LITHIUM ISOTOPE CONSTRAINTS ON QUANTITATIVE LITHIUM UPTAKE BY REVERSE WEATHERING: A NEW GENESIS MODEL FOR THE LARGEST KNOWN LITHIUM RESOURCE IN THE WORLD

MICHAEL JOHN REPETA

Thesis submitted to the University of Ottawa
in partial fulfillment of the requirements for the degree of
Master of Science, Earth Sciences

Department of Earth and Environmental Sciences
Faculty of Science
University of Ottawa

Abstract

This study presents a new reverse weathering model for lithium ore genesis at the Thacker Pass Project, the largest known lithium resource in the world. The formation of Li-rich claystones in the closed McDermitt Caldera paleolake system required hydrogeochemical conditions (a_{Mg2+}, $a_{SiO2(aq)}$, and pH) that drove the nucleation of reactive, Li-trapping Mg-silicates during brine evapoconcentration. Early-stage mineralization was marked by highly saline, alkaline brines that enabled the crystallization of extremely Li-rich illite (~1% Li) during diagenesis, while transitions to mixed-layer illite-smectite and hectorite reflect progressive freshening as solute inputs to the paleolake waned. The model integrates Li brine ore-genesis with analogs from modern East African Rift Valley alkaline lakes and ancient carbonate-rich basins associated with Mg-silicates, supported by low δ^7Li values ranging from -1.5 to 7.1‰ that lack vertical trends—indicating bulk-scale, quantitative Li uptake during mineralization. Episodic hydrothermal pulses are recorded in isotopic shifts, with depleted δ^7Li linked to more active hydrothermal inputs. These findings support a genesis model where Li enrichment was primarily governed by lacustrine salinity and alkalinity driven by evapoconcentration, coupled with the neoformation of Li-bearing clays. The maintenance of alkaline conditions during diagenesis has also been found to be essential in preserving the resource by limiting dissolution, silicification, or dolomitization of the Mg-silicates.

Résumé

Cette étude présente un nouveau modèle d'altération inverse pour la genèse du minerai de lithium du projet Thacker Pass, la plus grande ressource de lithium connue au monde. La formation d'argiles riches en lithium dans le système paléolac fermé de la caldera McDermitt a nécessité des conditions hydrogéochimiques (a_{Mg2+}, $a_{SiO2(aq)}$, et pH) qui ont favorisé la nucléation de silicates de Mg réactifs piégeant le lithium lors de l'évapoconcentration de la saumure. La minéralisation initiale a été marquée par des saumures fortement salines et alcalines qui ont permis la cristallisation d'illite extrêmement riche en lithium (~1 % Li) pendant la diagenèse, tandis que les transitions vers des couches mixtes d'illite-smectite et d'hectorite reflètent un rafraîchissement progressif à mesure que les apports de solutés au paléolac diminuaient. Le modèle intègre la genèse du minerai de saumure de Li avec des analogues provenant des lacs alcalins modernes de la vallée du Rift Est-Africain et d'anciens bassins riches en carbonates associés à des silicates de Mg, soutenu par de faibles valeurs de δ^7Li allant de -1,5 à 7,1 ‰ sans tendances verticales—indiquant une absorption quantitative et massive de Li pendant la minéralisation. Des impulsions hydrothermales épisodiques sont enregistrées dans les décalages isotopiques, avec un δ^7Li appauvri lié à des apports hydrothermaux plus actifs. Ces résultats soutiennent un modèle de genèse où l'enrichissement en Li était principalement régi par la salinité et l'alcalinité lacustres induites par l'évapoconcentration, couplé à la néoformation d'argiles contenant du lithium. Le maintien des conditions alcalines pendant la diagenèse s'est également avéré essentiel à la préservation de la ressource en limitant la dissolution, la silicification, ou la dolomitisation des silicates de Mg.

Acknowledgements

I would first like to express my sincere gratitude to Professor Ian Clark for introducing me to the field of aqueous isotope geochemistry during my undergraduate studies. Beginning as a laboratory technician working on helium and tritium and later delving into lithium isotopes through his research on nuclear waste repositories, he has played a pivotal role in shaping my research trajectory. His guidance, encouragement, and openness to exploring new directions in lithium isotope research led directly to the development and completion of this thesis. I am also grateful for his support in securing funding through the Natural Sciences and Engineering Research Council of Canada (NSERC), without which this work would not have been possible.

I thank Lithium Americas Corporation for their field support and samples. Dr. David Deak was instrumental in beginning this project. Special thank you to James Ingraffia for welcoming me to Nevada, providing a tour of UNR, and assisting with core sampling at Thacker Pass. Rick Zehner is also thanked for field guidance, thoughtful advice, and memorable hospitality. I also thank Dr. Tom Benson for helpful comments and discussions.

In the lab, I benefitted greatly from the support of Dr. Nimal De Silva, whose strong expertise with ICP-MS and ICP-OES was invaluable, and from Smita Mohanty, who provided essential training in sample preparation and instrumentation during my research assistantship under her supervision. I thank Sarina Cotroneo for her mentorship on column chromatography and clean lab protocols from my honours project and onward to this thesis, as well as Alain Mauviel for the thin section preparation. I also thank my supportive office friend, Julian (Myunghak) Kang, and everyone else I had the pleasure working alongside with in the 4th floor labs. Importantly, the challenging lithium isotope analysis performed by Dr. Shuangquan Zhang from Carleton University was critical in generating the final data, and he is thanked for the resulting high quality isotope data.

From the Geological Survey of Canada, I am particularly grateful to Dr. Jeanne Percival and her oriented powder XRD measurements. Her expertise in clay mineralogy and her kind willingness to teach me about the fascinating world of mixed-layer clays were very constructive. I also thank Dr. Lilianne Pagé for her clay separates digestion work, and Dr. Zhaoping Yang for her generous provision of the JR-2 lithium isotope reference material.

I would also like to thank my friends for their kind encouragements. Finally, most of all, I would like to thank my loving family for their unwavering support throughout my academic journey.

Table of Contents

List of Figures

List of Tables

1. Introduction

Demand for lithium-ion batteries used in portable electronics and a global effort to reduce carbon dioxide (CO_2) emissions in response to climate change requires a dramatic growth of the lithium-ion battery supply chain in the coming decade (Berry, 2020). Lithium (Li) is both the lightest and the most electropositive metal on the periodic table. These properties make this metal a central component of energy-dense, high-voltage rechargeable batteries essential for electric vehicles and renewable energy storage (Julien et al., 2016). With current Li production coming mainly from Australian pegmatite deposits (e.g. spodumene) and Chilean brine deposits (Benson, Coble, et al., 2017), developing new Li resources is a growing priority for countries and manufacturers (Natural Resources Canada, 2020; Sanderson, 2020). The Lithium Americas Corporation owned Thacker Pass Project is the largest known Li resource in the world (Lithium Americas, 2025) and is positioned to alleviate some of this increasing demand as the first mined sedimentary Li resource (Ehsani et al., 2018). The deposit rests within ash-rich sediments in the remnants of an ancient caldera lake bed that formed following the Middle-Miocene supereruption of the McDermitt Caldera (Benson, Coble, et al., 2017; Castor & Henry, 2020; Ehsani et al., 2018; Glanzman et al., 1978; Glanzman & Rytuba, 1979; Rytuba & Glanzman, 1979). Li is held in claystones of a mix of smectite clay known as hectorite, with whole-rock concentrations up to 4,000 ppm that gradually transitions with depth to an illite clay with whole-rock concentrations up to 9,000 ppm (Ehsani et al., 2018). How these clays became highly enriched in lithium is poorly understood and is the focus of recent research efforts (Benson, Coble, et al., 2017; Castor & Henry, 2020; Ingraffia et al., 2020). This thesis is an attempt to further the understanding of the geological processes responsible for lithium enrichment in caldera systems to add new lithium resources to the supply chains of the next generation of Li-ion batteries.

Lithium enrichment in caldera systems involves complex volcanic processes below the surface of the Earth and surficial processes that are largely controlled by climate (Benson, Coble, et al., 2017; Chen et al., 2020; Godfrey et al., 2013; Hofstra et al., 2013). Like for all types of Li deposits, Li enrichment begins in magmas that are generated by the melting of thick continental or transitional crust with a significant proportion of felsic material (Benson, Coble, et al., 2017; Chen et al., 2020; Hofstra et al., 2013). Because Li is incompatible in most minerals that crystalize from melts, it becomes progressively enriched in the residual melt during melt fractionation (Bartels et al., 2015;

Benson, Coble, et al., 2017; Ellis et al., 2018; Neukampf et al., 2019), and will often produce Li-rich minerals like spodumene ($LiAlSi_2O_6$), typically during magmatic orogens (Chen et al., 2020; Magna et al., 2010). Eruption of these types of granitic magmas can produce closed basins like the McDermitt Caldera, where Li and other mobile solutes are leached by meteoric and hydrothermal fluids, or degassed into the system (Ellis et al., 2018; Ingraffia et al., 2020), and are then concentrated through time by evaporation (Figure 1) (Benson, Coble, et al., 2017; Chen et al., 2020; Godfrey et al., 2013; Hofstra et al., 2013). High Li concentrations can then be obtained in large volumes of brine that accumulate over time in closed basins, like is commonly observed today in the salt-crusted prolific salars of the Atacama desert in Chile (Munk et al., 2016). The additional steps required for lithium clays to form following evaporative concentration in closed basins have received very little attention and are undefined. Constraining the surficial conditions and chemical reactions that lead to Li-clay mineralization could provide much needed insights for exploration within individual basins, or at the global scale in locating new sedimentary Li deposits. Furthermore, unravelling the processes that lead to Li incorporation in these clays could help develop the necessary tools that can effectively liberate Li from their structure.

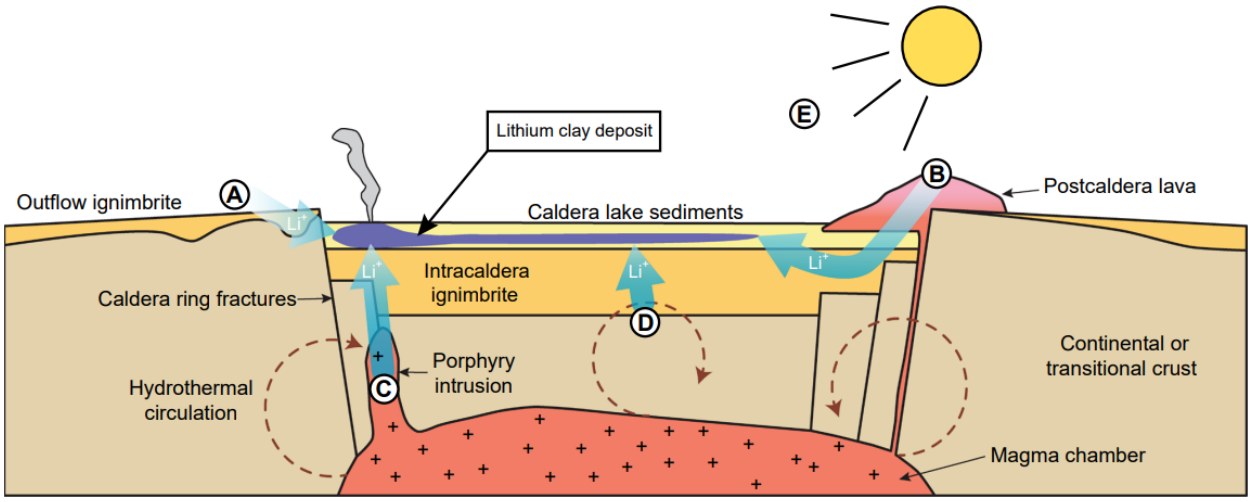

Figure 1. Schematic model for the genesis of sedimentary lithium deposits (modified from Benson et al. (2017)) . Lithium is supplied by the weathering of caldera-forming ignimbrites (A) and younger postcaldera lavas by meteoric waters (B), by hydrothermal fluids (C), and by the outgassing of intrusions and degassing of the intracaldera ignimbrite (D). Arid climatic periods concentrate the lithium accumulated in the basin as water evaporates (E).

This study is focused on the lithium isotopes of the Li-clays of the caldera-hosted Thacker Pass sedimentary lithium deposit. Lithium isotopes have primarily been used to trace chemical silicate weathering in Earth's more typical Li-poor environments, as it relates to natural drawdown

processes of atmospheric CO_2 and climate (e.g. Pogge von Strandmann et al., 2020). This is possible because clays are common silicate weathering products, and they all have a higher affinity to uptake the lighter ^6Li isotope during their formation, leaving the residual fluid enriched in the heavier ^7Li isotope (Huh et al., 1998). The Li isotope ratio composition of weathering environments is largely controlled by the ratio between the flux of Li from dissolution of the source rock and the flux of Li incorporation in clays, and the fractionation factor (Bouchez et al., 2013).

Lithium isotope ratios are most-commonly reported as δ^7Li, relative to the L-SVEC Li isotope standard (e.g. Misra & Froelich, 2009), derived from the spodumene-rich ores of Kings Mountain, North Carolina, USA, which represents the Li isotopic composition of the global magmatic continental crust, where $\delta^7Li = 0$ ‰ (Flesch et al., 1973; Tomascak et al., 2016):

$$\delta^7Li\ (‰) = \frac{{}^7Li/{}^6Li_{\ sample} - {}^7Li/{}^6Li_{\ L-SVEC}}{{}^7Li/{}^6Li_{\ L-SVEC}} \text{ X } 1000 \qquad \text{[Equation 1.]}$$

The isotopic composition of thermal fluids actively sourcing Li to the largest producing Li brine deposit in the world, known as the Salar de Atacama (Cabello, 2021), is characterised by the volcanic rock-like δ^7Li values of 0‰ (Godfrey & Álvarez-amado, 2020). As these Li-charged waters flow along topography and accumulate in the fault-bounded salar, δ^7Li gradually evolves to values up to 12.6‰ and Li becomes increasingly more concentrated to a remarkable 5000 ppm (Munk et al., 2018). Most fractionation occurs along the flow path by formation of secondary mineral phases in the transition zones that reach the halite nucleus during evapoconcentration (Munk et al., 2018). Li-claystones have not been reported be actively forming in the Salar de Atacama, even if the volcanic setting is very similar to the McDermitt Caldera. The main difference is that Thacker Pass is hosted in a caldera basin, and the Salar de Atacama is within a fault-bounded basin (e.g. Munk et al., 2016).

The objective of this thesis is to ascertain whether lithium isotopes, together with an understanding of the mineralogy and geological setting of the Thacker Pass deposit, can advance our understanding of the mechanism for Li mineralization.

2. Literature Review

2.1 Geologic Setting

The Thacker Pass lithium deposit is located within the McDermitt Volcanic Field in north-central Nevada, USA, in the southern portion of the McDermitt caldera (Figure 2) (Ehsani et al., 2018). Hotspot silicic volcanism began in the region about 16.5 Ma, following intrusion of basaltic magma (Steens Basalt) into the upper crust, during the initial impingement of the Yellowstone plume, that has since migrated along the Snake River Plain-Yellowstone trend to present-day Wyoming and Montana (Coble & Mahood, 2012). The upper crust here in the Middle-Miocene was composed of an accreted island arc or transitional terranes (Henry et al., 2017). Partial melting or assimilation of large amounts of transitional crust of felsic composition in this tectonic setting generated voluminous rhyolitic magmas enriched in Li (Benson, Coble, et al., 2017; Castor & Henry, 2020). Eruption of the peralkaline rhyolite to metaluminous trachyte ~1000 km^3 McDermitt Tuff, ~16 Ma, led to the collapse of the McDermitt Caldera (Castor & Henry, 2020). Smaller postcaldera eruptions of more rhyolitic lavas until about 16.3 Ma generated associated hydrothermal U, Au, Hg, and Ga deposits along the caldera ring fractures (Benson, Mahood, et al., 2017; Castor & Henry, 2000; Rytuba & Glanzman, 1979). Most magmatism ceased soon after post-collapse resurgence, driven by intrusion of icelandite basalts at about 16.1 Ma (Castor & Henry, 2020). Lacustrine sedimentation in the caldera started immediately after collapse, continued during and after resurgence, until eventual drainage of the lake (Castor & Henry, 2020; Ingraffia et al., 2020).

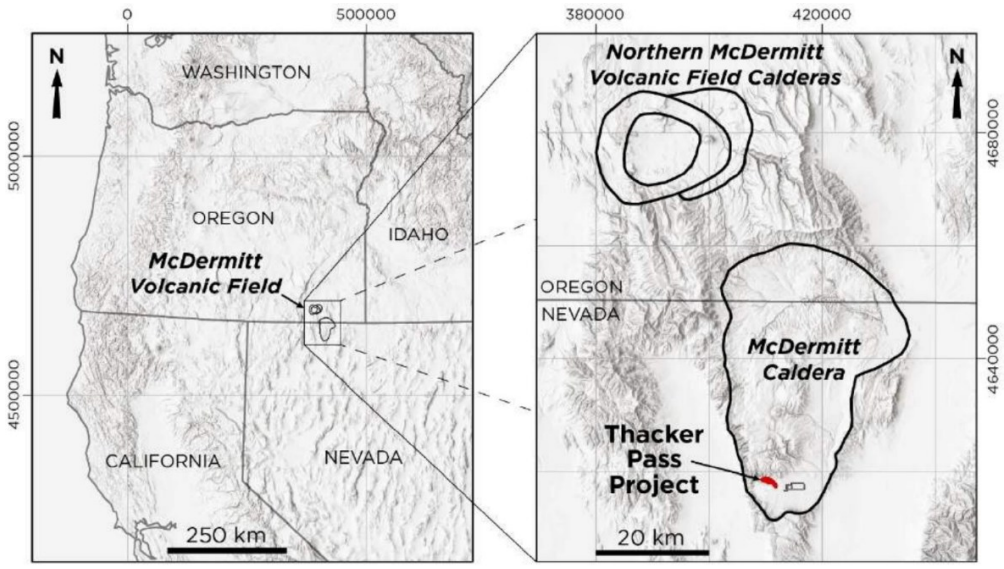

Figure 2. Location of the Thacker Pass Li deposit (from Ehsani et al. (2018)).

2.2 Formation of the McDermitt Caldera Lithium Clay Deposit

Many studies were conducted to better understand the mineralogy, distribution, and origin of the sedimentary lithium deposit, which was accidently discovered by Chevron in the late 1970s while exploring for uranium in the tuffaceous caldera lake sediments (Ehsani et al., 2018). The Li resource is laterally extensive and widespread throughout the McDermitt Caldera and is not focused along the caldera rim like the historically mined hydrothermal U, Hg, and Ga resources (Figure 3) (Benson, Coble, et al., 2017). The sediment packages that host the Li-clays can be as much as 200 m thick and thin toward the central resurgent domes, where they were eroded (Glanzman & Rytuba, 1979). They have little exposure and can only be fully observed from drill core.

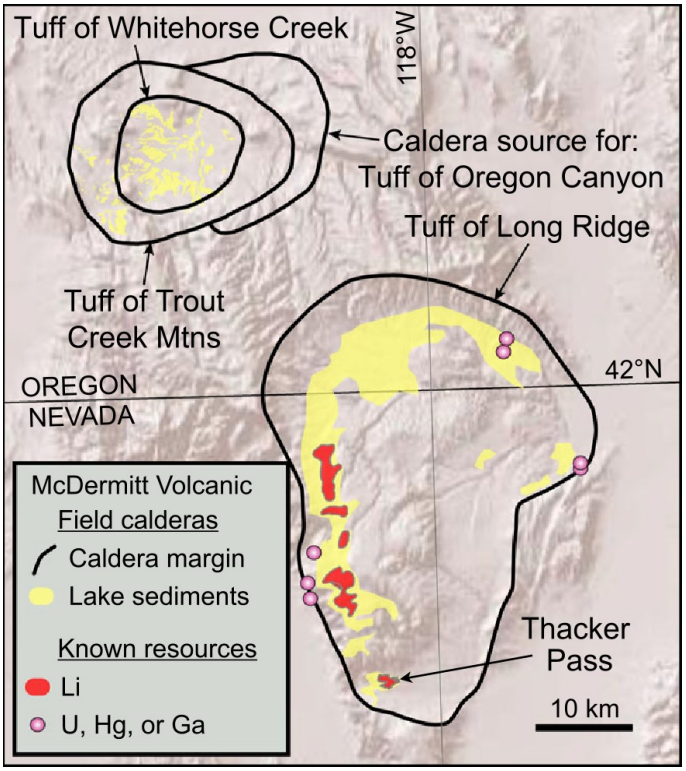

Figure 3. McDermitt Volcanic Field caldera-forming rhyolitic ignimbrites, Thacker Pass, and location of known resources (modified from Benson et al. (2017)).

The sediments of the McDermitt Caldera and their distribution were first described by Glanzman et al. (1978). They proposed that the sediments reveal a lacustrine environment because of an abundance of fossils such as fish, gastropods, mollusks, leaves and bits of wood was observed in the northern and western sides of the caldera. The trioctahedral Li-rich smectite known as hectorite was found to be associated with calcite ($CaCO_3$), and high Li concentrations were positively

correlated with magnesium (Mg) and fluorine (F) concentrations in whole-rock samples. They suggested that the Li was likely leached from volcanic material and incorporated into clay beds of altered peralkaline ash-flow tuffs. High Li concentrations were proposed to be a result of increasing salinity and possibly alkalinity of interstitial fluids during zeolitization of volcanic glass. Lithium enrichment in the hectorite clay was found to roughly correlate with the progressive alteration of the volcanic glass. From the least amount of Li in zones of unaltered glass, to intermediate amounts in zones of clinoptilolite-feldspar, to the highest with those reaching analcime-K-feldspar alteration. They mapped the lateral variation of the alteration zones in the surficial tuffaceous sediments throughout the caldera (Figure 4):

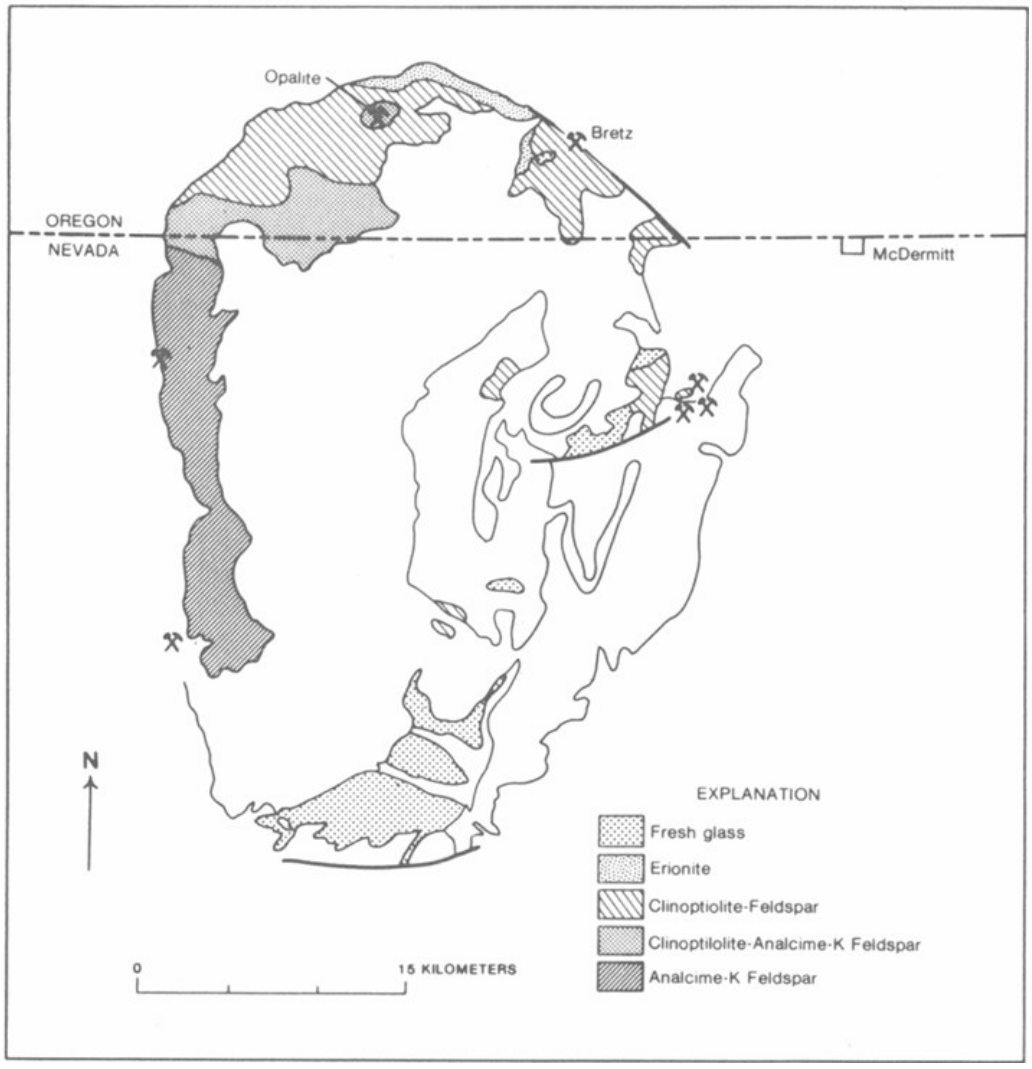

Figure 4. Lateral extent of surficial tuffaceous sediment alteration zones in the McDermitt Caldera (from Glanzman et al. (1978)).

Glanzman & Rytuba (1979) found additional carbonates associated with the hectorite, such as interbedded primary oolites on the western side of the caldera and dolomite. Pyrite was also found with hectorite containing Li concentrations up to 6,800 ppm. Quartz and feldspars were found to have an inverse relationship to the hectorite and carbonates. Dioctahedral Al-smectites with low lithium contents were also found at the base and top of the hectorite deposit near the resurgent domes (Montana Mountains). The hectorite was suggested to be of diagenetic origin.

Glanzman & Winsor (1982) hypothesized that the deposit could have formed from the accumulation of a Li-rich gel at the bottom of the caldera lake, which ultimately precipitated a massive Li-rich clay layer, with thin intervals of tuffaceous sediments that would have been deposited intermittently during the precipitation of the clay. This study was a brief internal report, without details of what led to the gel hypothesis.

Morissette (2012) paired X-ray diffraction (XRD) analysis with structural formula calculations from the chemical analysis of the clay-size fractions to identify that the hectorite has some aluminum (Al^{3+}) substituting for silicon (Si^{4+}) in the tetrahedral layer of the clay, giving it an intermediate tetrahedral sheet composition between hectorite and the more Al-rich saponite. Morissette (2012) discovered that the highest Li concentrations (~ 1% Li) are found with albite near the base of the deposit in an illite clay, like tainiolite in composition; $KLiMg_2Si_4O_{10}F_2$. This phase was suggested to have potentially formed by a diagenetic smectite-illite conversion in a hydrothermal environment that left an observable gradual smectite-illite transition with depth. Sedimentary tainiolite has not been reported elsewhere. This rock-forming mica usually forms by hydrothermal alteration via high temperature Li-rich fluids (Tischendorf, Rieder, Förster, Gottesmann, & Guidotti, 2004), and is typically found in carbonatite complexes (Al-ani & Sarapää, 2016; Cooper, Paterson, & Reid, 1995; Le Bas et al., 1992; Sharygin, 2017; Traversa et al., 2001). Morissette (2012) interpreted that the bedding and apparent alignment of the clay minerals to bedding could suggest that the clays formed as an alteration of the tuffaceous sediments.

Detailed work by Castor & Henry (2020) observed that the highest Li concentrations are most commonly found in the deeper illitic parts of the deposit, and are lower in sections with large amounts of ash. They identified fluorite in the claystones of many drill cores of the deposit, among the pyrite, zeolites, feldspars, and carbonates described in previous studies. The smectite to illite transition in the deposit described by Morissette (2012) was also observed by XRD and

geochemically (Figure 5). An authigenic K-feldspar in the illite zone was measured to have an $^{40}Ar/^{39}Ar$ age of 14.9 Ma. The age of this authigenic K-feldspar is ~1.2 Ma younger than what is thought to be the end of magmatism in the caldera, which they suggest mitigates against a simple hydrothermal origin to the Li-clay deposit. Their suggested clay formation mechanism generally follows Morissette (2012), where they propose about 200 m of tuffaceous sediments from regional pyroclastic eruptions accumulated in the caldera and were altered by "closed hydrologic system diagenesis" to the currently found zonation of clays and alteration minerals that follow a vertical zonation of analcime, K-feldspar, and albite.

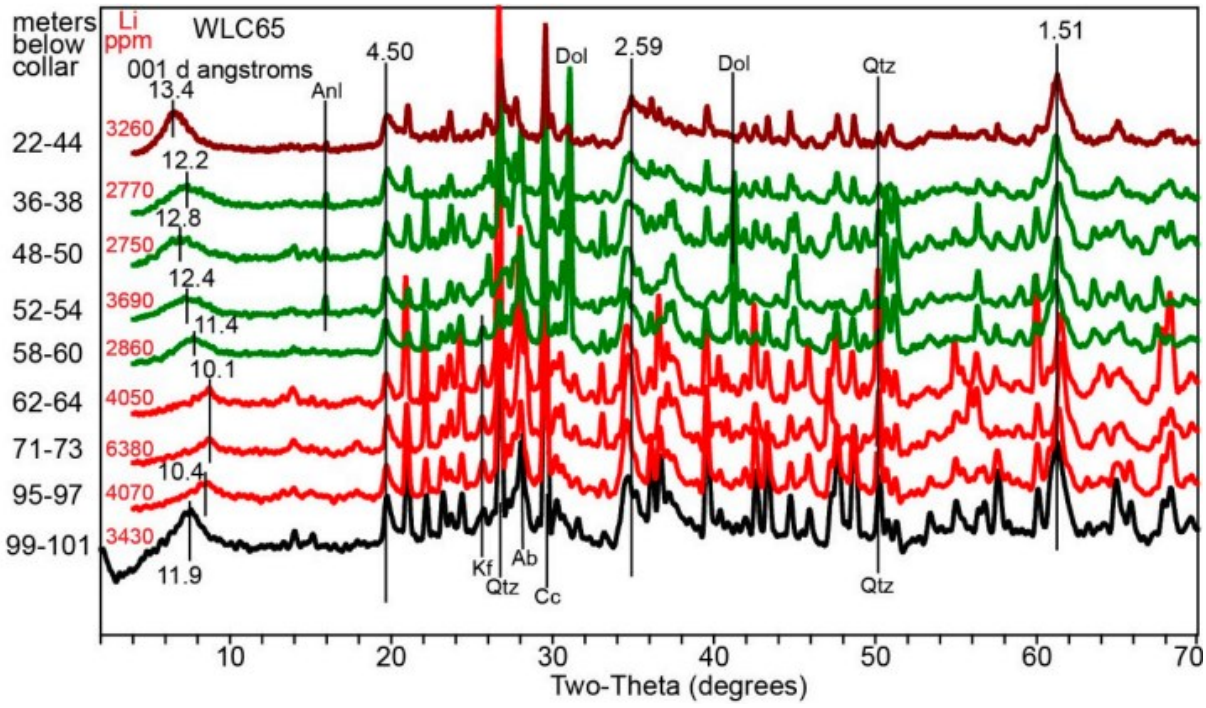

Figure 5. Whole-rock XRD scans and mineralogy of depth intervals sampled from Thacker Pass drill core (from Castor & Henry (2020)). Lithium concentrations and basal spacing (d(001)) of clays, along with other clay peaks (4.50, 2.59, and 1.51 Å). The upper burgundy line is the upper smectite zone, green is the upper transitional clay zone, red is the illite zone, and black is the lower transitional clay zone. Other identified minerals include analcime (Anl), albite (Ab), quartz (Qtz), calcite (Cc), K-feldspar (Kf), and dolomite (Dol).

The thinking of Castor & Henry (2020) largely builds on the original genesis model of Glanzman et al. (1978) by adding a new albite alteration zone where the highest Li concentrations are found in the illite. A deeper albite alteration zone with Li-bearing illite could not be previously observed without drill core from Thacker Pass. This new zone at depth now represents maximum alteration of the tuffaceous sediments throughout the McDermitt Caldera. They propose that the occurrence of both analcime and albite zones at Thacker Pass is similar to what has been observed in the

lacustrine Jurassic Morrison Formation of diagenetic origin (e.g. Fishman et al., 1995). They emphasized that the McDermitt Caldera is an example of a closed hydrologic system diagenesis, reflecting evolving water alkalinity and salinity with temperatures estimated to range from 25 °C to 70 °C, but it is unique because other studied diagenetic systems do not have lithium-rich smectite and illite.

To evaluate the total amount of Li in the entire 700 km^2 McDermitt Caldera, Castor & Henry (2020) extrapolated that a total of approximately 120 million tons of Li is currently found in the clays. This is a massive amount of Li, compared to the officially reported 86 million tons of Li found in resources worldwide (USGS, 2021). For more context, there are resources of 9.6 million tons of Li found in the currently exploited Li brines of Chile (USGS, 2021), which is more than an order of magnitude less Li than what could be found in the McDermitt Caldera. This highlights that the clays are in the McDermitt Caldera are highly unusual and special.

Castor & Henry (2020) also fixated on the tuffaceous sediments as the sole Li source for the clays, and showed through Li mass balance calculations that they, alone, might not have contained enough Li to provide all the Li currently found in the deposit. They then leaved open the possibility that Li could be introduced by hydrothermal fluids, like proposed by Benson, Coble, et al. (2017).

Ingraffia et al. (2020) characterized the stratigraphic mineralogy and geochemistry of drill core from Thacker Pass (Figure 6). They observed that the Li-clays are associated with an abundance of calcite (nodules and radiating lenses) and pyrite. High Li concentrations (>7000 ppm) were found in the illite associated with fluorite, interpreted to replace some of the calcite nodules. High Li concentrations were found to correlate with elevated concentrations of Cs, Rb, As, Mo, Sb, Hg, F, and S. They suggest most of these elements, along with Li, were degassed to the caldera floor by high-temperature fumarolic activity generated by the cooling, compaction and devitrification of the underlying ~1 km thick rheomorphosed and densely welded intra-caldera tuff. Li was then incorporated in clays that are interpreted to be an alteration of the tuffaceous sediments, like Morissette (2012) and Castor & Henry (2020). They however introduced a secondary hydrothermal alteration component on top of the diagenetic alteration model because of newly observed illite, pyrite and quartz veinlets, breccia textures, and high concentrations of elements associated with hydrothermal activity. The Li-clay is now seen more as a hydrothermal alteration.

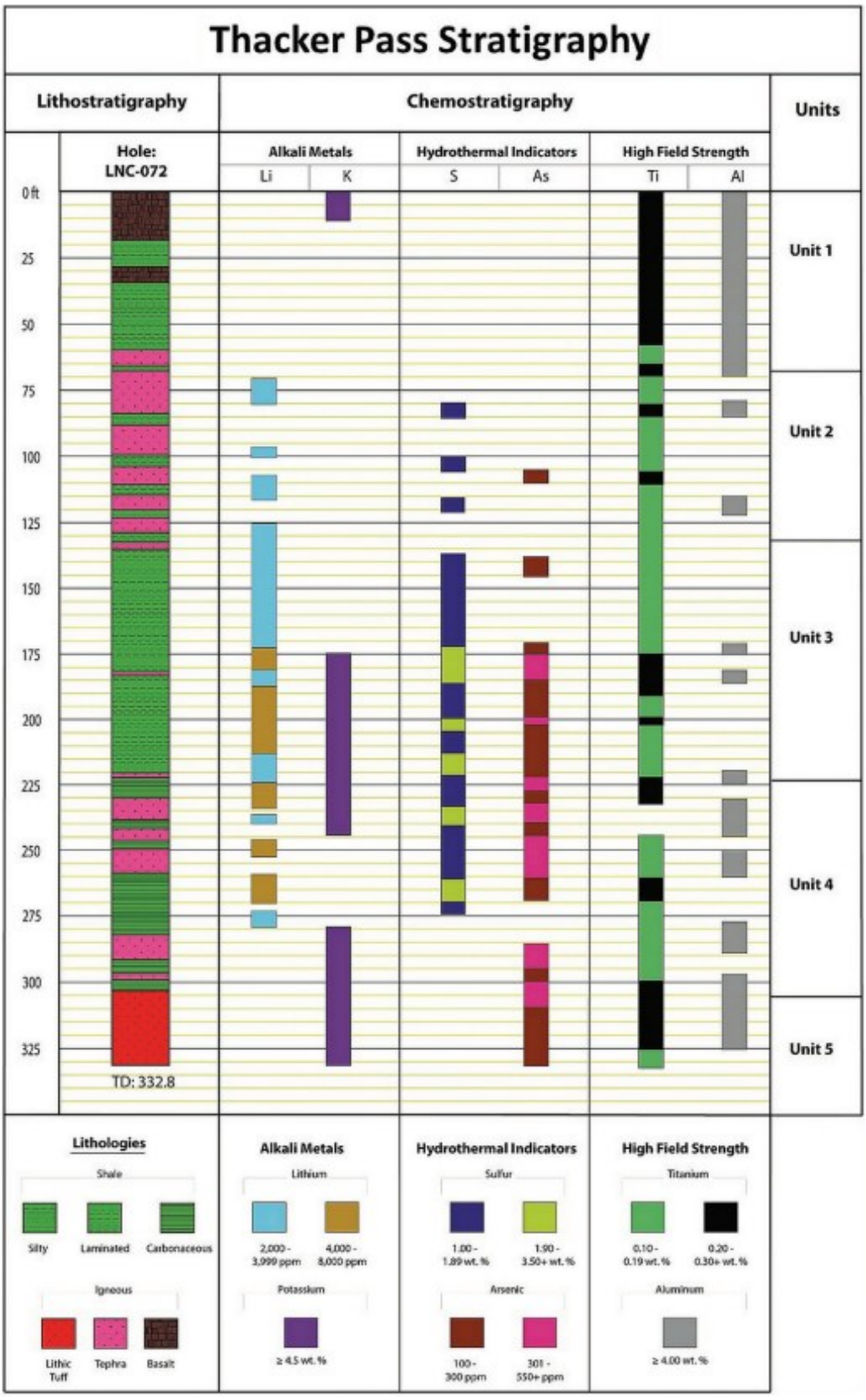

Figure 6. Stratigraphy of the Thacker Pass sedimentary lithium deposit (from Ingraffia et al. (2020)).

2.3 Hectorite as a Magnesian Clay Mineral

Hectorite was originally reported by Foshag & Woodford (1936) as the "Bentonitic Magnesian Clay-Mineral From California" in the *American Mineralogist*. The clay was sampled from a Tertiary volcanic series, three miles south of Hector, in San Bernardino County, California. XRD spectra revealed that the mineral is closely related to the magnesian clay known as saponite. The Hector magnesian clay was found with calcite nodules and had a chemical composition notably high in lithium and sodium, and poor in aluminum. They suggested it was probable that the clay is a heavily altered dacite tuff. Strese & Hofmann (1941) later proposed the name "hectorite" for this Li-rich magnesian clay mineral. Ross & Hendricks (1943) suggested the hectorite likely formed under alkaline or neutral conditions because of its association with calcite. Ames et al. (1958) proposed it formed by hydrothermal alteration of ash-rich sediments in an ancient lake. More recent thinking proposes that hectorite can precipitate directly from saline lake water (Calvo et al., 1999; Starkey, 1982; Tardy et al., 1972). Tardy et al. (1972) recognized that most clay minerals can contain some Li, including the more commonly found Al-dioctahedral clays that form by alteration during silicate weathering, and that much higher Li concentrations are found in authigenic phases that precipitate from solution (neoformation) in arid environments, where carbonates and sulfates also precipitate. Most of the clay phases that form in these environments are not only hectorite, but other magnesian clays (Table 1.) that are all closely related (Tardy et al., 1972). Li can substitute for Mg in minerals because of their similar ionic radii (Goldschmidt, 1937). All Mg-clays can hold Li in their octahedral sites and there is no official Li concentration threshold that distinguishes hectorite from the rest of the magnesian clays (Hindshaw et al., 2019).

Magnesian Clay Minerals	*Ideal Composition*
Trioctahedral Smectites	Saponite: $Mg_3(Si_{3.67}Al_{0.33})O_{10}(OH)_2M^+_{0.33}$ Hectorite: $(Mg_{2.67}Li_{0.33})Si_4O_{10}(OH)_2M^+_{0.33}$ Stevensite: $(Mg_{2.67}\,\square_{0.33})Si_4O_{10}(OH)_2M^+_{0.33}$
Palygorskite	$(Mg, Al, Fe^{3+})_5(Si, Al)_8O_{20}(OH)_2(OH_2)_4 \bullet 4H_2O$
Sepiolite	$Mg_8Si_{12}O_{30}(OH)_4(OH_2)_4 \bullet 8H_2O$
Kerolite (hydrated variety of talc)	$Mg_3Si_4O_{10}(OH)_2$

Table 1. The main magnesian clay minerals (modified from Pozo & Calvo (2018)).

Laboratory synthesis experiments reveal that the rapid crystallogenesis of hectorite and crystallographic structure is identical to stevensite (Figure 7) (Decarreau, 1980). The negative layer charge of hectorite is derived from Li^{+} substituting for Mg^{2+} in the octahedral sites, a process that can be aided by fluoride (F^{-}) substituting for hydroxide (OH^{-}) (Decarreau, 1980). This substitution may be thermally activated, and the rate of this substitution and amount of Li incorporated in the clay structure increases with Li concentration in solution (Decarreau et al., 2012). Without F^{-}, regardless of how high the Li concentration in solution, a maximum Li content of 3400 ppm is possible in the Mg-silicate structure (Vigier et al., 2008). Fluoride substitution for hydroxide is common in natural hectorite, and also favors crystallogenesis rather than nucleation of new hectorite nuclei (Decarreau, 1980; Granquist & Pollack, 1959). The key difference between hectorite and stevensite is the lack of isomorphous substitutions in stevensite; the negative layer charge comes entirely from the octahedral vacancies, which are illustrated in Table 1. as a box symbol in its typical chemical formula and as transparent octahedra in the crystallographic model of Figure 7. The negative layer charge can be compensated electrostatically in the interlayer space of the smectites (M^{+}) by readily exchangeable hydrated monovalent or divalent cations (e.g. Li^{+}, Mg^{2+}, K^{+}, Na^{+}), giving the clays swelling properties because of the water molecules (Velde, 1995). Addition of potassium (K^{+}) to synthetic Na-saturated fluorinated hectorite in solution by Möller et al. (2010) has been found to rapidly and non-reversibly fixate every second interlayer, resulting in a regular sequence of hydrated (d(001) = 12.3 Å) and dehydrated (d(001) = 10.0 Å) layers.

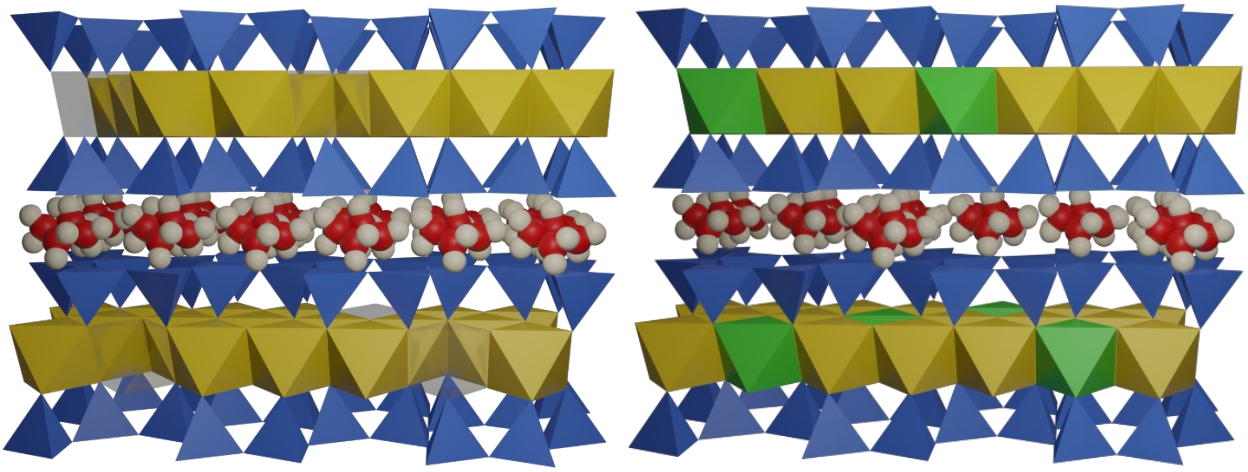

Figure 7. 3D clay structure of stevensite (left) and hectorite (right) (adapted from Tosca & Wright (2014) and Vigier et al. (2008)). Two tetrahedral-octahedral-tetrahedral (TOT) layers separated by exchangeable charge-balancing hydrated monovalent cations in the clay interlayer. Magnesium octahedra in yellow, silicon tetrahedra in blue, octahedral vacancies as transparent, and lithium octahedra in green. The TOT units usually form repeating stacks along the C-axis, and can include interstratifications, like is the case for illite-smectite mixed-layer clays.

2.4 Lithium Isotopes and Clay Mineral Interactions

Li has two stable isotopes; ^{6}Li and ^{7}Li, with abundances of 7.59% and 92.41% respectively (Coplen et al., 2002). The large relative mass difference between the two isotopes of about 16.7% allows for measurable fractionation during geological processes (e.g. Hoefs & Sywall, 1997). While the Li isotopes of natural trioctahedral Mg-clays like hectorite, saponite, and stevensite have received little attention, their high solubilities and thus ease of laboratory synthesis (Carrado et al., 2006) have made them ideal candidates to experimentally determine the fractionation factor between clay and water at temperatures relevant for Earth surface processes (Hindshaw et al., 2019; Vigier et al., 2008). Hydrated Li is coordinated with 4 oxygen atoms mainly as $[Li(H_2O)_4]^+$ (Hindshaw et al., 2019), with bond lengths of around 1.9 Å (Rudolph et al., 1995), and octahedral Li is coordinated with 6 oxygen atoms with bond lengths of around 2.08 Å (Kalo et al., 2012). Isotopic fractionation occurs as Li migrates from each bonding environment because shorter bonds are stronger than longer bonds, therefore the heavier ^{7}Li is preferably retained in the aquo-complex, and the lighter ^{6}Li is more readily incorporated in the octahedral sites of clays (Hindshaw et al., 2019).

Hindshaw et al. (2019) obtained a fractionation factor ($\alpha = \Delta^{7}Li_{solid\text{-}solution}$) of 0.9790 ± 0.0011 for the octahedral sites from the clay synthesis experiments (at 20 °C), by using a combination of isotopic analysis of bulk, residual, and exchangeable solutions, coupled with ^{7}Li-NMR measurements. Their study provided fractionation factors for each clay site (interlayer, octahedral, and pseudo-hexagonal sites). Fortunately, the vast majority of Li in hectorite and Li-illite is primarily held in the trioctahedral sites (Morissette, 2012), suggesting that the octahedral site fractionation factor could be applied to the claystone ores of Thacker Pass.

Not all clays have the same number of available octahedral sites in their structures that can remove and thus isotopically fractionate Li. Dioctahedral aluminum-smectites that typically form during weathering (e.g. montmorillonite) can usually hold much less Li than trioctahedral smectites like Li-rich hectorite and other Mg-clays (Tardy et al., 1972). Mg-clays have not been found in the Salar de Atacama, even if the water inflows become supersaturated relative to them along their evaporation paths (Boschetti et al., 2007). $\delta^{7}Li$ enrichment during flow along their evaporation paths has been suggested to stem from weathering reactions that form clay phases with low Li concentrations of 1-20 ppm (Munk et al., 2018). Further $\delta^{7}Li$ enrichment has been suggested to occur during secondary salt formation (Godfrey et al., 2013; Munk et al., 2018).

3. Hypothesis

The paleofluid Li isotope signatures preserved in the Li-claystones of the Thacker Pass Li deposit should have more enriched δ^7Li than what has been measured in the Li brine resource of the Salar de Atacama (12.6‰ (Munk et al., 2018)) because of extensive fractionation associated with the formation of voluminous accumulations of Li-rich trioctahedral Mg-clays. Periods reflecting high volcanic Li inputs to the caldera system should have more depleted δ^7Li, while more quiescent periods in the caldera lake should have more enriched δ^7Li from the Li-clay mineralizing trend (Godfrey & Álvarez-amado, 2020). If enrichment occurred through fluid migration during diagenesis, or by later hydrothermal alteration as proposed by Ingraffia et al. (2020), downcore δ^7Li variations should correlate with the smooth increases in Li enrichment and the diagenetically altered mineralogical zones of the aluminous tuffaceous sediments reported by Castor & Henry (2020). The first scenario would suggest that most enrichment occurred during evaporation and that the paleolake water composition had the principal role in ore mineralization. The implications of this scenario would require further investigation into the chemical controls inhibiting this type of mineralization during evaporative brine evolution in the Salar de Atacama system, despite their supersaturation (Boschetti et al., 2007).

4. Methodology

4.1 Sample Collection

Claystone samples from Thacker Pass were collected at measured depth intervals from drill core and stored in sample bags. Care was taken to collect samples representative of the different lithologies reported by Morissette (2012) and complimentary to the ongoing research activities of Ingraffia (2020), Ingraffia et al. (2020), and Castor & Henry (2020). Claystone samples were collected from the upper smectite zone, the transitional zone, and the deeper illite zone. A fresh volcanic glass sample from the McDermitt Tuff was also mailed to the University of Ottawa.

4.2 Photomicrography

Photomicrography offers the opportunity to analyze the texture of the claystones and identify the larger mineral phases that are associated with the Li-bearing clay minerals. 10 claystone samples were submitted to the University of Ottawa Rock Preparation Laboratory to be epoxy-impregnated and cut into covered thin sections. Some of the submitted samples came directly from the remaining material that was left over from the geochemical sampling work described in the following section. Thin sections were scanned with and without polarizing sheets at a resolution of 4800 dpi and were examined with an Olympus BX41 binocular polarizing microscope under plain and polarizing light. Photomicrographs were taken using an Olympus SC180 camera.

4.3 Sample Preparation

Two different approaches to sample preparation were used. The first was a bulk approach, and the second involved clay-size (< 2 μm) separation. Separating the clay-sized fraction of the claystone samples offers the opportunity to have XRD and chemical data that is more focused on solely the Li-bearing clay minerals.

- 9 measured-out claystone samples were selected from the LNC-063 core for bulk geochemistry and XRD work.

- The volcanic glass sample was also selected for bulk geochemistry.

- The clay-size fraction of 14 claystone samples was separated from LNC-001.

4.3.1 Bulk Sample Preparation

About 40 g of each measured-out LNC-063 core sample was crushed to a medium gravel to silt size using a steel jaw crusher. ~10 g aliquots of each sample were crushed further with a mortar and pestle. ~4 g of each of these aliquots was milled in 10 mL of isopropanol using a micronizing McCrone Mill at the Geological Survey of Canada in Ottawa. The suspensions were then transferred to plastic weigh boats and dried in a drying oven set at 40 °C. The dried clay material was then transferred to 50 mL falcon tubes.

The volcanic glass sample was crushed using a jaw crusher. The glass shards were then collected and pulverized using a mortar and pestle. The powder was then stored in a 50 mL falcon tube.

4.3.2 Clay Separation Procedure

To separate the clay-size fraction, the ~40 g core samples were first lightly broken-up with a mortar and pestle, before being disaggregated by submerging in DI water-filled 500 mL HDPE bottles and shaking on an orbital shaker. The suspensions were then manually shaken vigorously and decanted into 1 L HDPE bottles. DI water was then added to fill the water level to the marked-out line on the bottle and left to stand to equilibrate the water temperature. The 1 L bottles were then shaken and inverted, prior to uncapping them and letting them stand. The clay-size fraction was separated with a syringe using Stokes' law:

$$V = \frac{d^2 g\,(\rho_s - \rho_f)}{18\eta} \qquad \text{[Equation 2.]}$$

Where:

- V is the velocity of the spherical particle.
- d is the diameter of the particle.
- g is the gravitational force.
- ρ_s is the density of the clay mineral.
- ρ_f is the density of water.
- η is viscosity of water.

By using the calculated velocity, the required time for clay-sized particles with a diameter of 2 μm to travel a settling distance (h) of 4 cm from the marked-out-line on the HDPE bottles can be calculated using:

$$t = \frac{h}{V}$$ [Equation 3.]

To not discriminate between smectite and the slightly denser illite clay phases, the mineral density of 2.9 g/cm^3 for illite was selected, yielding a settling time of 2 hours, 31 minutes, and 29 seconds. After the required time, the clay suspension was carefully extracted above the settling line. The suspensions were stored in 250 mL bottles before drying in plastic weigh boats in an oven set at 40 °C. Once dried, the material was transferred to 50 mL falcon tubes.

4.4 X-Ray Powder Diffraction

Two different powder XRD techniques were used for characterizing the bulk samples and the clay separates. The 9 bulk samples were characterized by randomly oriented powder XRD to get the bulk mineralogy of the samples, with particular attention in identifying the diagenetic alteration mineralogy of the aluminous tuffaceous sediments reported in previous studies. An aliquot of 5 clay separates from core LNC-001 were submitted to the Geological Survey of Canada for oriented powder XRD to more accurately measure the smectite and illite proportions in the mixed-layer phases.

4.4.1 Bulk Samples Randomly Oriented Powder Mounts XRD

Aliquots of the dried bulk samples were prepared by grinding using a mortar and pestle and pressing the powder in an aluminum sample holder. The randomly oriented powder mounts were analyzed by a Rigaku Ultima IV Diffractometer equipped with copper Kα X-rays, scanning from 2° to 65° at a rate of 1° per minute. Phase identification was achieved by referencing the measured peaks to the International Centre for Diffraction Data (ICDD) PDF-2 database.

4.4.2 Clay Separates Smear Slide Sample Mounts XRD

Oriented powder XRD measurements were taken by the Mineralogical Laboratory of the Geological Survey of Canada in Ottawa, Canada. To orient the platy clay minerals, aliquots of clay separates were suspended in distilled water and pipetted onto glass slides and subsequently air-dried. The dried smear mounts were analyzed by a Bruker D8 Advance Power Diffractometer equipped with a Lynx-Eye Detector and cobalt Kα X-rays. The smear mounts were then analyzed a second time following ethylene glycol solvation and a third time following heating to 550 °C in a muffle furnace.

4.5 Geochemical Characterization

Two different analytical methods were performed for the geochemical characterization of the bulk claystone samples, and both the clay separates and the powdered volcanic glass.

4.5.1 Bulk Claystone Sample Geochemical Characterization

50 mg aliquots of the dried bulk samples were weighed into clean 15 mL Savillex® vials using an analytical balance and digested in two steps following methods based on the clay digestions described by Van Hoecke et al. (2015). A blank and a 50 mg powdered international rock reference used in Li isotope studies, JR-2, from the Geological Survey of Japan were also included in the procedure. In the first step, 9 mL of HF and 3 mL of HNO_3 were added to the vials. The vials were capped and placed on a hotplate set to 110 °C and refluxed for 48 hours. The digests were dried down to incipient dryness by opening the vials and setting the hotplate to a temperature of 80 °C. 12 mL of *aqua regia* was added to the dried residues and placed back on the hotplate set to 110 °C and refluxed for another 48 hours. The digests were dried down again to incipient dryness by opening the vials and setting the hotplate to a temperature of 80 °C. The residues thus obtained were repeatedly dissolved and dried down following repeated additions of HNO_3 and H_2O_2 to target refractory organic phases, and finally diluted ~4000 times in 2% HNO_3 for elemental analysis. Elemental concentrations were measured by an Agilent Technologies 5110 inductively-coupled plasma optical emission spectrometer (ICP-OES) in the geochemistry laboratory of the University of Ottawa. Calibration standard solutions were prepared using certified single element standards purchased from SCP Science (Montreal, Canada). A 1.25 ppm checking standard was prepared to account for any instrument drift during the analytical run.

4.5.2 Clay Separates and Powdered Volcanic Glass Geochemical Characterization

15 mg aliquots of the clay separates were weighed into 2 mL centrifuge tubes and shaken overnight in 1.5 mL 1 M NH_4Cl to remove interlayer, pseudohexagonal, and adsorbed cations. This follows Hindshaw et al. (2019), to leave behind only structurally-bound cations for the digestion step. The mixtures were centrifuged, and the supernatant was carefully pipetted off. Three times, the clay was then re-suspended in Milli-Q water and centrifuged, and the supernatant was carefully pipetted off to remove the exchanged solution. Digestion and analysis of the samples, including the powdered volcanic glass, was then performed by the Geological Survey of Canada, in Ottawa, Canada using ICP-OES and ICP-MS, following four acid (HNO_3 – HF – HCl – $HClO_4$) digestions.

4.6 Lithium Isotopes

4.6.1 Lithium Column Separation Method Development

To measure Li isotopes, Li needs to be separated from the sample matrix using column chromatography techniques, and optimal Li purification depends on the separation of Li from Na (e.g. Misra & Froelich, 2009). For this study, an HCl column method based on the single-column method of Li et al. (2018) was developed to achieve this. Briefly, a Savillex® microcolumn was packed with thoroughly cleaned and conditioned AG® 50W-X8 Cation Exchange Resin (200-400 mesh) and a calibration curve was generated (Figure 8) to locate the Li and Na peaks based on the added volume of 0.2 M HCl eluent after sample loading. The three samples included for this calibration were two claystone digests and a synthetic solution with a matrix composition matched to the digest of the JR-2 Li isotope reference material. Each mL of added eluent was collected and analyzed for Li and Na using an Agilent Technologies 8800 Triple Quadrupole inductively coupled plasma mass spectrometer (ICP-MS) at the University of Ottawa. Calibration standard solutions were prepared using certified single element standards purchased from SCP Science (Montreal, Canada). A 1 ppb checking standard was prepared to account for instrumental drift.

Using the calibration curve, it was determined that to ensure the complete Li recovery needed for isotopic analysis, the Li fraction for each sample needs to be collected from 14 mL to 28 mL elution volume. The sample run was performed in a laminar flow hood. During the run, 1 mL was collected before and after Li fraction collection to check for any drift of the elution curve to ensure complete Li recovery because of column-induced fractionation effects (Misra & Froelich, 2009). The collected 14 mL Li fractions were dried down in a laminar flow hood and refluxed overnight in concentrated nitric acid to remove any resin contaminants. From follow-up ICP-MS analysis, it was determined that procedural blanks were negligible and complete Li recoveries were achieved.

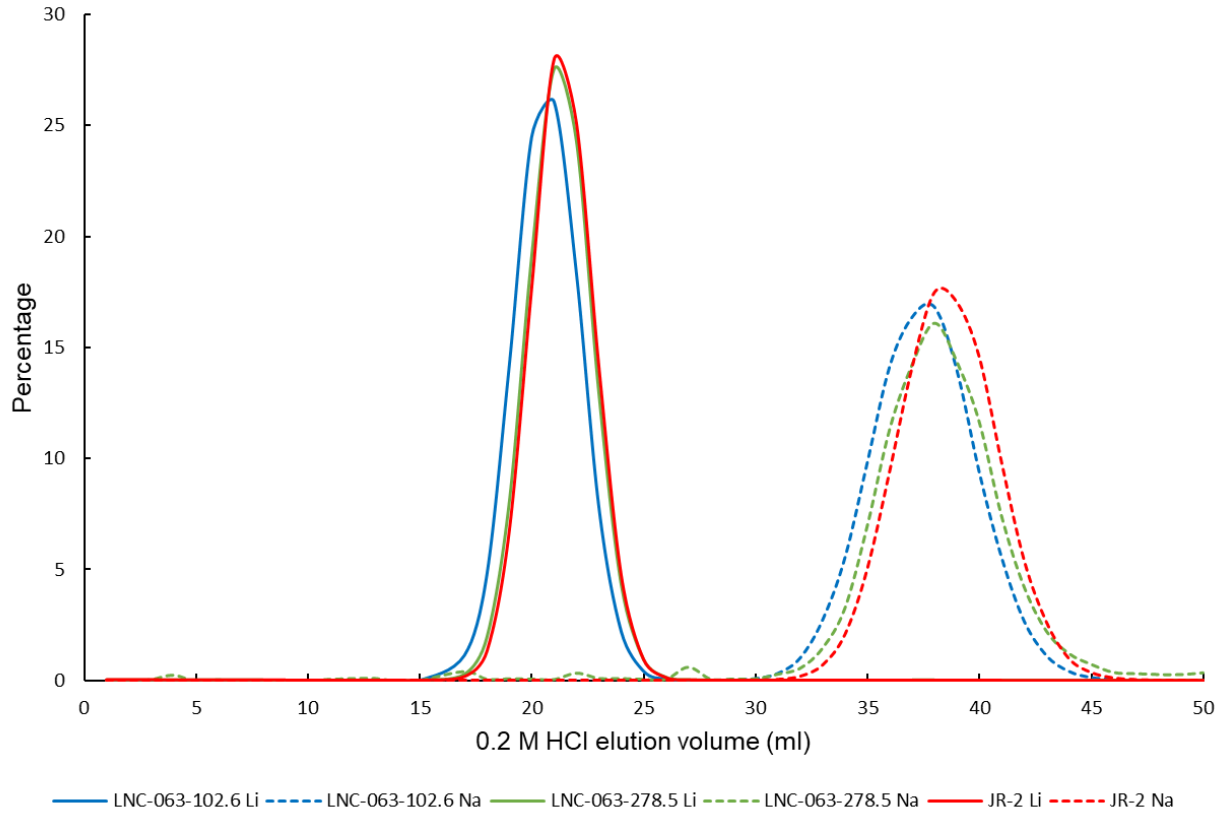

Figure 8. Elution curves of Li (first peak) and Na (second peak) for three samples.

4.6.2 Lithium Isotope Measurements

Dried down Li fractions were submitted to Carleton University for isotopic analysis by a ThermoFinnigan Neptune MC-ICP-MS using a standard-sample-standard bracketing technique with L-SVEC standard solution. The reliability of the analytical procedure was assessed with the JR-2 rhyolite reference material included in the sample suite. A δ^7Li of 4.00 ± 0.22‰ (2SD) was obtained for JR-2, consistent with published data (Ellis et al., 2018; Liu et al., 2018; Magna et al., 2004; Zhu et al., 2020).

5. Results

5.1 Bulk Claystone Characterization

Sample	Depth	Al	Ca	Fe	K	Li	Mg	Na	S	δ^7Li	2SD
L63072	22.1	55,878	61,258	23,478	32,164	377	25,954	32,291	9,020	1.9	0.49
L63102	31.3	82,377	16,688	21,121	4,968	402	30,584	60,705	2,888	7.1	0.06
L63113	34.5	25,530	32,348	15,450	17,638	3,246	96,240	5,103	4,378	6.0	0.40
L63152	46.4	24,649	130,113	11,959	31,707	1,962	55,157	8,726	7,380	3.9	0.61
L63192	58.6	47,363	35,524	19,341	79,429	3,523	28,543	15,128	17,520	-1.5	0.17
L63227	69.3	30,326	33,948	6,674	81,751	5,253	67,393	6,055	2,032	4.7	0.26
L63262	80.1	13,315	71,769	6,125	61,946	6,058	91,494	5,335	5,369	2.0	0.59
L63275	83.9	15,046	80,458	7,665	66,330	7,470	77,268	6,643	4,057	5.6	0.49
L63278	84.9	11,769	51,478	9,748	66,588	8,693	94,552	6,452	5,614	5.7	0.40

Table 2. Depth below ground surface (m), concentrations of analyzed major ions (ppm), and Li isotopes (‰) of claystone samples from core LNC-063.

Bulk samples analyzed in this sample suite reach Li concentrations up to 8,693 ppm at depth in the more illite-rich samples (Table 2.), consistent with previous published measurements of bulk samples (Castor & Henry, 2020; Ingraffia et al., 2020; Morissette, 2012). Reproducing the stacked XRD pattern of Castor & Henry (2020) using these samples displays the same observed gangue mineralogy, a smectite to illite clay transition with depth, and the alteration mineralogical zones of analcime, K-feldspar, and albite (Figure 9). Li concentrations of bulk claystone samples are affected by the quantity of Li-bearing Mg-clays and the Li enrichment within the Mg-silicate structure itself. Sample L63192 at depth of 59 mm has notably high S concentrations, the strongest albite peak, and has both a smectite and illite peak, indicating two separate phases (not mixed-layered). This sample also has the highest Li/Mg ratio (0.12) of the sample suite and is consistent with the ratio calculated from previous measurements of the most Li-rich, tainiolite-like illite phase observed at Thacker Pass (Castor & Henry, 2020; Morissette, 2012). There are strong calcite XRD peaks for all samples, except in the two dolomitic samples where only a minor peak can be identified. Al, Ca, Fe, Na and S are from gangue minerals, the majority of Mg and Li are from the Li-clays, Al and Na is mainly associated with tuffaceous material and Al-silicate alterations, K is found in K-feldspar and the Li-illite phase at depth, and S is in pyrite (e.g. Castor & Henry, 2020). Samples L63102 and L63113 contain dolomite, therefore a portion of the measured Mg is sourced from this carbonate phase (Castor & Henry, 2020).

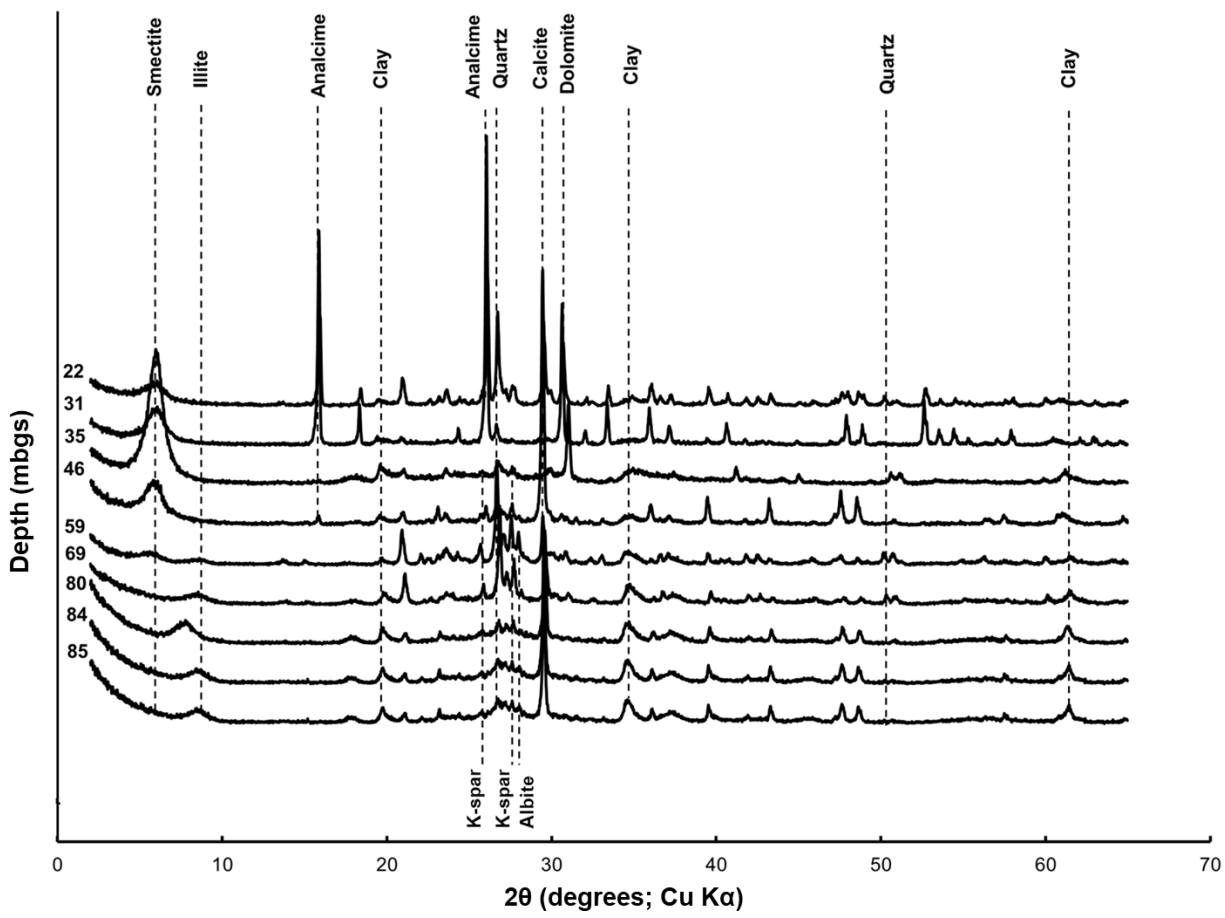

Figure 9. Stacked XRD patterns and labelled major mineral peaks for bulk claystone intervals from 22 m to 85 m depth below ground surface (mbgs) from core LNC-063, based on Figure 9. from Castor & Henry (2020) for a different drill core from Thacker Pass. Separate smectite and illite 001 peaks are labelled, and other major clay (labeled "Clay") peaks combine overlapped smectite and illite peaks. The clay peaks are noticeably broad, especially for samples at depths of 58.6 and 69.3 m.

The Li isotope signatures from claystones have δ^7Li values that range from -1.5 to 7.1‰. The depth profile shows an irregular pattern with no clear trends (Figure 10). Using Li/Mg ratios to normalize Li enrichment within the Mg-silicate phases also show no trends, however the most Li-enriched and illitic sample has the most depleted δ^7Li (-1.5‰). The most enriched δ^7Li (6.0 and 7.1‰) is found within the upper dolomite-bearing layer identified here and by Castor & Henry (2020). The most Li-enriched sample also has almost double the S concentration (17,520 ppm) of the next richest in S sample (9,020 ppm). From a representative thin section to be unveiled in a further section focused on general photomicrography, this sample contains abundant pyrite framboids, observable angular glass-shards, calcite and fluorite. There is a moderate trend between δ^7Li and S concentration (Figure 10.) The F concentrations that have been found to correlate with Li (Castor

& Henry, 2020; Ingraffia et al., 2020) have not been measured here because of hydrofluoric acid use in digestions, but fluorite has been observed in thin sections that contain the most Li-enriched illite phase like Castor & Henry (2020) and Ingraffia et al. (2020).

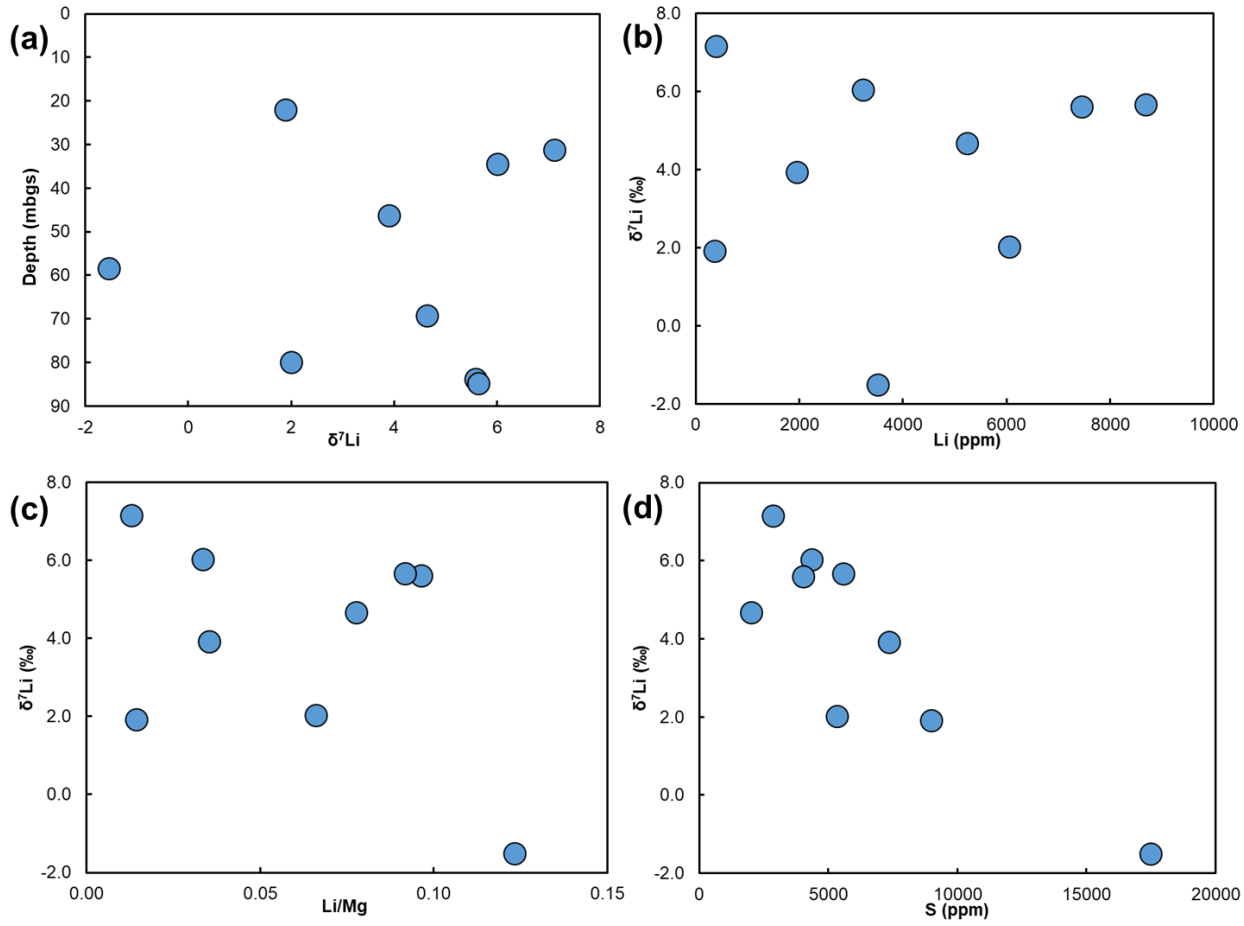

Figure 10. Lithium isotopes of claystones from Thacker Pass. (a) Li isotope depth profile. (b) Li isotope and claystone Li concentrations. (c) Li isotope and claystone Li/Mg ratio to quantify Li enrichment in Mg-silicate structure (please note that measurements for the two most depleted δ^7Li samples include Mg from dolomite). (d) Claystone Li isotope and S concentrations from presence of sulfides.

5.2 Clay Separates Characterization

Sample	Depth	Al	Ca	Fe	K	Li	Mg	Na	Li/Mg
L01088	26.8	25,459	35,187	30,083	3,805	498	30,821	10,719	0.016
L01162	49.3	25,647	65,845	44,775	6,425	998	77,808	10,516	0.013
L01205	62.5	38,407	12,956	69,108	785	326	84,417	6,032	0.004
L01222	67.7	16,115	972	15,015	8,588	3,004	138,315	3,254	0.022
L01260	79.2	18,092	798	13,259	5,765	1,740	128,230	4,622	0.014
L01272	82.9	11,761	391	12,435	9,109	4,272	121,587	2,854	0.035
L01282	86.0	35,816	694	14,710	41,590	2,655	92,463	3,759	0.029
L01305	93.0	12,064	983	17,692	36,019	6,178	120,031	3,543	0.051
L01306	93.4	9,432	263	15,388	23,420	6,064	124,004	2,809	0.049
L01321	98.0	8,706	437	5,007	36,582	7,110	123,063	3,910	0.058
L01322	98.1	5,763	321	2,185	33,939	6,334	127,067	4,780	0.050
L01352	107.2	8,828	7,092	4,716	53,563	9,749	107,546	5,976	0.091
L01469	123.9	8,198	225	7,254	59,626	9,638	118,808	1,248	0.081
L01513	143.0	12,239	585	11,143	43,327	5,890	125,238	1,054	0.047

Table 3. Depth below ground surface (m), concentrations of analyzed major ions (ppm), and Li/Mg ratios of clay separates from core LNC-001.

Analyses from clay separates of Thacker Pass (Table 3) minimizes the Al, Ca, Fe, K, and Na inputs from the gangue minerals, although some are still present in the < 2 µm fraction from error resultant from separation by syringe method and from contributions of Al-silicates that are < 2 µm. Much like saponite, some Al and Fe likely is structurally bound within the Li-bearing Mg-silicates, like Morissette (2012) found. In general, the data here is consistent with analyses of the < 2 µm fraction of Morissette (2012), although Li concentrations reach a maximum concentration of 9,638 ppm rather than 12,400 ppm. From the bulk and clay separates data, Morissette (2012) likely performed the separation on a bulk sample similar to bulk sample L63192 (Table 2), with a Li/Mg ratio of 0.12.

Li, interlayer K, and Li/Mg gradually increase with depth, and decrease near the base of the section. This is consistent with the order with depth of smectite → illite/smectite → illite → illite/smectite described by Castor & Henry (2020), because higher Li concentrations are found in the tainiolite-like illite phase that is more common in the deeper sections. The mixed sections have low to moderate Li concentrations (Castor & Henry, 2020). From clay separates chemistry, the smectite to illite transitions are observable by plotting Li, K, and Li/Mg concentrations with depth (Figure 11).

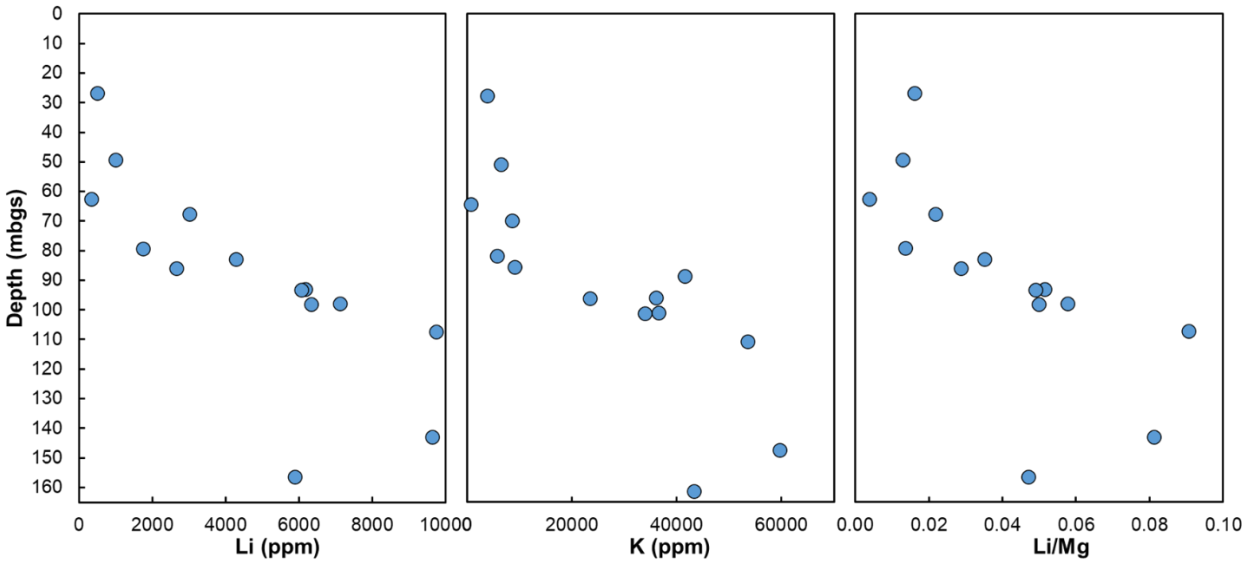

Figure 11. Depth below ground surface (m) and concentrations of Li, K and Li/Mg ratios of clay separates from core LNC-001.

Oriented powder XRD measurements of ethylene glycol-solvated samples with intermediate interlayer K concentrations (< 50,000 ppm) confirm the presence of mixed layering of illite and smectite. Using the techniques of Moore & Reynolds (1997), Reichweite (R) ordering is estimated from the position of the glycolated 001/002 reflection, and percent illite from the position of the 002/003 reflection. A table of analyzed samples is presented below with Li and K concentrations included for comparison. A diffraction pattern has been included on the next page (Figure 12), and the rest of the patterns used to generate the table can be found in Appendix A.

Sample	Depth	From digestion		001/002	002/003	From XRD pattern	
		Li	K	d(Å)	d(Å)	% Illite	Reichweite
L01088	26.8	498	3,805	8.33	5.59	20	0
L01162	49.3	998	6,425	8.27	5.50	40	0
L01222	67.7	3,004	8,588	8.42	5.58	20	0
L01305	93.0	6,178	36,019	9.36	5.24	75	1
L01321	98.0	6,334	36,582	9.16	5.29	70	1
L01513	143.0	5,890	43,327	9.29	5.30	70	1

Table 4. Depth below ground surface (m), concentrations of Li and K (ppm), positions of XRD reflections useful for estimating percent illite in mixed-layered clay minerals, percent illite and Reichweite (R) ordering (Moore & Reynolds, 1997).

As seen Table 4 above, samples L01088 and L01222 both yield ~20% illite from the XRD pattern, yet L01222 holds more than double the K in its interlayer. This highlights that the methods of

Moore & Reynolds (1997) are an estimation and are likely less accurate than percent illite estimates from K concentrations of NH_4^+-saturated clay separates, however it is the only method where it is possible to identify mixed-layering rather than a mix of separate smectite and illite phases.

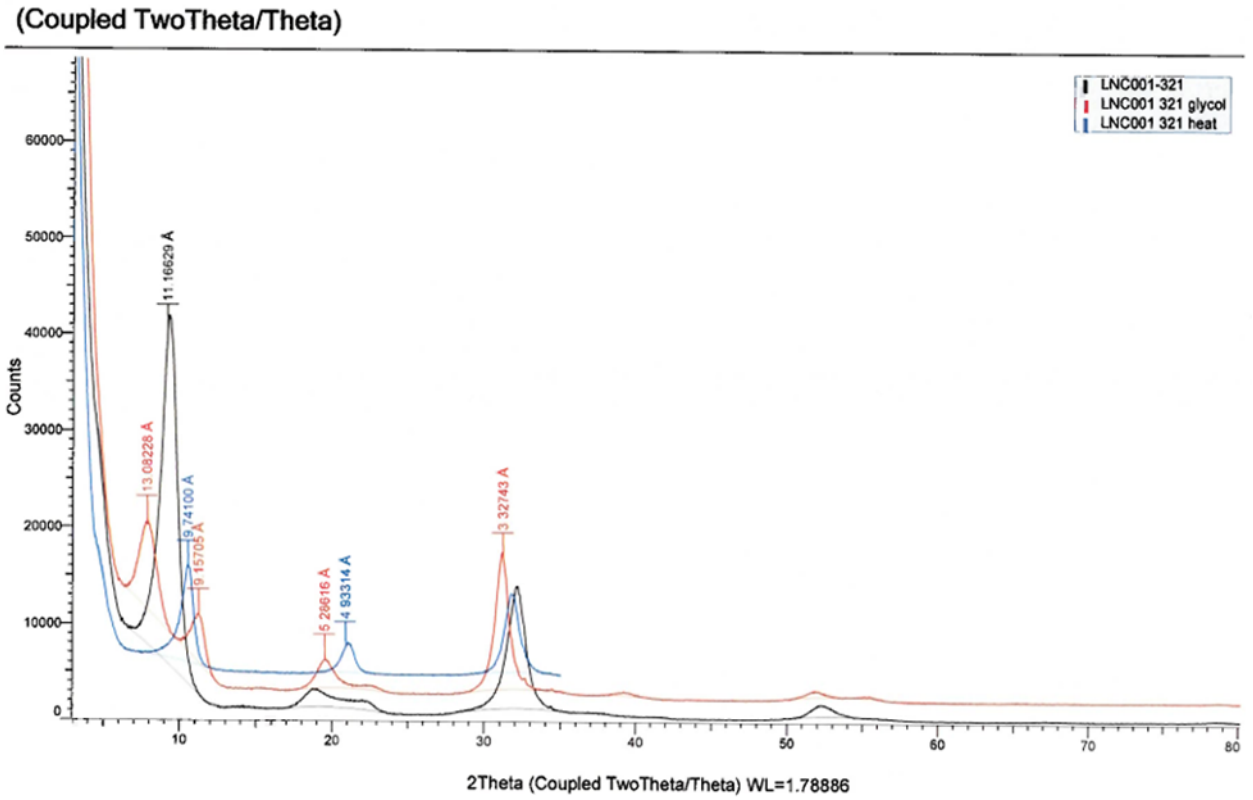

Figure 12. XRD pattern of oriented mixed-layer clay separates sample L01321 extracted from core LNC-001. Black line indicates scan of air-dried sample. Red line indicates scan of sample in ethylene glycol solvated state. Blue line indicates scan in final heated state following heating to 550°C in a muffle furnace. This mixed-layer clay is composed of 70% illite and 30% smectite according to the methods of Moore & Reynolds (1997).

From these oriented XRD patterns, a Kübler index of ~1.5 can be obtained from the half-peak-width values of the 001 illite reflection peak (Warr, 2019). This measurement classifies the illite crystallinity as poorly crystalline and above the shallow diagenetic temperature zone (Verdel et al., 2011; Warr, 2019). The poorly crystalline nature of the illite at Thacker Pass has also been identified in SEM imagery by Morissette (2012) and Castor & Henry (2020).

5.3 Photomicrography

This section presents observations of representative thin sections from claystones of Thacker Pass, these include the upper hectorite section, the dolomite-bearing section, the high Li-grade and more illitic section, and the lowermost section that features illite-smectite mixed-layers.

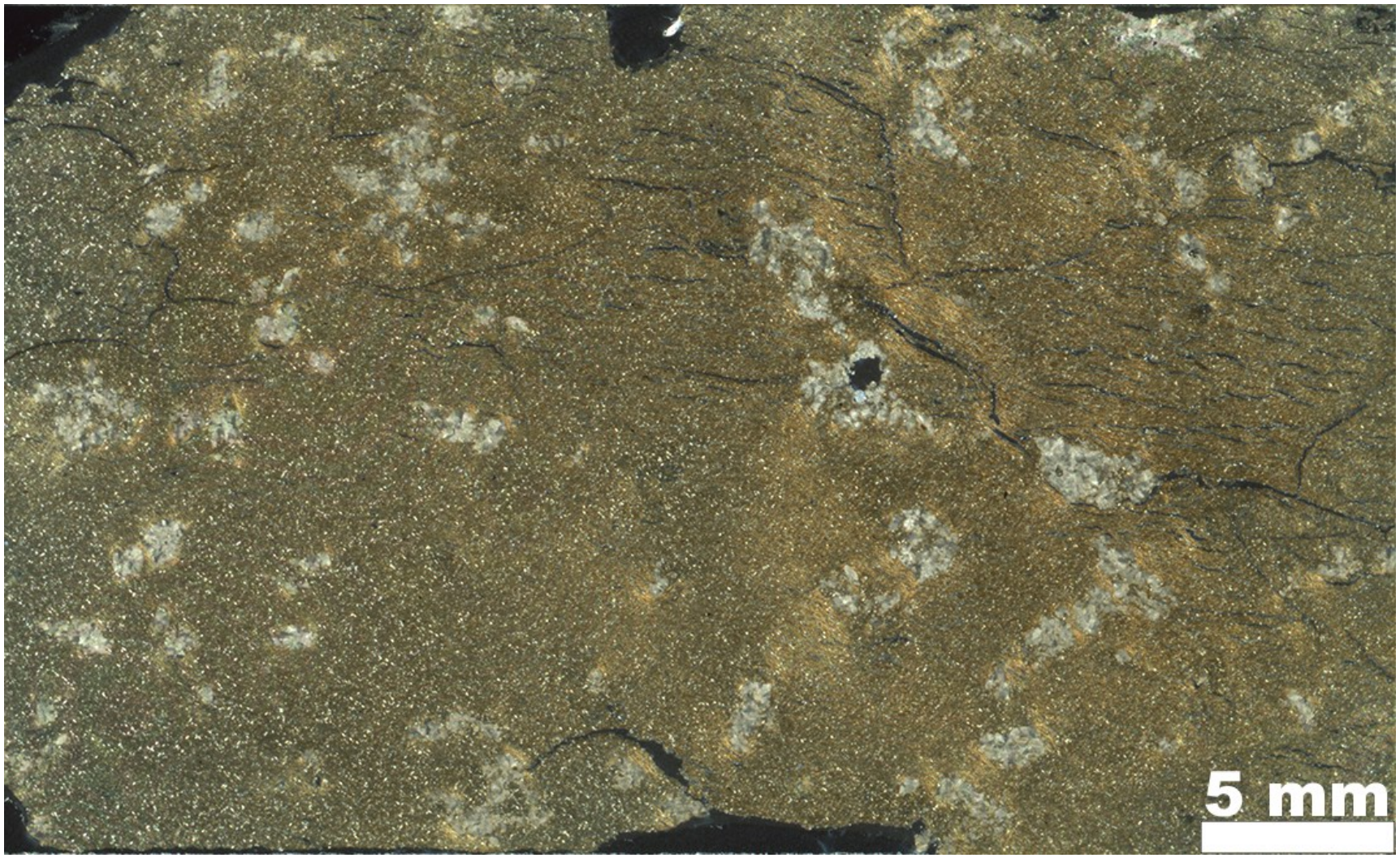

Figure 13. Cross-polarized thin section scan of hectorite-bearing claystone from upper section. Li-clay matrix (brown and tan) with calcite spherulitic-like nodules (grey), disseminated analcime and fibrous microcrystalline quartz (white). Large black sections are porosity. Please see appendix B for plane-polars version.

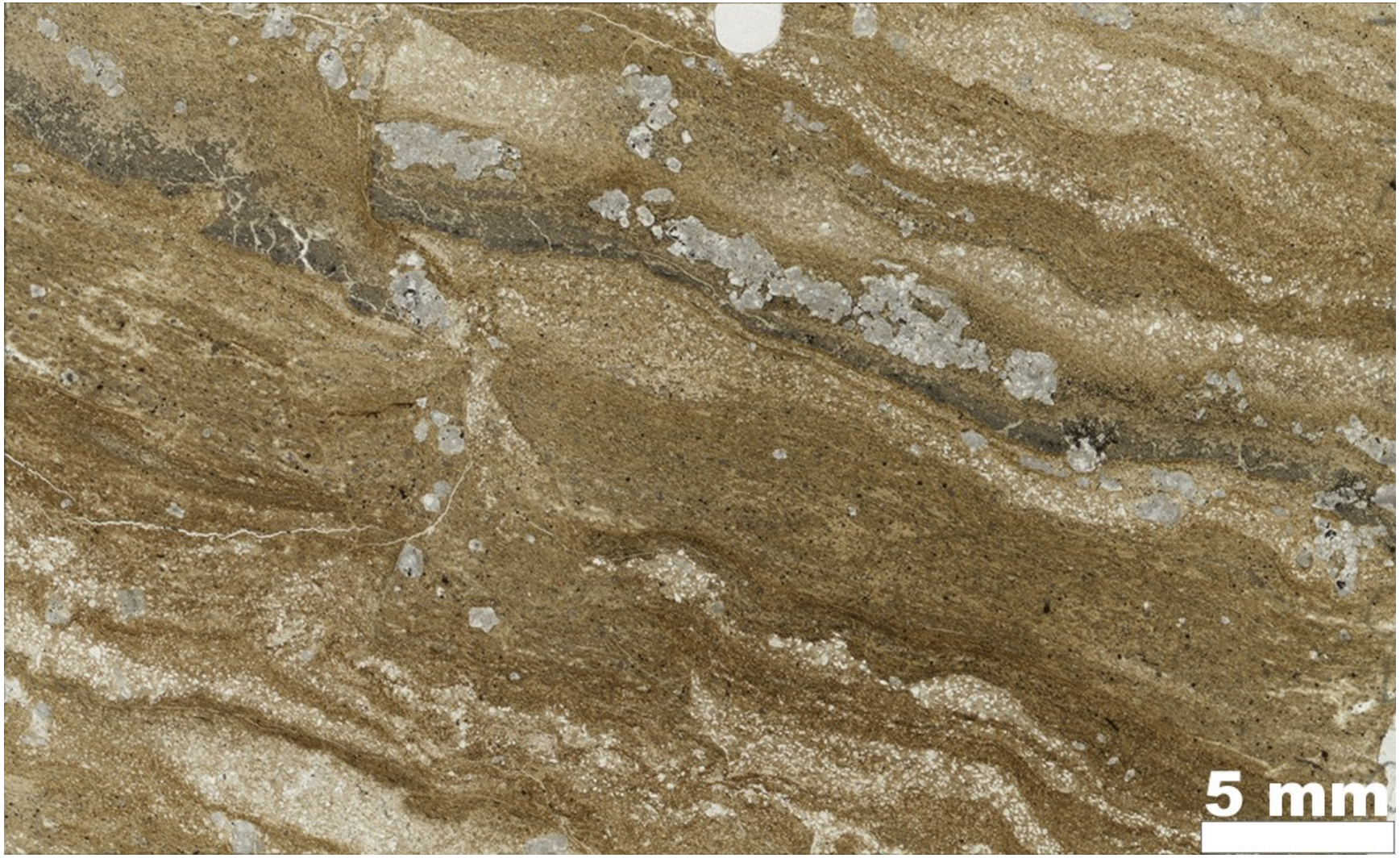

Figure 14. Plane-polarized thin section scan of tilted hectorite-bearing laminated claystone from upper section. Li-clay matrix (brown) and quartz (white) layers with seemingly floating spherulitic-like calcite nodules (light grey), and aggregations of these on a thin normal faulted and desiccated altered volcanic ash layer (dark gray). Sub-mm pyrite framboids (black spheres) are disseminated throughout and form localized groups in areas and as inclusions within some of the calcite nodules. The calcite distribution and the irregular crenulated contacts between each layer show plastic deformation and a gel-like texture. Please see appendix B for cross-polars version.

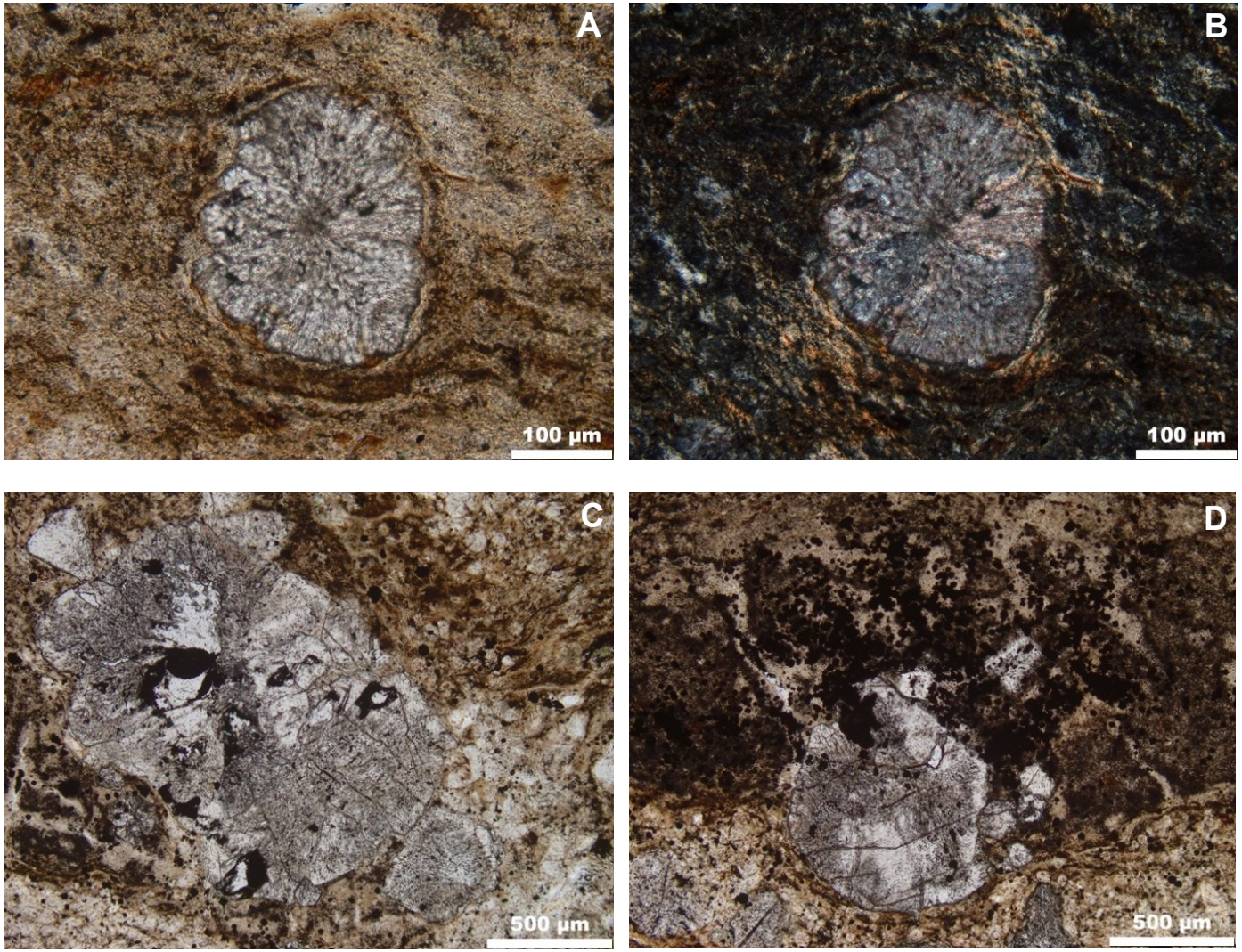

Figure 15. Photomicrographs of spherulitic-like calcite nodules set in hectorite matrix of claystone shown in Figure 14. All in plane-polars view, except B in cross-polars view. A and B show a clear radial fibrous microstructure to the calcite, C and D have similar fibrous microstructures with a less obvious radial component. C is composed of multiple aggregated calcite nodules. Groupings of framboidal pyrite (black) are found within the hectorite and as inclusions within the calcite nodules. The largest population of pyrite framboids is found branching out directly above the calcite nodule found in D.

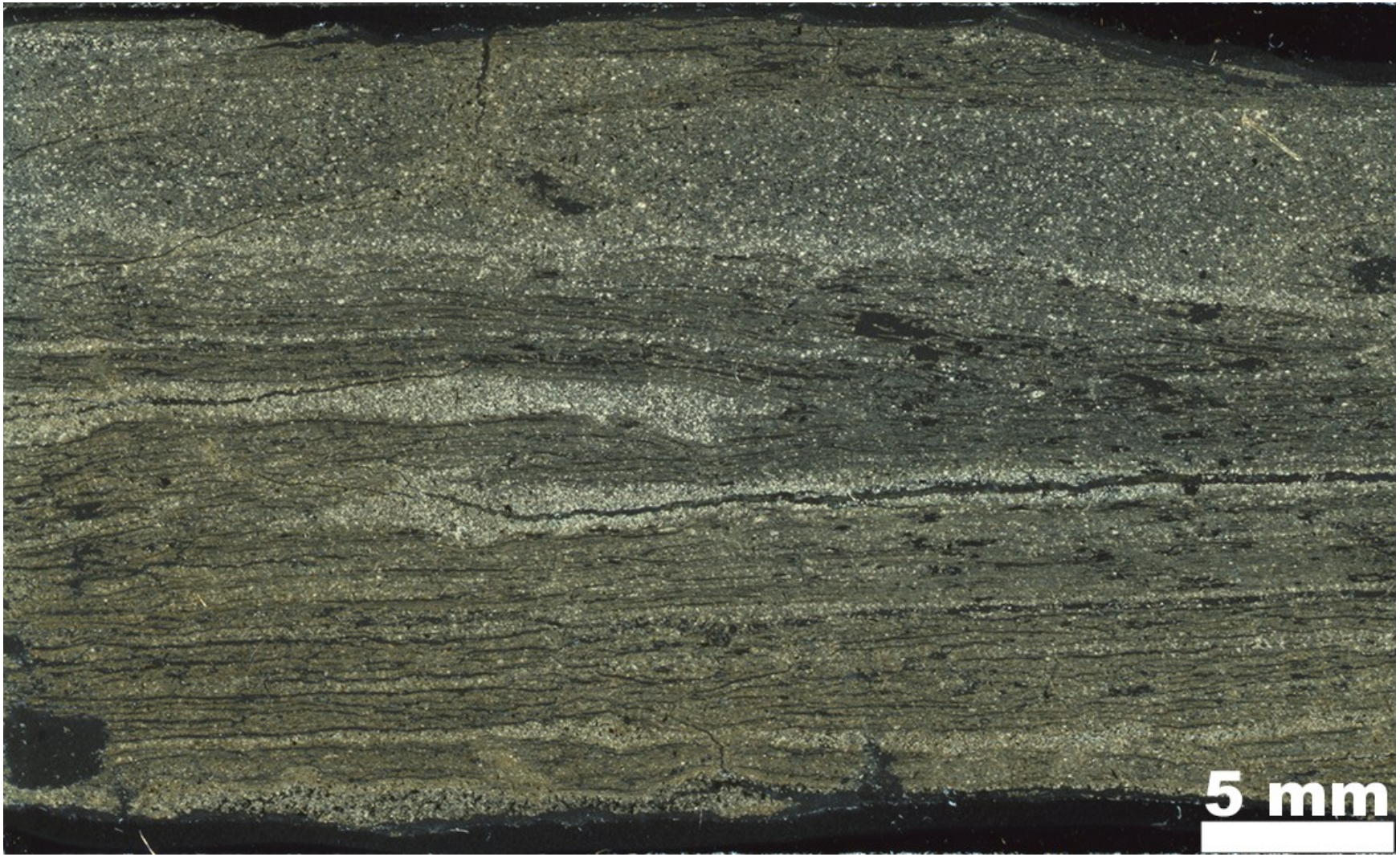

Figure 16. Cross-polarized thin section scan of laminated claystone from dolomite-bearing section. This is a split from bulk sample L63113 with a δ^7Li of 6.0 ± 0.40‰. Hectorite matrix (greenish brown) with microcrystalline dolomite layers (white) in areas associated with porosity from Mg-silicate dissolution (most black sections) and porosity-filling bitumen/pyrite accumulations (black). Please see plane-polars version in appendix B for distinction between opaques and porosity.

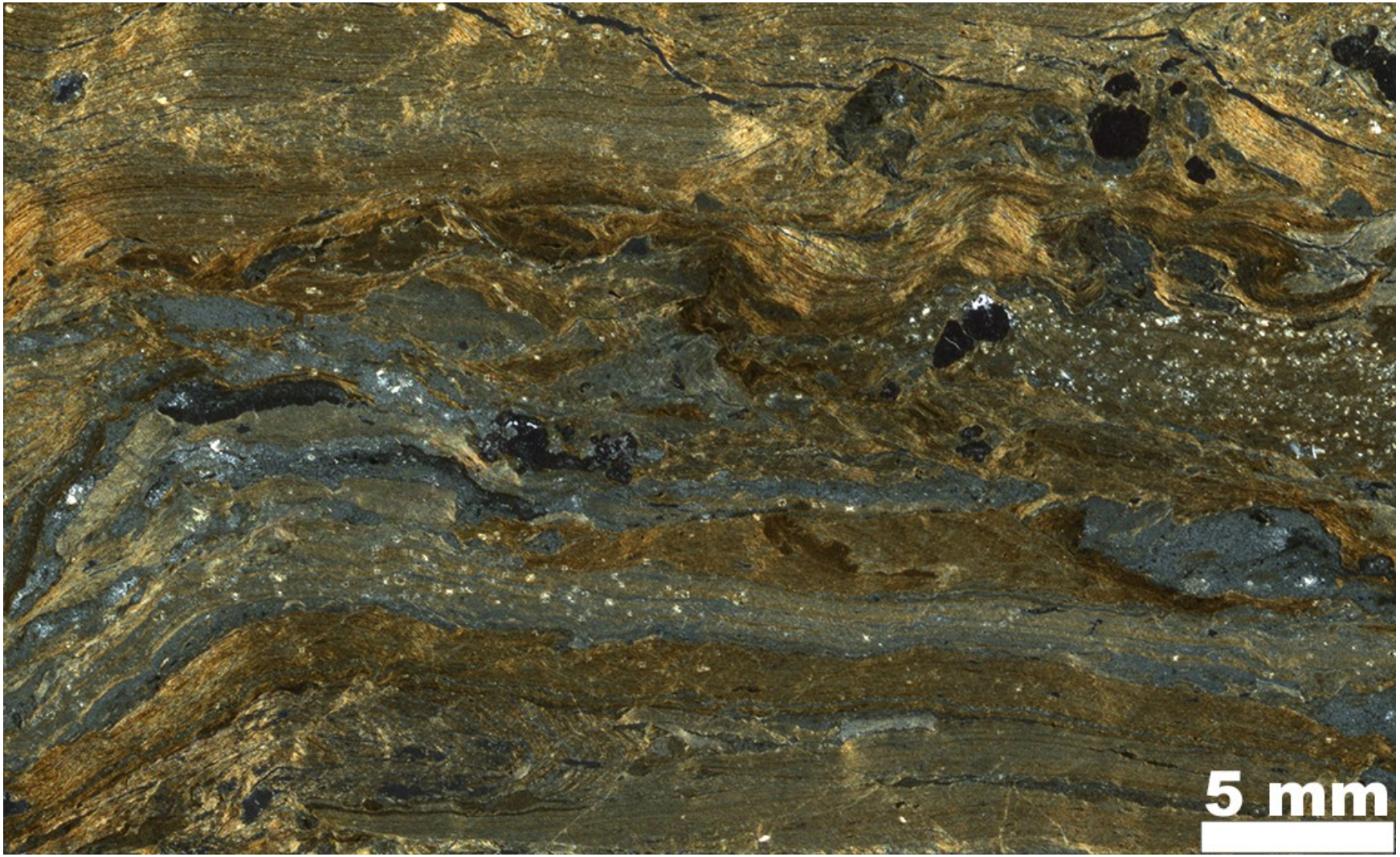

Figure 17. Cross-polarized thin section scan of illite-bearing laminated claystone. This is a split from clay separates sample L01352 with Li concentration of ~1%. Shows laminated illite matrix (tan and brown), silicification by fibrous microcrystalline quartz that is often botryoidal (grey and white) and by diffuse quartz veinlets (dark grey). Fluorite pseudomorph of calcite nodules (isotropic black nodules, shown in plane-polars view on next page). The Li-clay here is the most birefringent in the sample suite and is representative of the Li-bearing illite. The irregular contacts between each contorted layer and the folded nature show plastic deformation and a gel-like texture. Please see appendix B for plane-polars version.

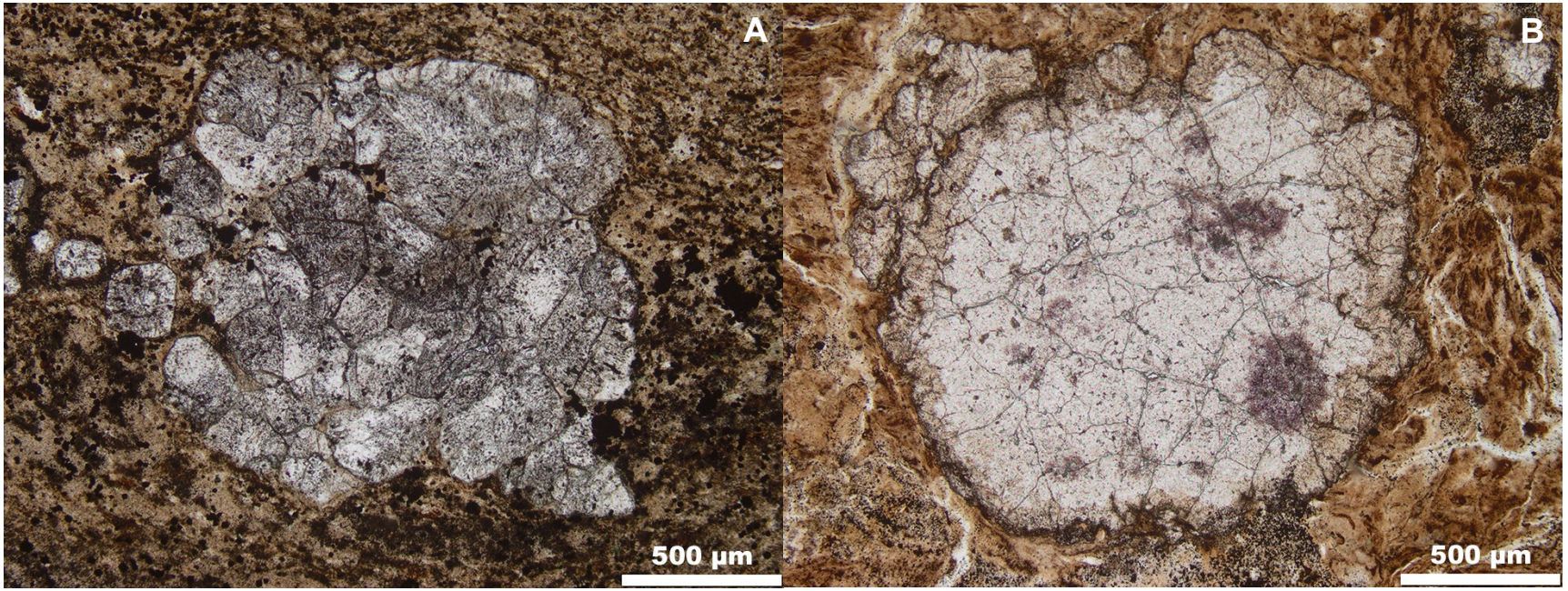

Figure 18. Calcite and fluorite morphology. Plane-polarized photomicrograph of calcite nodule aggregates in hectorite (tan) (A) from Figure 14 and fluorite pseudomorphs of calcite nodule aggregates in illite matrix (brown) (B) from Figure 17. Both contain framboidal pyrite that form mottled patches, although B are of smaller size. The pyrite in B appears to be associated with quartz veinlets (white).

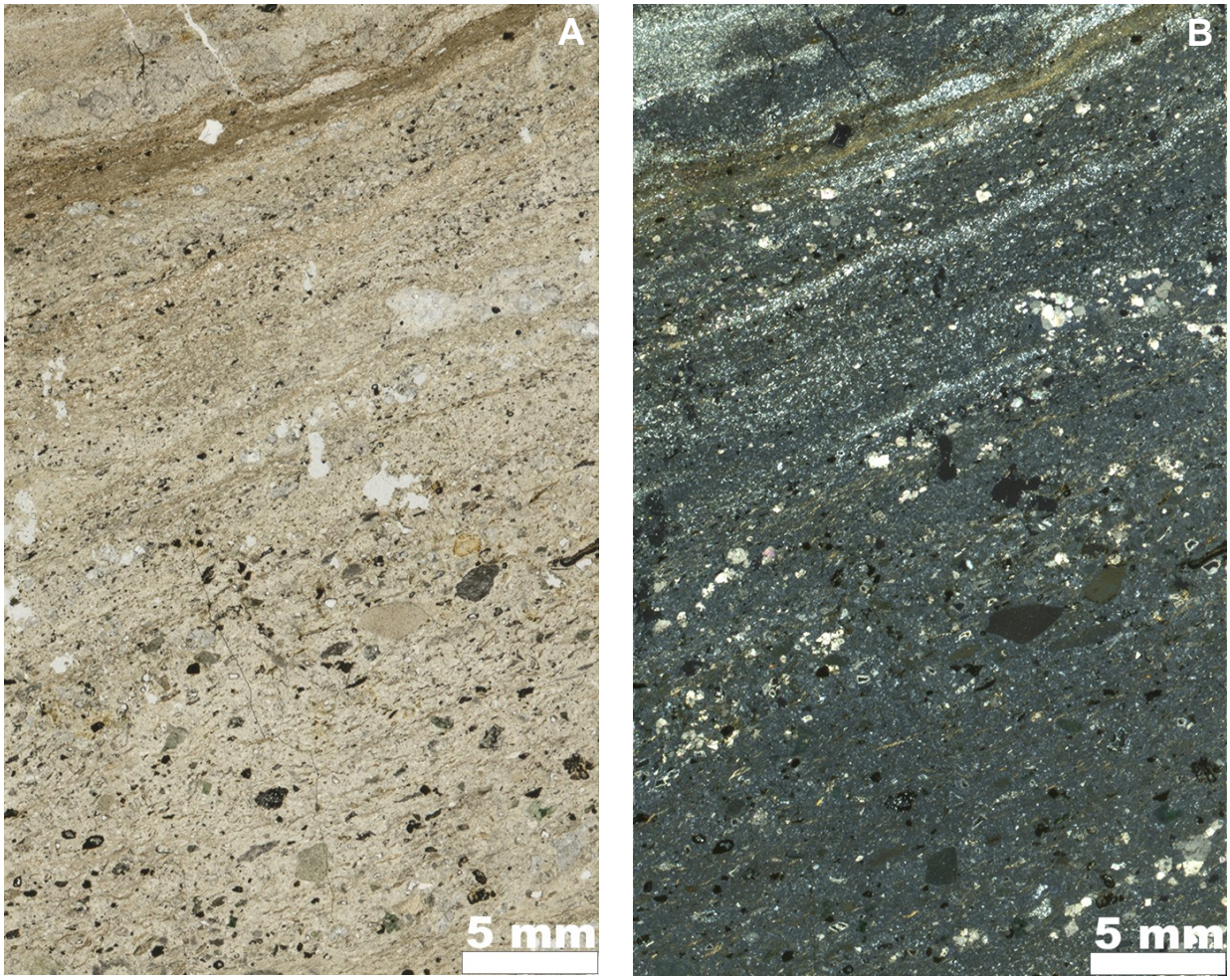

Figure 19. Plane-polarized thin section scan (A) and cross-polarized version (B) of illite-bearing laminated claystone. This is a split from bulk sample L63192 with a δ^7Li of -1.5 ± 0.17‰, the highest Li/Mg ratio (0.12), and the most S-rich. Illite (brown) and abundant pyrite framboids (black in plane-polars and cross-polars) coat angular volcanic glass shards near the base of the thin section. Calcite nodules (white in plane-polars and high birefringence in cross-polars), and fluorite (white in plane-polars and isotropic in cross-polars). Fine quartz layers are also present (white fine-grained layers in cross-polars). From XRD pattern of the split, the very fine grain grey material is largely composed of albite, some K-feldspar, and possibly microcrystalline quartz.

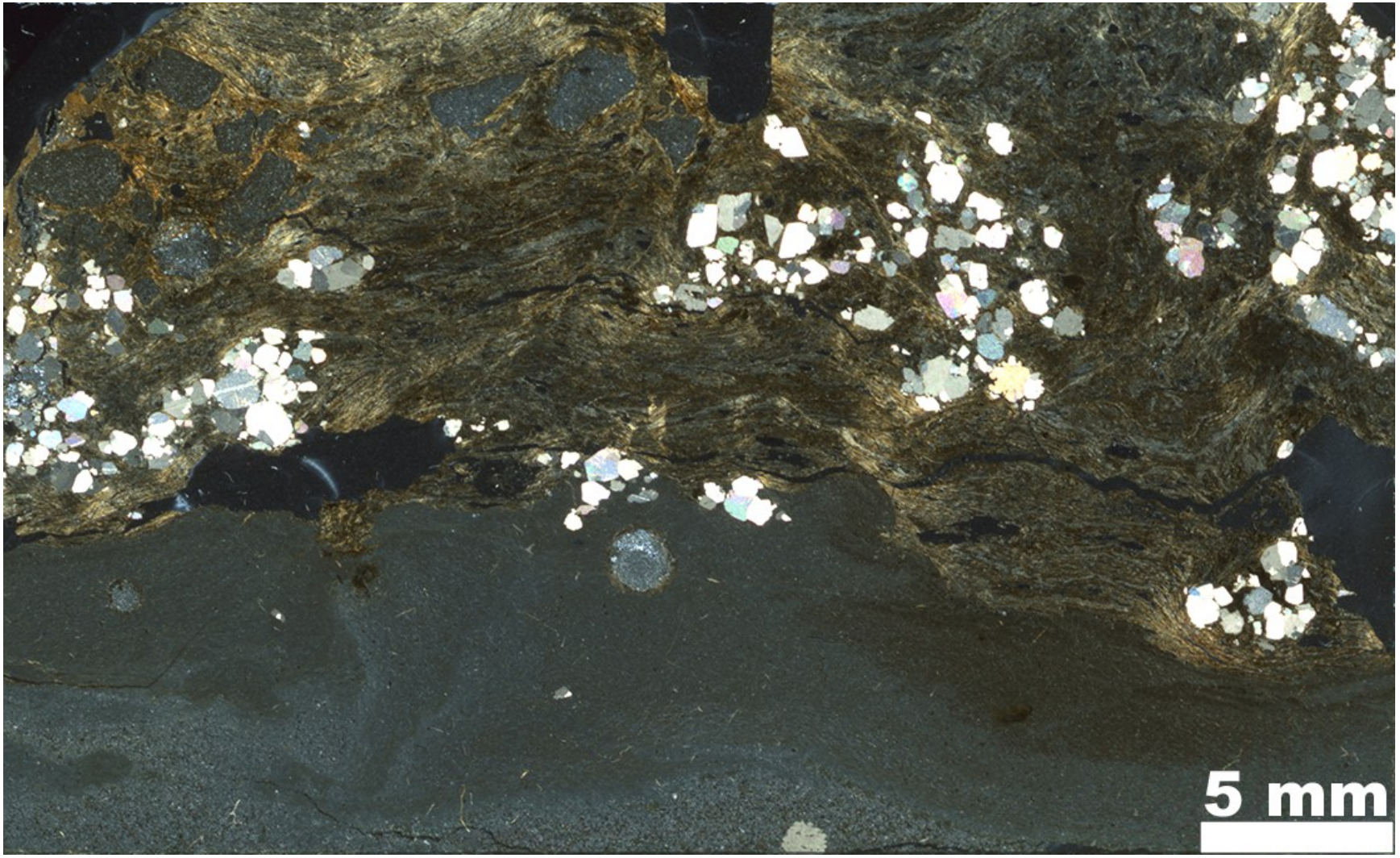

Figure 20. Cross-polarized thin section scan of lowermost mixed-layer illite-smectite claystone. Li-clay (tan and brown) silicification by fibrous microcrystalline quartz (dark grey) as 1-2 mm nodules and at a large scale in the lower half of the thin section. Lowermost coarsening of crystals may be from Al-silicate altered volcanic ash layer. Calcite crystals (high birefringence) have a higher birefringence and lack microstructures compared to the fibrous nodules found in the shallower claystone samples and appear to be a Li-clay replacement feature like the microcrystalline quartz nodules. Please see appendix B for plane-polars version.

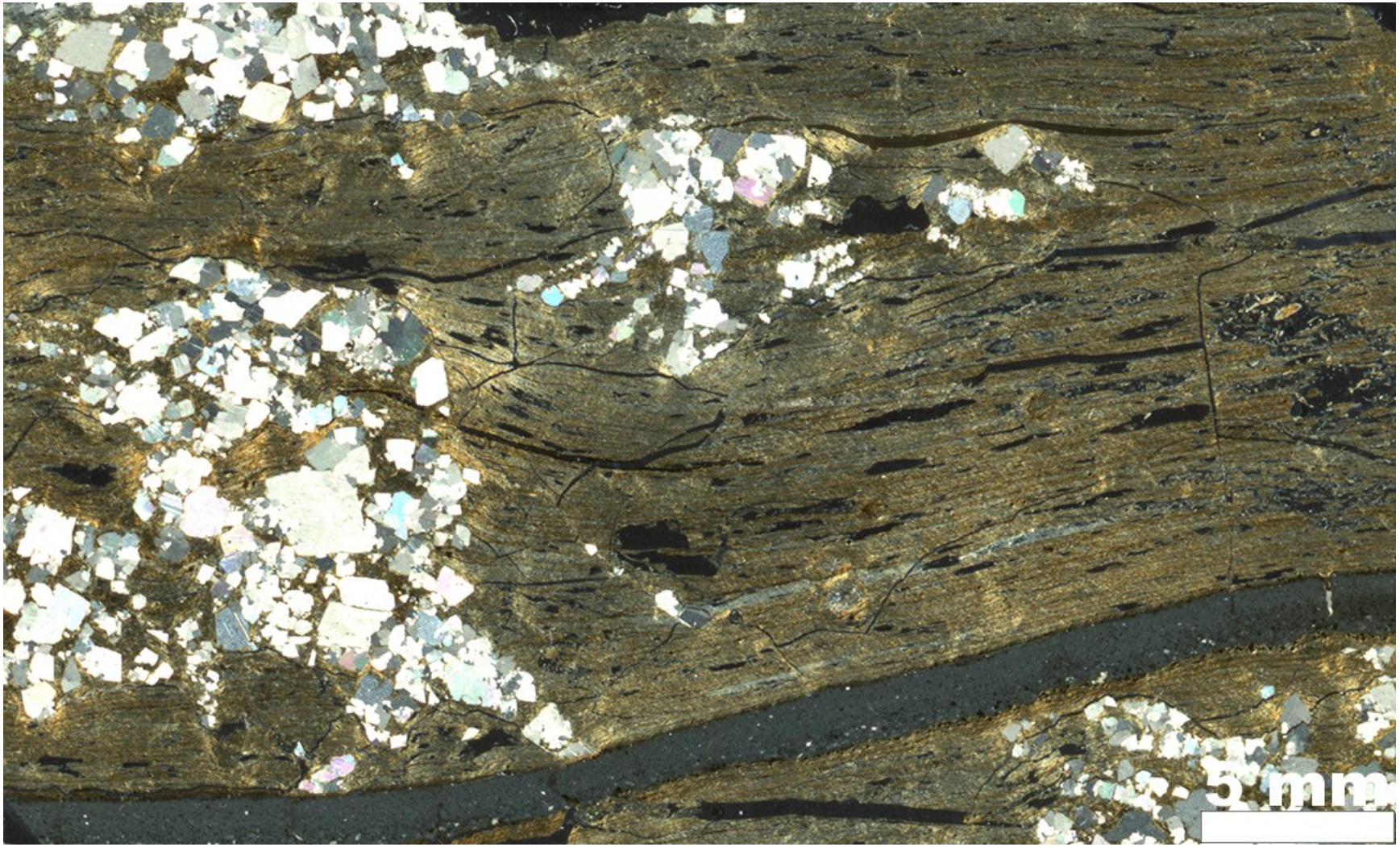

Figure 21. Cross-polarized thin section scan of lowermost mixed-layer illite-smectite claystone. This is a split from bulk sample L63275 with a δ^7Li of 5.6 ± 0.49‰. Li-clay (tan and brown), rhombohedral calcite crystals (high birefringence), and a 2 mm layer of silicified volcanic ash (grey) with finely disseminated euhedral pyrite (black). The planar arrangement of the calcite crystals in many areas and the presence of horizontal sections of fenestral porosity (horizontal black) indicates that the calcite is likely porosity filling. Please see appendix B for plane-polars version.

5.3.1 Photomicrography Summary

From examination of thin sections, carbonate phases are ubiquitous and appear to be closely related to the Li-bearing clays. The fibrous calcite nodules closely resemble the spherulitic calcite associated with Mg-clays identified in ancient alkaline volcanic deposits like the Barra Velha Formation (e.g. Mercedes-Martín et al., 2017; Saller et al., 2016; Wright & Barnett, 2015). Thin section splits of the samples with a δ^7Li of -1.5 ± 0.17‰ (Figure 19) and a δ^7Li of 6.0 ± 0.40‰ (Figure 16) appear vastly different, with the most depleted δ^7Li showing a more obvious volcanic influence by presence of angular volcanic glass shards. There is no evidence from the thin sections that the clays are altered tuffaceous sediments like suggested by Castor & Henry (2020), nor could Li-illite hydrothermal veinlets be identified like Ingraffia (2020) and Ingraffia et al. (2020). From a higher magnification, it could be plausible to interpret the illite phase as a veinlet when the illite matrix is undergoing silicification by fibrous quartz (Figure 22), although this is misleading because the microcrystalline quartz is not a "wall rock".

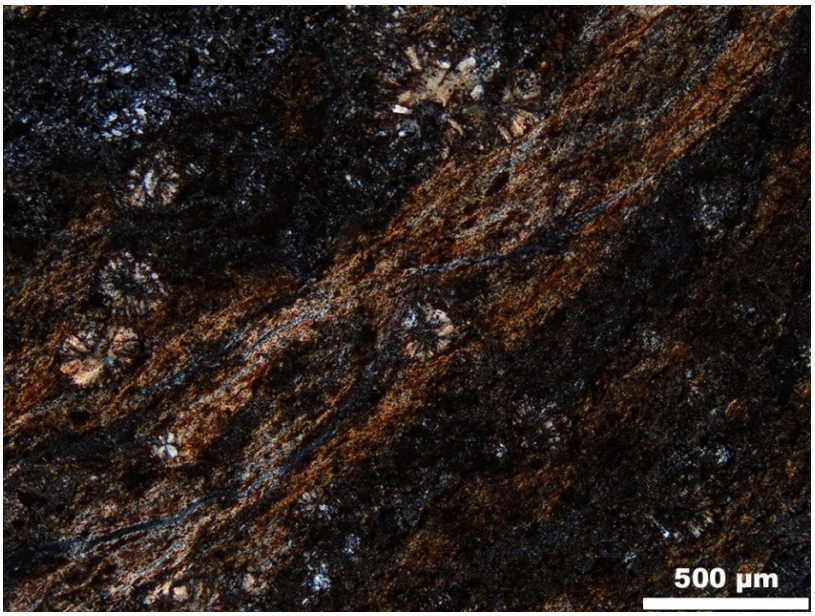

Figure 22. Cross-polarized photomicrograph of silicification of Li-illite (brown) by microcrystalline fibrous quartz (white and grey) from Figure 17. Botryoidal texture of fibrous quartz overlapping Li-illite indicates that this is a replacement process.

Morissette (2012) also identified many "fragments" in the thin sections of the McDermitt Caldera that closely resemble nodular silicification by fibrous microcrystalline quartz (Figure 20). These observations suggest that under certain conditions, the Li-bearing ore could be replaced by other phases during diagenesis, rather than it being a replacement of tuffaceous sediments.

6. Discussion

6.1 Li Isotopes and Fractionation Factor

The Li isotope signatures from the highly Li-enriched claystones have δ^7Li values that range from -1.5 to 7.1‰. These values are consistent with the δ^7Li range of the shallow brines and thermal waters of the active Central Andes, where economically important Li brine resources are currently being exploited in hyperarid salars like the Salar de Atacama and the Salar de Olaroz (Alvarez-Amado et al., 2022; Garcia et al., 2020; Godfrey et al., 2019; Munk et al., 2018). There is no correlation between Li concentration and δ^7Li at Thacker Pass, unlike the Li brine resources that feature increasing Li concentrations with increasing δ^7Li, and heavier 8.1 to 12.6‰ values measured in the most Li-rich brine ores that reach concentrations up to ~5000 ppm at depth as Li infiltrates, accumulates and ages within the halite/evaporite aquifers during evapoconcentration (Garcia et al., 2020; Munk et al., 2018). Despite concentrations up to ~10000 ppm Li in the clay structure and the massive volume and lateral extent of this mineral-hosted resource, little isotopic distillation in the ore-generating fluid occurred, considering that clay preferentially sequesters ^{6}Li during formation (Huh et al., 1998). The irregular pattern in the Li isotope depth profile contrasts with the smooth Li enrichment pattern recorded in the clay-separates, suggesting ore formation did not occur by migration of reactive altering fluids through a tuffaceous sediment section during diagenesis, as previously suggested (Castor & Henry, 2020; Ingraffia et al., 2020). The low Al concentrations in the clays and photomicrography observations also do not support that the clays are altered tuffaceous sediments (e.g. Millot, 1970).

Very poor illite crystallinity, evidenced by a Kübler index of ~1.5, warrants the use of the low-temperature (20°C) octahedral site-specific fractionation factor (-21.5 ± 1.1‰) determined by Hindshaw et al. (2019) to decrypt the isotopic composition of the mineralizing paleofluid. The isotopic composition of the evolving water from clay formation in the McDermitt Caldera can be defined by the Rayleigh fractionation equation (Clark, 2015):

$$\delta^7\mathrm{Li}_w = \delta^7\mathrm{Li}_i + \varepsilon^7\mathrm{Li}_{c-w} \times \ln(f) \qquad \text{[Equation 4.]}$$

Where $\delta^7\mathrm{Li}_w$ is the evolving isotopic composition of the lake water, $\delta^7\mathrm{Li}_i$ is the initial isotopic composition of the water, $\varepsilon^7\mathrm{Li}_{c-w}$ is the fractionation factor, and $\ln(f)$ is the residual Li fraction in water.

Applying the fractionation factor yields paleofluid δ^7Li compositions that range from 20.0 to 28.6‰, ranking them as more δ^7Li enriched than the Li brines of the Salar de Atacama, and almost as evolved as modern seawater (Figure 23).

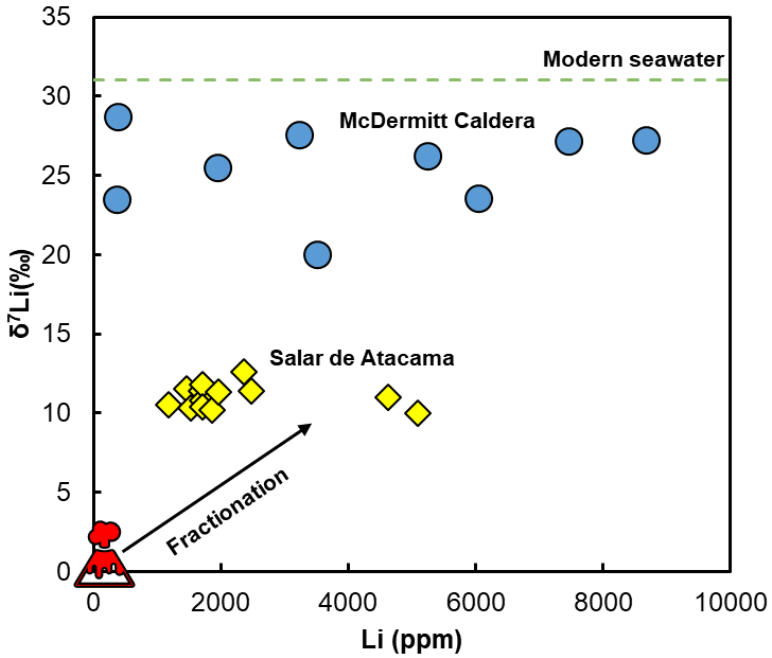

Figure 23. Paleofluid δ^7Li composition relative to Li concentration in bulk claystones, contextualized with data from δ^7Li enriched Li brines ores of the nucleus of the Salar de Atacama (Munk et al., 2018) and the ~0‰ volcano-hydrothermal ~40 ppm Li source to the salar (Alvarez-Amado et al., 2022).

Having Li-clay mineralization from continental brines that are almost as evolved as seawater, with an absence of characteristically volcano-hydrothermal δ^7Li mineralization, or even salar-like δ^7Li, seems unlikely because it would suggest a large missing portion of previously formed Li-clay or a massive hidden deposit that would cause the δ^7Li enrichment here.

What could be more likely is that the measured δ^7Li, which averages 3.9‰, is close to the paleofluid because there was a quantitative uptake of Li during mineralization. In this case, there is minimal net fractionation at the bulk sample scale because there is no residual Li for Rayleigh fractionation to occur (i.e. f = 0, and ln(0) is undefined). Also, the measured δ^7Li is more likely to be reflective of the paleofluid composition than the calculated δ^7Li because it covers the lower δ^7Li range measured in the Li systems of the Andes. It is in the lower range because there likely was less reactive transport before Li mineralization compared to the Salar de Atacama, where Li migrates through basin-ward transition zones from the volcano-hydrothermal system to the ore-bearing salar nucleus (Alvarez-Amado et al., 2022; Munk et al., 2018).

6.2 A New Ore Genesis Model: A Tale of Two Brines

This section formulates a new genesis model where quantitative uptake of Li during mineralization is possible and elucidates how the generation and evolution pathway of the McDermitt Caldera Li brine was similar, yet distinct from the Li brine of the Salar de Atacama. Li enrichment began by fractional crystallization in magmas during silicic volcanism generated by intrusion of basaltic magma (Steens Basalt) into the upper crust during the initial impingement of the Yellowstone plume (Benson, Coble, et al., 2017). The eruption of this Li-rich magma produced a closed hydrothermally active lacustrine basin of peralkaline rhyolitic composition known as the McDermitt Caldera (Benson, Mahood, et al., 2017; Castor & Henry, 2020; Glanzman et al., 1978; Glanzman & Rytuba, 1979; Rytuba & Glanzman, 1979). Paleolake chemical compositions were mainly controlled by the influx of solutes mobilized from the alteration of the hot volcanic rocks in the hydrothermal system and the degassing of volatiles (Ingraffia et al., 2020), like is commonly observed in modern volcanic lakes (Varekamp, 2015).

Alteration reactions were driven by acidic volcanic fluids generated by deep high-temperature magmatic gases rich in SO_2 and CO_2, comparable to the associated present-day active Yellowstone open-system degassing dynamics (Lowenstern et al., 2015). Early in the evolution of the McDermitt Caldera, when it was the most volcanically active, the hydrothermal system was characterized by sulfuric acid-rich fluids that generated the U-Zr and Hg ore deposits within faults, fissures and fractures focused along the caldera rim (Castor & Henry, 2000, 2020; Henry et al., 2017). Paleolake waters were likely saline and acidic because of pervasive degassing from the highly active deep-seated magmatic system. Decreasing magmatic activity led to the eventual transition to a more quiescent carbonate-rich lake, relegating the acidic hydrothermal system to a significant depth under the lake, where the now mostly CO_2-charged hydrothermal fluid acidity was effectively consumed through deep-seated weathering of the host rock before reaching the surficial lacustrine system through vents and fumaroles (Pecoraino et al., 2015; Varekamp, 2015). A carbonate-rich paleoenvironment is supported by the ubiquitous presence of carbonate phases associated with the Li-bearing claystones at Thacker Pass. Additionally, the morphologies of the calcite nodules, seen in the results section, closely resemble the spherulitic calcite identified in other ancient alkaline volcanic lake deposits like the Barra Velha Formation (e.g. Mercedes-Martín et al., 2017; Saller et al., 2016; Wright & Barnett, 2015) and the calcite nodules actively crystalizing

in areas of Yellowstone, where CO_2 degassing from cooling water leads to the high pH values required for carbonate precipitation (e.g. Chafetz et al., 2018; Fouke, 2011).

High concentrations of lithium and other alkaline cations, silica, and carbonate alkalinity were supplied to the paleolake of the McDermitt Caldera by the hydrothermal fluids, meteoric waters and hydrolysis of glassy tuffaceous sediments (e.g. Castor & Henry, 2020). Li sources to the paleolake likely had δ^7Li values ranging from -2.5 to 0‰, consistent with the δ^7Li of Li-rich thermal waters that supply the fault-bounded Salar de Atacama Li brine resources in the volcanically active Andean arc (Alvarez-Amado et al., 2022; Godfrey et al., 2019; Rivas et al., 2024). These δ^7Li depleted values could have been obtained when Li was released from the volcanic source through igneous diffusive processes where ^{6}Li diffuses more readily from the cooling intracaldera McDermitt Tuff (Ellis et al., 2018; Ingraffia et al., 2020), and during the exsolution of Li-rich magmatic volatile phases at the magmatic-hydrothermal transition in the underlying reservoir (Ellis et al., 2022). In addition to supplying CO_2-rich fluids, the deep basaltic recharge in this caldera setting may have exsolved deep δ^7Li depleted Li-rich fluids to the shallower hydrothermal system (Iddon & Edmonds, 2020). Furthermore, dissolution of the rhyolitic material throughout the caldera system by fluids generated volcanic-rock-like depleted δ^7Li values, salinity and alkalinity, like has been observed during dissolution experiments of rhyolite samples from Yellowstone (Cullen et al., 2019). Li sourced by surficial weathering of the Li-bearing volcanic catchment likely evolved to progressively more enriched δ^7Li values (~10‰) by Rayleigh fractionation along the flow path, like has been observed in the Andes (e.g. Garcia et al., 2020; Munk et al., 2018).

Li and the rest of the solutes were then further concentrated in the closed basin by evapoconcentration, like current Li brine evolution in the Salar de Atacama where an arid climate plays a key role (e.g. Munk et al., 2016). The alkalinity generated by the underlying hydrothermal system, surficial weathering, and evaporative processes can be defined by charge balance of the conservative dissolved species that are linked to pH (based on Stumm & Morgan (1996)):

$$\begin{aligned}[\text{Alkalinity}] &= \left[HCO_3^-\right] + 2\left[CO_3^{2-}\right] + [OH^-] - \left[H^+\right] \\ &= \left[Li^+\right] + \left[Na^+\right] + \left[K^+\right] + 2\left[Ca^{2+}\right] + 2[Mg^{2+}] \\ &\quad - [F^-] - [Cl^-] - 2\left[SO_4^{2-}\right] - 2\left[NO_3^{2-}\right]\end{aligned} \qquad \text{[Equation 5.]}$$

Following evolution to a Li-rich alkaline solution from the degassing of lacustrine CO_2, the paleolake waters of the McDermitt Caldera could then have reached the high pH (>9.5) conditions required for the rapid nucleation of reactive Mg-silicate crystallites to form a highly hydrated and reactive gel from high Si and Mg activities in lake water as they coalesced on the lake floor (e.g. Millot, 1970; Tosca & Masterson, 2014). High pH waters allowed that silicic acid ($H_4SiO_4^0$) dissociated to the more soluble anion species $H_3SiO_4^-$, with reactive silanol groups able to synthesize reactions with magnesium ions, leading to Mg-silicate formation directly from water (Siffert, 1962). The gel substrate provided the ideal conditions for spherulitic calcite nucleation and growth (Tutolo & Tosca, 2018), and more importantly the reactive surface area for Li to get trapped in the octahedral sites of the crystalizing Mg-silicates, leading to isotope fractionation because ^{6}Li is preferably incorporated within the crystallizing Mg-silicates to form the Mg-smectite Li-clay mineral known as hectorite (Vigier et al., 2008) upon gel dehydration at the beginning of diagenesis (Tosca & Masterson, 2014), following the reaction:

$$xM^+ + xLi^+ + (3-x)Mg^{2+} + 4SiO_2(aq) + 2F^-(aq) + 5H_2O(l) = M_x(Mg_{(3-x)}Li_x)Si_4O_{10}(OH,F)_2 \bullet H_2O + 6H^+ \quad \text{[Equation 6.]}$$

The highly reactive nature of the Mg-silicate gel ensures that all the Li introduced to the structurally-closed paleolake is quantitively trapped in the multitude of crystallizing Mg-silicate structures, thus there is little to no measurable Li isotope fractionation at the bulk sample scale (δ^7Li average of 3.9‰). This rapid alkalinity-consuming authigenic clay neoformation process, known as "reverse weathering" (Von Damm & Edmond, 1984), often occurs in parallel to carbonate precipitation in the many alkaline lakes present in the volcanically active terrains of the East African Rift Valley, and is sustained by intermediate degrees of evaporative concentration that ensures the precipitation of more simple salts like halite do not dominate the system (Von Damm & Edmond, 1984). Because the catchment volcanic rocks of this rift environment have erupted from continental thinning (Owen et al., 2018), there is a lack of Li in the system (Benson, Coble, et al., 2017), hence the other more well-known Mg-clays (stevensite, sepiolite, talc and kerolite) tend to actively precipitate here (e.g. Darragi & Tardy, 1987; Eugster & Jones, 1979; Gac et al., 1977). Not every lacustrine sediment in the alkaline paleolake of the McDermitt Caldera was formed by reverse weathering, Al and Fe containing terrigenous silicate inputs of tuffaceous sediments, and detrital dioctahedral clays formed by weathering in the catchment were also

entrained into the lake by aeolian processes and lake margin alluvial fan systems (e.g. Cerling, 1979; Darragi & Tardy, 1987; Deocampo et al., 2009; Hay & Kyser, 2001; Hover & Ashley, 2003). Volcanic glass in contact with water in the alkaline lakes tends to alter to zeolite minerals and finally feldspars during diagenesis, often through an aluminosilicate gel precursor following dissolution of glass (e.g. Hay & Kyser, 2001; Langella et al., 2001; Renaut, 1993; Singer & Stoffers, 1980; Surdam & Eugster, 1976). Detrital Al-rich clays can be transformed to zeolites (e.g. Hay & Kyser, 2001; Renaut, 1993), or Mg-clays (e.g. Deocampo et al., 2009; Hay & Kyser, 2001; Hover & Ashley, 2003; Jones, 1986; Millot, 1970). As first described by Millot (1970), the terrigenous detrital inputs along the often migrating lake margins tend to create a zonation of more Al and Fe-rich and Mg-poor clays grading to more Mg-rich and Al and Fe-poor clays towards the basin center. Jones (1986) suggests that although neoformation of Mg-clays from alkaline water occurs, colloidal Al and Fe-rich particles, or incipient dioctahedral clays derived from the hydrolysis of glass could be critical in overcoming kinetic barriers to their nucleation. This clay formation by transformation of Al and Fe-rich particles appears to have been more relevant in the later stages of paleolake evolution, where the < 2 µm fraction is more Al and Fe-rich and holds less Mg and Li (Table 3 and Figure 24), like is more common of saponite (e.g. Tardy et al., 1972).

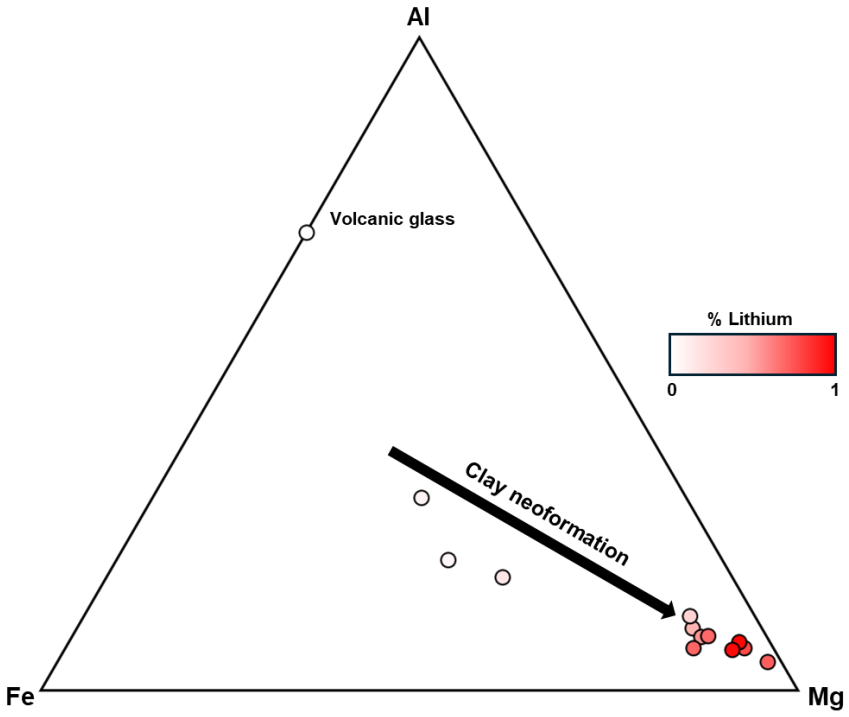

Figure 24. Ternary Al-Fe-Mg diagram showing LNC-001 clay separates and volcanic glass sample, with corresponding Li concentrations.

Despite being primitive Li-poor volcanic environments, massive-scale crustal thinning and rifting associated with the breaking apart of ancient supercontinents have generated economically important and enigmatic Mg-clays linked to giant offshore hydrocarbon reservoirs like the Barra Velha Formation (e.g. Wright, 2012). To refine facies models for exploration of Mg-clay associated hydrocarbon reservoirs, Mg-silicate synthesis experiments have provided valuable information on the precise chemical controls required for Mg-silicate precipitation and their possible diagenetic behavior in natural environments (e.g. Tosca, 2015; Tosca & Masterson, 2014; Tosca & Wright, 2018; Tutolo & Tosca, 2018). The geochemical controls required for direct neoformation of Mg-silicates (termed "homogeneous nucleation") lie in the kinetics and thermodynamics of the MgO-SiO_2-H_2O system, which can be demonstrated in a solubility diagram (Figure 25) (Tosca, 2015). The experimentally determined critical supersaturation line has been validated by applying it to various alkaline lakes of the East African Rift Valley, where Mg-silicate neoformation occurs, and alternatively in alkaline lakes where Mg-silicates are absent despite their supersaturation (Tosca, 2015).

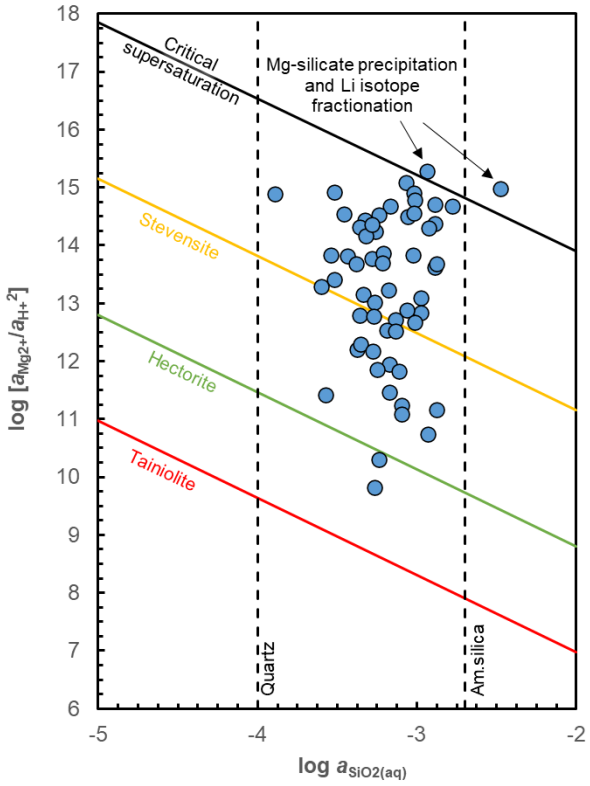

Figure 25. Applying the solubility diagram of the MgO-SiO_2-H_2O system at 25 °C and Mg-silicate critical supersaturation line for homogeneous nucleation from Tosca (2015) to Salar de Atacama water compositions compiled by Boschetti et al. (2007). Hectorite and tainiolite solubility lines are plotted from the thermodynamic data of Boschetti (2022). Stevensite solubility line is from Tosca (2015) and reference therein.

The significant supersaturation gap between the critical supersaturation line and the solubility line of Mg-silicates lies in kinetics, meaning the conditions with the required level of supersaturation for interactions between ions or molecules to yield large enough nuclei that are stable in solution, which is referred to as the critical radius (Lasaga, 1998; Stumm, 1992; Tosca, 2015). Boschetti et al. (2007) noted that unfavorable precipitation kinetics may be the likely culprit for absence of Mg-silicates in the inflowing brines to the Salar de Atacama despite their supersaturation, and this can be verified by plotting their data with the critical supersaturation boundary line determined by Tosca (2015). The solubility diagram demonstrates that the water inflows to the nucleus of the Salar de Atacama seldom reach the critical supersaturation to become supersaturated relative to Mg-silicates along their evaporation paths, although they come close.

The critical supersaturation boundary can be lowered with the presence of foreign surfaces, like silica, volcanic glass, biological surfaces, and detrital clays, which decrease the interfacial energy required for nucleation, and often provide the required chemical components, leading to "heterogeneous nucleation" of Mg-silicates (Tosca, 2015). From these findings, Mg-silicates formation by heterogeneous nucleation in the inflow areas of the Salar de Atacama could be occurring, and cause some of the Li isotope fractionation measured there (e.g. Munk et al., 2018).

This clay formation mechanism in the Salar de Atacama is likely not widespread and consistent, and does not yield clay volumes comparable to the claystones of the McDermitt Caldera. It is possible to conclude that the brine of the paleolake of the McDermitt Caldera acquired high Li concentrations through evapoconcentration like the brine of the Salar de Atacama, but importantly was alkaline at the end the evaporative flow path in the basin, and more specifically had the right hydrogeochemical conditions (a_{Mg2+}, $a_{SiO2(aq)}$, and pH) that promoted a thermodynamic and kinetic drive towards widespread homogeneous nucleation of reactive Li-trapping Mg-silicates in the lake water. As a mechanism, homogeneous nucleation is the only mechanism that can occur in laterally extensive areas because it is primarily controlled by the omnipresent climate (Tosca & Wright, 2018), and could explain the stark contrast between the distribution of the more localized caldera rim hydrothermal ore deposits and the Li-clays that are found throughout the 20 x 30 km caldera.

The Salar de Atacama brine did not evolve to be an alkaline brine at the end of its evaporative flow path, and the reason for this can be elaborated and illustrated using the concept of chemical divides during the evolution of closed basin brines introduced by Hardie & Eugster (1970). As described

earlier, the chemical composition of the volcanic catchment plays a primary role in generating Li deposits (Benson, Coble, et al., 2017), but it may also even dictate if the runoff is only saline or both saline and alkaline (Tutolo & Tosca, 2023). For an alkaline lake with high pH values to form, it is essential that the catchment generates runoff where the alkalinity (ALK) > 2[Ca + Mg], because from mass-balance requirements, Mg-silicates and Mg-carbonates mostly consume alkalinity and Mg in 2:1 molar ratios (Tosca & Tutolo, 2023). From this concept, it is possible to demonstrate how the McDermitt Caldera paleolake brine diverged from the evolutionary pathway of the Li-rich salt-crusted Salar de Atacama to precipitate the massive Li-rich claystone deposit by reverse weathering (Figure 26):

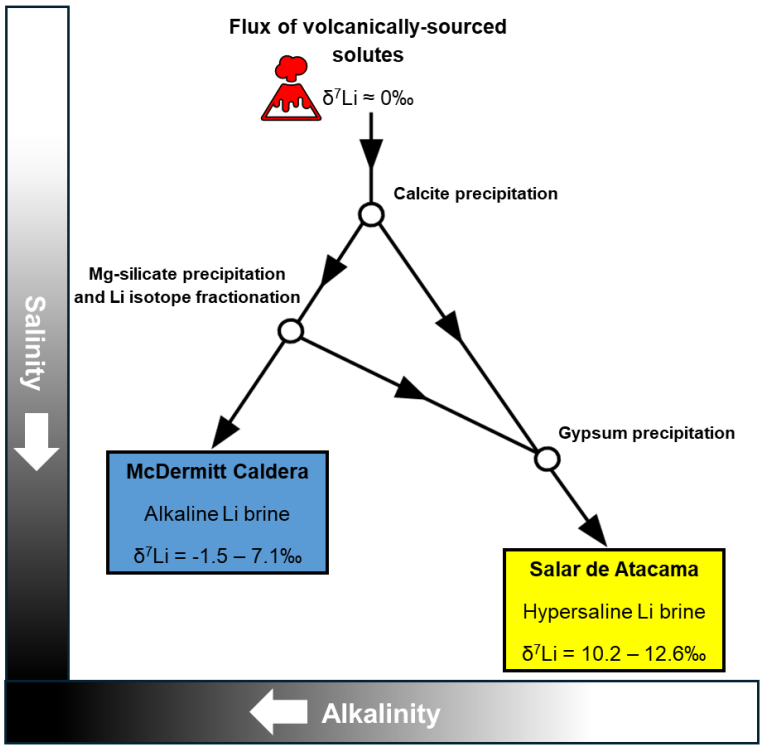

Figure 26. Chemical divides of brine evolution (Hardie & Eugster, 1970) presented here for the McDermitt Caldera and present-day Salar de Atacama settings. The first mineral to precipitate out of evaporating brine is calcite. From there, the brine can become more alkaline if $ALK_0 >> 2[Ca + Mg]_0$, or less alkaline if $ALK_0 << 2[Ca + Mg]_0$. The increasingly alkaline path reaches Mg-silicate precipitation, preferentially incorporating ^6Li and consuming ALK. If resulting ALK > 2[Ca + Mg], then brine remains on increasing ALK path. If resulting ALK < 2[Ca + Mg], then ALK is consumed, and brine evolution path converges with alkalinity depleted path as gypsum precipitates. The resultant brine evolves to be either sulfate or calcium-rich like what is found within the halite (NaCl) nucleus of the Salar de Atacama, as further described by the divides of Risacher et al. (2003). Salar de Atacama nucleus brine δ^7Li is from Munk et al. (2018).

The flowchart above helps illustrate the massive effect of carbonate and silicate mineral precipitation on evolving the chemical composition of a brine undergoing evapoconcentration, and

the major role the original composition of the dilute water has in determining the evaporative pathway taken (Hardie & Eugster, 1970). Alkalinity is limited in the Atacama because the catchment lithology features native sulfur, which oxidizes during weathering and acidifies the inflow water (Risacher et al., 2003). Gypsum-rich desert dust also enriches the water in Ca, which lowers the carbonate content, further driving the brine to compositions where ALK < 2[Ca + Mg] (Risacher et al., 2003). Furthermore, higher degrees of evapoconcentration likely occur in the Salar de Atacama compared to what transpired in the McDermitt Caldera, as evidenced by the absence of evaporite minerals like gypsum or halite (Von Damm & Edmond, 1984). Their absence is not evidence that the Thacker Pass system was not a brine as previously stated (Ingraffia, 2020), the brine simply never reached halite supersaturation. These two minor lithological differences in catchment composition and the degrees of evapoconcentration are the primary controls in determining the type of ore that will form in a volcanically influenced Li-enriched closed basin. If the McDermitt Caldera only generated hypersaline Li brines like the Salar de Atacama, drainage of the lake in the Miocene would have also drained the massive Li resource. This has major implications when exploring for Li-clay deposits in extinct silicic volcanic systems.

There is an 8.6‰ range in the δ^7Li of claystones of Thacker Pass (Figure 26), and this fluctuation could reflect influence of end-member Li sources. δ^7Li depletions in the claystones likely reflect periods of increasing thermal water inflow from the underlying hydrothermal system (e.g. Lowenstein et al., 2016; Renaut et al., 2021). It is noteworthy that the Li-illite bearing claystone with the most Li enrichment (highest Li/Mg of 0.12) that is associated with the most depleted paleobrine δ^7Li, has visible signs of volcanism, by presence of pyrite-coated angular volcanic glass shards seen in thin section. δ^7Li may not be an indicator of alkalinity, rather it may signal alkalinity from fresh volcanic inputs, or lack thereof if δ^7Li is enriched from catchment weathering or the paleolake reverse weathering trend. The most δ^7Li enriched claystones show signs of sluggish Mg-silicate precipitation, by evidence of their dissolution and replacement by microcrystalline dolomite. In Lake Turkana, the largest alkaline lake in the East African Rift Valley, pore waters of previously precipitated Mg-silicates show that CO_2 production during methanogenesis, following sulfate depletion in the lake, is enough to trigger their congruent dissolution during burial diagenesis (Cerling, 1996). Because Mg-silicates are thermodynamically and kinetically sensitive to pH, a slight decrease in pH from the high P_{CO_2} generated by methanogenesis is enough to shift the pore water from supersaturated to undersaturated with respect to Mg-silicates (Tosca & Wright,

2018). This shift in pore water composition combined with the extremely high surface area of Mg-silicates, especially when freshly precipitated, is enough for their weekly-bonded structures to rapidly dissolve, while also increasing carbonate alkalinity and favoring the formation of replacement dolomite, silicification, and secondary porosity, like is the case in the Barra Velha Formation (Tosca & Wright, 2018). Any diagenetic or hydrothermal processes that changes the composition of pore waters of Mg-silicates can modify the mineralogical assemblages (Pozo & Calvo, 2018), and this is observable in the replacement features (porosity, silicification, and dolomitization) found in the thin sections of Thacker Pass. Therefore, if fresh volcanic alkalinity inputs are lacking, reverse weathering slows, and already precipitated Li-trapping Mg-silicates may not persist during diagenesis. It is therefore important that alkaline conditions persist for preservation of the Mg-silicates (Tosca & Tutolo, 2023).

6.3 Diagenesis

Pore water compositions of freshly precipitated Mg-silicates at Thacker Pass are directly related to the mineralizing lake water composition and have a key role in determining the identity of the crystallizing Li-clay phase or authigenic accessory phase during diagenesis (e.g. Deocampo, 2015). As demonstrated, the paleolake of the McDermitt Caldera reached Mg-silicate precipitation during evapoconcentration, but beyond this, increasing salinity and alkalinity levels also increases the concentrations of the solutes (e.g. Li, Mg, K, F) relevant for forming each authigenic mineral observed here (Cerling, 1979; Hay & Kyser, 2001). Higher salinity and alkalinity levels were likely more common in the early stages of alkaline lake evolution of the McDermitt Caldera, from high inputs of a more active underlying hydrothermal system (Renaut et al., 2021). This is reflected in the depth profiles of the clay separates, where the combination of high Li and F concentrations (Decarreau, 1980; Vigier et al., 2008) led to Li concentrations reaching ~1% in the clay structure.

A combination of enhanced K-fixation from increasing layer charge by extreme Li incorporation in the Mg-silicate structure and the high K pore water concentrations led to illitization of the freshly precipitated smectite during early diagenesis, like is observed in other alkaline lakes (Deocampo, 2015). This Li-rich illite remarkably has the chemical formula of the mica known as tainiolite; $KLiMg_2Si_4O_{10}F_2$ (Castor & Henry, 2020; Morissette, 2012). Additionally, at the highest salinity and alkalinity levels, the calcite spherulites that initially precipitated within the Mg-silicate gels were replaced by fluorite from high F pore water concentrations. On the other hand, fine glassy

aluminous tuffaceous sediment inputs to the caldera lake were altered to Al-smectite, zeolite minerals and feldspars during diagenesis in alkaline conditions (e.g. Hay & Kyser, 2001; Langella et al., 2001; Renaut, 1993; Singer & Stoffers, 1980; Surdam & Eugster, 1976).

From XRD data, the most saline and alkaline conditions responsible for the formation of the most Li-enriched illitic clay is associated with albite, intermediate Li concentrations are associated with K-feldspar, and the lowest concentrations are associated with analcime, consistent with the zonation proposed by Castor & Henry (2020). The authigenic alteration zones of tuffaceous sediments form concentric patterns in closed alkaline lakes, because of basin-wide hydrogeochemical gradients (Langella et al., 2001), and in the paleolake of the McDermitt Caldera these gradients were likely present, resulting in the most saline and alkaline conditions in the deepest parts of the shallow paleolake.

Within the pore waters of precipitated Mg-silicate gels, dissolved sulfate was reduced by microbial sulfate reduction and reacted with also microbially reduced iron to form abundant pyrite framboids (Claes et al., 2021; Hay & Kyser, 2001). Iron is relatively immobile in aqueous environments (Clark, 2015), and here it is likely sourced from hydrothermal emanations to the lake or glassy tuffaceous sediment inputs (Hay & Kyser, 2001; Tosca et al., 2011). Thin sections analyzed here certainly support this, and the pyrite framboid distribution within the matrix and within the calcite spherulites also support a microbial origin (Claes et al., 2021). The important relationships with Li mineralization in the McDermitt Caldera can be compiled and summarized in a diagram (Figure 27) based on the diagrammatic representations of increasing alkalinity and salinity of Singer & Stoffers (1980) and Langella et al. (2001):

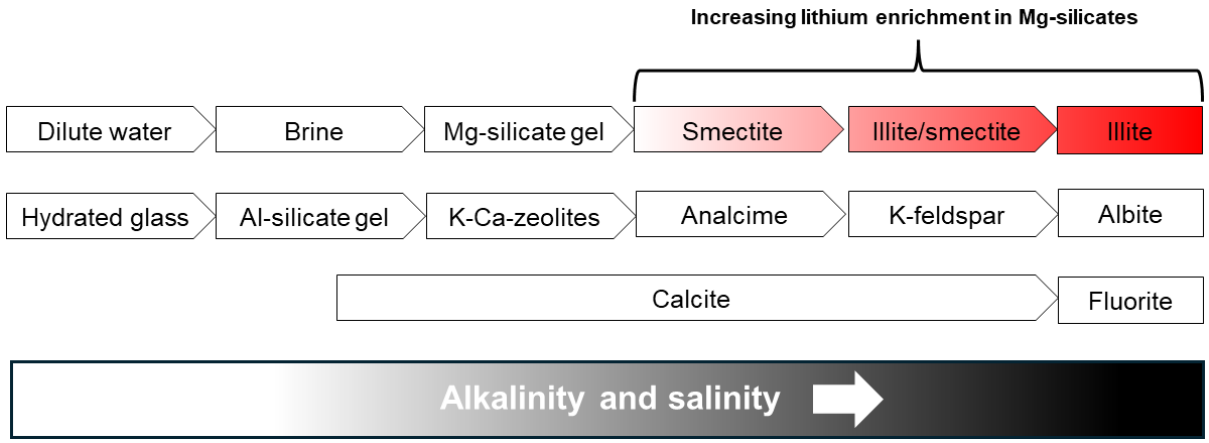

Figure 27. Authigenic mineral zones from increasing alkalinity and salinity in the paleolake of the McDermitt Caldera.

7. Conclusion

By examining mineralogical relationships and incorporating Li isotope measurements, this thesis introduces a new reverse weathering model of ore-genesis for the largest known lithium resource in the world. For Li-rich claystones to form in the structurally-closed paleolake of the McDermitt Caldera, it required the establishment of hydrogeochemical conditions that promoted a thermodynamic and kinetic drive towards widespread homogeneous nucleation of reactive Li-trapping Mg-silicates during evapoconcentration.

Earlier time periods during genesis of the deposit generally had the most saline and alkaline brines that typically have the highest Li, F and K concentrations (e.g. Cerling, 1979), leading to the extremely Li-rich ~1% Li illite phase during early diagenesis. The transitions to mixed-layer illite-smectite phases and to the hectorite phase indicate freshening periods that became more common as solute fluxes waned over time (Lowenstein et al., 2016; Renaut et al., 2021).

This mineralization model merges Li brine ore-genesis models with the substantial body of work aimed at understanding the alkaline lakes found in the East African Rift Valley and the more recent efforts applied to ancient alkaline lakes associated with massive offshore carbonate hydrocarbon reservoirs in the South Atlantic (e.g. Mercedes-Martín et al., 2017; Tosca & Wright, 2018; Tutolo & Tosca, 2018; Wright, 2020). Quantitative uptake of Li during mineralization, evidenced by measured volcanic-like δ^7Li ranging from -1.5 to 7.1‰ and the overall lack of isotopic trends with depth and Li enrichment suggests that most enrichment occurred during evapoconcentration of brine in the lacustrine basin. Episodic enhanced hydrothermal inputs to the caldera lake likely led to more depleted δ^7Li and periods with a quiescent hydrothermal system led to the more enriched δ^7Li. Li enrichment in the claystones was controlled by lacustrine salinity and alkalinity levels, consistent with the vertical tuffaceous sediment mineral alteration zones that follow the “closed hydrologic system diagenesis” model of Castor & Henry (2020). The maintenance of alkalinity has also been found to be essential in limiting replacement of the resource during diagenesis.

More work is needed to investigate Li isotope fractionation at the microscale within the claystones, and this could be achieved by careful analysis of nanometrically sized claystone separates (e.g. Clauer et al., 2014). Perhaps a wider range of δ^7Li can be measured here compared to the bulk scale, where quantitative uptake of Li largely obscures the high levels of fractionation expected to occur by reverse weathering during ore formation.

References

Alvarez-Amado, F., Tardani, D., Poblete-Gonzalez, C., Godfrey, L. V, & Matte-Estrada, D. (2022). Hydrogeochemical processes controlling the water composition in a hyperarid environment: New insights from Li, B, and Sr isotopes in the Salar de Atacama. *Science of The Total Environment*, *835*(April), 155470. https://doi.org/10.1016/j.scitotenv.2022.155470

Ames, L. L., Sand, L. B., & Goldich, S. S. (1958). A contribution on the hector, california bentonite deposit. *Economic Geology*, *53*(1), 22–37. https://doi.org/10.2113/gsecongeo.53.1.22

Bartels, A., Behrens, H., Holtz, F., & Schmidt, B. C. (2015). The effect of lithium on the viscosity of pegmatite forming liquids. *Chemical Geology*, *410*, 1–11. https://doi.org/10.1016/j.chemgeo.2015.05.011

Benson, T. R., Coble, M. A., Rytuba, J. J., & Mahood, G. A. (2017). Lithium enrichment in intracontinental rhyolite magmas leads to Li deposits in caldera basins. *Nature Communications*, *8*(1), 270. https://doi.org/10.1038/s41467-017-00234-y

Benson, T. R., Mahood, G. A., & Grove, M. (2017). Geology and 40 Ar/ 39 Ar geochronology of the middle Miocene McDermitt volcanic field, Oregon and Nevada: Silicic volcanism associated with propagating flood basalt dikes at initiation of the Yellowstone hotspot. In *Bulletin of the Geological Society of America* (Vol. 129, Issues 9–10). https://doi.org/10.1130/B31642.1

Berry, C. (2020). *Taming the Hydra: Funding the Lithium Ion Supply Chain in an Era of Unprecedented Volatility [Online First]*. IntechOpen. https://doi.org/10.5772/intechopen.92891

Boschetti, T. (2022). A revision of lithium minerals thermodynamics: Possible implications for fluids geochemistry and geothermometry. *Geothermics*, *98*(September 2021), 102286. https://doi.org/10.1016/j.geothermics.2021.102286

Boschetti, T., Cortecci, G., Barbieri, M., & Mussi, M. (2007). New and past geochemical data on fresh to brine waters of the Salar de Atacama and Andean Altiplano, northern Chile. *Geofluids*, *7*(1), 33–50. https://doi.org/10.1111/j.1468-8123.2006.00159.x

Bouchez, J., Von Blanckenburg, F., & Schuessler, J. A. (2013). Modeling novel stable isotope ratios in the weathering zone. *American Journal of Science*, *313*(4), 267–308. https://doi.org/10.2475/04.2013.01

Cabello, J. (2021). Lithium brine production, reserves, resources and exploration in Chile: An updated review. *Ore Geology Reviews*, *128*(November 2020). https://doi.org/10.1016/j.oregeorev.2020.103883

Calvo, J. P., Rodríguez-Arandía, J. P., Blanc-Valleron, M. M., Rouchy, J. M., & Sanz, E. (1999). Authigenic clay minerals in continental evaporitic environments. In M. Thiry & R. Simon-Coinçon (Eds.), *Palaeoweathering, Palaeosurfaces and Related Continental Deposits* (pp. 129–151). Blackwell Publishing Ltd. https://doi.org/10.1002/9781444304190.ch

Carrado, K. A., Decarreau, A., Petit, S., Bergaya, F., & Lagaly, G. (2006). Chapter 4 Synthetic Clay Minerals and Purification of Natural Clays. *Developments in Clay Science*, *1*(C), 115–

139. https://doi.org/10.1016/S1572-4352(05)01004-4

Castor, S. B., & Henry, C. D. (2000). Geology, geochemistry, and origin of volcanic rock-hosted uranium deposits in northwestern Nevada and southeastern Oregon, USA. *Ore Geology Reviews*, *16*(1–2), 1–40. https://doi.org/10.1016/S0169-1368(99)00021-9

Castor, S. B., & Henry, C. D. (2020). Lithium-Rich Claystone in the McDermitt Caldera, Nevada, USA: Geologic, Mineralogical, and Geochemical Characteristics and Possible Origin. *Minerals*, *10*(68).

Cerling, T. E. (1979). Paleochemistry of plio-pleistocene lake Turkana, Kenya. *Palaeogeography, Palaeoclimatology, Palaeoecology*, *27*(C), 247–285. https://doi.org/10.1016/0031-0182(79)90105-6

Cerling, T. E. (1996). Pore Water Chemistry of an Alkaline Lake: Lake Turkana, Kenya. In T. C. Johnson, E. O. Odada, & K. T. Whittaker (Eds.), *The Limnology, Climatology and Paleoclimatology of the East African Lakes* (1st editio, pp. 225–240). Routledge. https://doi.org/10.1201/9780203748978-12

Chafetz, H., Barth, J., Cook, M., Guo, X., & Zhou, J. (2018). Origins of carbonate spherulites: Implications for Brazilian Aptian pre-salt reservoir. *Sedimentary Geology*, *365*(January 2018), 21–33. https://doi.org/10.1016/j.sedgeo.2017.12.024

Chen, C., Lee, C. T. A., Tang, M., Biddle, K., & Sun, W. (2020). Lithium systematics in global arc magmas and the importance of crustal thickening for lithium enrichment. *Nature Communications*, *11*(1), 1–8. https://doi.org/10.1038/s41467-020-19106-z

Claes, H., Miranda, T., Falcão, T. C., Soete, J., Mohammadi, Z., Zieger, L., Erthal, M. M., Aguillar, J., Schmatz, J., Busch, A., & Swennen, R. (2021). Model for calcite spherulite formation in organic, clay-rich, lacustrine carbonate shales (Barbalha Formation, Aptian, Araripe Basin, NE Brazil). *Marine and Petroleum Geology*, *128*(February). https://doi.org/10.1016/j.marpetgeo.2021.104988

Clark, I. D. (2015). Groundwater geochemistry and isotopes. In *Groundwater Geochemistry and Isotopes*. https://doi.org/10.1201/b18347

Clauer, N., Williams, L. B., & Fallick, A. E. (2014). Genesis of nanometric illite crystals elucidated by light-element (hydrogen, lithium, boron and oxygen) isotope tracing, and K–Ar and Rb–Sr dating. *Chemical Geology*, *383*, 26–50. https://doi.org/10.1016/J.CHEMGEO.2014.05.025

Coble, M. A., & Mahood, G. A. (2012). Initial impingement of the Yellowstone plume located by widespread silicic volcanism contemporaneous with Columbia River flood basalts. *Geology*, *40*(7), 655–658. https://doi.org/10.1130/G32692.1

Coplen, T. B., Böhlke, J. K., De Bièvre, P., Ding, T., Holden, N. E., Hopple, J. A., Krouse, H. R., Lamberty, A., Peiser, H. S., Révész, K., Rieder, S. E., Rosman, K. J. R., Roth, E., Taylor, P. D. P., Vocke, R. D., & Xiao, Y. K. (2002). Isotope-abundance variations of selected elements (IUPAC technical report). *Pure and Applied Chemistry*, *74*(10), 1987–2017. https://doi.org/10.1351/pac200274101987

Cullen, J. T., Hurwitz, S., Barnes, J. D., Lassiter, J. C., Penniston-Dorland, S., Kasemann, S. A.,

& Thordsen, J. J. (2019). Temperature-dependent variations in mineralogy, major element chemistry and the stable isotopes of boron, lithium and chlorine resulting from hydration of rhyolite: Constraints from hydrothermal experiments at 150 to 350 °C and 25 MPa. *Geochimica et Cosmochimica Acta*, *261*, 269–287. https://doi.org/10.1016/j.gca.2019.07.012

Darragi, F., & Tardy, Y. (1987). Authigenic trioctahedral smectites controlling pH, alkalinity, silica and magnesium concentrations in alkaline lakes. *Chemical Geology*, *63*(1–2), 59–72. https://doi.org/10.1016/0009-2541(87)90074-X

Decarreau, A. (1980). Cristallogenèse expérimentale des smectites magnésiennes : hectorite, stévensite. *Bulletin de Minéralogie*, *103*(6), 579–590. https://doi.org/10.3406/bulmi.1980.7423

Decarreau, A., Vigier, N., Pálková, H., Petit, S., Vieillard, P., & Fontaine, C. (2012). Partitioning of lithium between smectite and solution: An experimental approach. *Geochimica et Cosmochimica Acta*, *85*, 314–325. https://doi.org/10.1016/j.gca.2012.02.018

Deocampo, D. M. (2015). Authigenic clay minerals in lacustrine mudstones. *Special Paper of the Geological Society of America*, *515*(January 2015), 49–64. https://doi.org/10.1130/2015.2515(03)

Deocampo, D. M., Cuadros, J., Wing-Dudek, T., Olives, J., & Amouric, M. (2009). Saline lake diagenesis as revealed by coupled mineralogy and geochemistry of multiple ultrafine clay phases: Pliocene Olduvai Gorge, Tanzania. *American Journal of Science*, *309*(9), 834–868. https://doi.org/10.2475/09.2009.03

Ehsani, R., Fourie, L., Hutson, A., Peldiak, D., Spiering, R., Young, J., & Armstrong, K. (2018). Technical Report on the Pre- Feasibility Study for the Thacker Pass Project, Humboldt County, Nevada. *Lithium Americas*.

Ellis, B. S., Neukampf, J., Bachmann, O., Harris, C., Forni, F., Magna, T., Laurent, O., & Ulmer, P. (2022). Biotite as a recorder of an exsolved Li-rich volatile phase in upper-crustal silicic magma reservoirs. *Geology*, *50*(4), 481–485. https://doi.org/10.1130/g49484.1

Ellis, B. S., Szymanowski, D., Magna, T., Neukampf, J., Dohmen, R., Bachmann, O., Ulmer, P., & Guillong, M. (2018). Post-eruptive mobility of lithium in volcanic rocks. *Nature Communications*, *9*(1). https://doi.org/10.1038/s41467-018-05688-2

Eugster, H. P., & Jones, B. F. (1979). Behavior of major solutes during closed basin- lakes brine evolution. In *American Journal of Science* (Vol. 279, Issue 6, pp. 609–631). https://doi.org/10.2475/ajs.279.6.609

Fishman, N. S., Turner, C. E., & Brownfield, I. K. (1995). Authigenic albite in a Jurassic alkaline, saline lake deposit, Colorado Plateau - evidence for early diagenetic origin. *US Geological Survey Bulletin*, *1806 p*.

Flesch, G. D., Anderson, A. R., & Svec, H. J. (1973). A secondary isotopic standard for 6Li/7Li determinations. *International Journal of Mass Spectrometry and Ion Physics*, *12*(3), 265–272. https://doi.org/10.1016/0020-7381(73)80043-9

Foshag, W., & Woodford, A. (1936). Bentonitic Magnesian Clay-Mineral From California.

American Mineralogist, *21*, 238–244.

Fouke, B. W. (2011). Hot-spring Systems Geobiology: Abiotic and biotic influences on travertine formation at Mammoth Hot Springs, Yellowstone National Park, USA. *Sedimentology*, *58*(1), 170–219. https://doi.org/10.1111/j.1365-3091.2010.01209.x

Gac, J. Y., Droubi, A., Fritz, B., & Tardy, Y. (1977). Geochemical behaviour of silica and magnesium during the evaporation of waters in Chad. *Chemical Geology*, *19*(1–4), 215–228. https://doi.org/10.1016/0009-2541(77)90016-X

Garcia, M. G., Borda, L. G., Godfrey, L. V, López Steinmetz, R. L., & Losada-Calderon, A. (2020). Characterization of lithium cycling in the Salar De Olaroz, Central Andes, using a geochemical and isotopic approach. *Chemical Geology*, *531*(October 2019), 119340. https://doi.org/10.1016/j.chemgeo.2019.119340

Glanzman, R. K., McCarthy, J. H., & Rytuba, J. J. (1978). Lithium in the McDermitt caldera, Nevada and Oregon. In *Energy* (Vol. 3, Issue 3). https://doi.org/10.1016/0360-5442(78)90031-2

Glanzman, R. K., & Rytuba, J. J. (1979). Zeolite-Clay Mineral Zonation of Volcaniclastic Sediments Within the McDermitt Caldera Complex of Nevada and Oregon. *USGS Open-File Report*, 1–25. https://pubs.usgs.gov/of/1979/1668/report.pdf

Glanzman, R. K., & Winsor, T. R. (1982). *King's River Lithium Project Humboldt County, Nevada*.

Godfrey, L., & Álvarez-amado, F. (2020). Volcanic and saline lithium inputs to the salar de atacama. *Minerals*, *10*(2), 1–17. https://doi.org/10.3390/min10020201

Godfrey, L. V, Chan, L. H., Alonso, R. N., Lowenstein, T. K., McDonough, W. F., Houston, J., Li, J., Bobst, A., & Jordan, T. E. (2013). The role of climate in the accumulation of lithium-rich brine in the central andes. *Applied Geochemistry*, *38*, 92–102. https://doi.org/10.1016/j.apgeochem.2013.09.002

Godfrey, L. V, Herrera, C., Gamboa, C., & Mathur, R. (2019). Chemical and isotopic evolution of groundwater through the active Andean arc of Northern Chile. *Chemical Geology*, *518*, 32–44. https://doi.org/10.1016/j.chemgeo.2019.04.011

Goldschmidt, V. M. (1937). The principles of distribution of chemical elements in minerals and rocks. The seventh Hugo Müller Lecture, delivered before the Chemical Society on March 17th, 1937. *J. Chem. Soc.*, *0*, 655–673. https://doi.org/10.1039/JR9370000655

Granquist, W. T., & Pollack, S. S. (1959). A Study of the Synthesis of Hectorite. *Clays and Clay Minerals*, *8*(1), 150–169. https://doi.org/10.1346/ccmn.1959.0080115

Hardie, L. A., & Eugster, H. P. (1970). Evolution of Closed-Basin Brines. *Mineral. Soc. Amer. Spec. Paper.*, *3*, 273–290.

Hay, R. L., & Kyser, T. K. (2001). Chemical sedimentology and paleoenvironmental history of Lake Olduvai, a Pliocene lake in northern Tanzania. *Bulletin of the Geological Society of America*, *113*(12), 1505–1521. https://doi.org/10.1130/0016-7606(2001)113<1505:CSAPHO>2.0.CO;2

Henry, C. D., Castor, S. B., Starkel, W. A., Ellis, B. S., Wolff, J. A., Laravie, J. A., McIntos, W. C., & Heizler, M. T. (2017). Geology and evolution of the McDermitt caldera, northern Nevada and southeastern Oregon, western USA. *Geosphere*, *13*(4), 1067–1112. https://doi.org/10.1130/GES01454.1

Hindshaw, R. S., Tosca, R., Goût, T. L., Farnan, I., Tosca, N. J., & Tipper, E. T. (2019). Experimental constraints on Li isotope fractionation during clay formation. *Geochimica et Cosmochimica Acta*, *250*, 219–237. https://doi.org/10.1016/j.gca.2019.02.015

Hoefs, J., & Sywall, M. (1997). Lithium isotope composition of Quaternary and Tertiary biogene carbonates and a global lithium isotope balance. *Geochimica et Cosmochimica Acta*, *61*(13), 2679–2690. https://doi.org/10.1016/S0016-7037(97)00101-4

Hofstra, A. H., Todorov, T. I., Mercer, C. N., Adams, D. T., & Marsh, E. E. (2013). Silicate melt inclusion evidence for extreme pre-eruptive enrichment and post-eruptive depletion of lithium in silicic volcanic rocks of the Western United States: Implications for the origin of Lithium-Rich Brines. *Economic Geology*, *108*(7), 1691–1701. https://doi.org/10.2113/econgeo.108.7.1691

Hover, V. C., & Ashley, G. M. (2003). Geochemical signatures of paleodepositional and diagenetic environments: A STEM/AEM study of authigenic clay minerals from an arid rift basin, Olduvai Gorge, Tanzania. *Clays and Clay Minerals*, *51*(3), 231–251. https://doi.org/10.1346/CCMN.2003.0510301

Huh, Y., Chan, L. H., Zhang, L., & Edmond, J. M. (1998). Lithium and its isotopes in major world rivers: implications for weathering and the oceanic budget. *Geochimica et Cosmochimica Acta*, *62*(12), 2039–2051. https://doi.org/10.1016/S0016-7037(98)00126-4

Iddon, F., & Edmonds, M. (2020). Volatile-Rich Magmas Distributed Through the Upper Crust in the Main Ethiopian Rift. *Geochemistry, Geophysics, Geosystems*, *21*(6). https://doi.org/10.1029/2019GC008904

Ingraffia, J. T. (2020). Lithium at the Thacker Pass deposit, Humboldt County, Nevada, U.S.A. *M.S. Thesis, University of Nevada Reno*, *February 2019*.

Ingraffia, J. T., Ressel, M. W., & Benson, T. R. (2020). Thacker Pass Lithium Clay Deposit , McDermitt Caldera , North-Central Nevada : Devitrification of McDermitt Tuff as the Main Lithium Source. *Geological Society of Nevada*.

Jones, B. F. (1986). Clay mineral diagenesis in lacustrine sediments. In F. A. Mumpton (Ed.), *Studies in Diagenesis* (Vol. 1578, pp. 291–300). U.S. Geological Survey Bulletin.

Julien, C., Mauger, A., Vijh, A., & Zaghib, K. (2016). *Lithium Batteries: Science and Technology*. Spring International Publishing. https://doi.org/10.1007/978-3-319-19108-9

Kalo, H., Milius, W., & Breu, J. (2012). Single crystal structure refinement of one-and two-layer hydrates of sodium fluorohectorite. *RSC Advances*, *2*, 8452–8459. https://doi.org/10.1039/c2ra20457f

Langella, A., Cappelletti, P., & De'Gennaro, M. (2001). Zeolites in closed hydrologic systems. *Reviews in Mineralogy and Geochemistry*, *45*(Surdam 1977), 235–260. https://doi.org/10.2138/rmg.2001.45.7

Lasaga, A. C. (1998). Kinetic theory in the earth sciences. In *Kinetic Theory in the Earth Sciences*. Princeton University Press. https://doi.org/10.5860/choice.36-4499

Li, W., Liu, X.-M., & Godfrey, L. V. (2018). Optimisation of Lithium Chromatography for Isotopic Analysis in Geological Reference Materials by MC-ICP-MS. *Geostandards and Geoanalytical Research*, *43*(2), 261–276. https://doi.org/10.1111/ggr.12254

Lithium Americas. (2025). *Lithium Americas Increases Mineral Resource and Reserve for Thacker Pass [News release]*. https://lithiumamericas.com/news/news-details/2025/Lithium-Americas-Increases-Mineral-Resource-and-Reserve-for-Thacker-Pass/default.aspx

Liu, Y. H., Huang, K. F., & Lee, D. C. (2018). Precise and accurate boron and lithium isotopic determinations for small sample-size geological materials by MC-ICP-MS. *Journal of Analytical Atomic Spectrometry*, *33*(5), 846–855. https://doi.org/10.1039/c7ja00400a

Lowenstein, T. K., Dolginko, L. A. C., & García-Veigas, J. (2016). Influence of magmatic-hydrothermal activity on brine evolution in closed basins: Searles Lake, California. *Bulletin of the Geological Society of America*, *128*(9–10), 1555–1568. https://doi.org/10.1130/B31398.1

Lowenstern, J. B., Bergfeld, D., Evans, W. C., & Hunt, A. G. (2015). Origins of geothermal gases at Yellowstone. *Journal of Volcanology and Geothermal Research*, *302*, 87–101. https://doi.org/10.1016/j.jvolgeores.2015.06.010

Magna, T., Janoušek, V., Kohút, M., Oberli, F., & Wiechert, U. (2010). Fingerprinting sources of orogenic plutonic rocks from Variscan belt with lithium isotopes and possible link to subduction-related origin of some A-type granites. *Chemical Geology*, *274*(1–2), 94–107. https://doi.org/10.1016/j.chemgeo.2010.03.020

Magna, T., Wiechert, U. H., & Halliday, A. N. (2004). Low-blank isotope ratio measurement of small samples of lithium using multiple-collector ICPMS. *International Journal of Mass Spectrometry*, *239*(1), 67–76. https://doi.org/10.1016/j.ijms.2004.09.008

Mercedes-Martín, R., Brasier, A. T., Rogerson, M., Reijmer, J. J. G., Vonhof, H., & Pedley, M. (2017). A depositional model for spherulitic carbonates associated with alkaline, volcanic lakes. *Marine and Petroleum Geology*, *86*, 168–191. https://doi.org/10.1016/j.marpetgeo.2017.05.032

Millot, G. (1970). *Geology of Clays*. Springer-Verlag.

Misra, S., & Froelich, P. N. (2009). Measurement of lithium isotope ratios by quadrupole-ICP-MS: Application to seawater and natural carbonates. *Journal of Analytical Atomic Spectrometry*, *24*(11), 1524–1533. https://doi.org/10.1039/b907122a

Möller, M. W., Hirsemann, D., Haarmann, F., Senker, J., & Breu, J. (2010). Facile scalable synthesis of rectorites. *Chemistry of Materials*, *22*(1), 186–196. https://doi.org/10.1021/cm902800y

Moore, D. M., & Reynolds, R. C. (1997). *X-ray Diffraction and the Identification and Analysis of Clay Minerals*. Oxford University Press.

Morissette, C. (2012). The Impact of Geological Environment on the Lithium Concentration and

Structural Composition of Hectorite Clays. *UNR Thesis*.

Munk, L. A., Boutt, D. F., Hynek, S. A., & Moran, B. J. (2018). Hydrogeochemical fluxes and processes contributing to the formation of lithium-enriched brines in a hyper-arid continental basin. *Chemical Geology*, *493*, 37–57. https://doi.org/10.1016/j.chemgeo.2018.05.013

Munk, L. A., Hynek, S. A., Bradley, D. C., Boutt, D., Labay, K., & Jochens, H. (2016). Lithium Brines: A Global Perspective. *Rare Earth and Critical Elements in Ore Deposits*, *18*, 339–365. https://pubs.geoscienceworld.org/books/book/1998/chapter/16276487

Natural Resources Canada. (2020). *Canada and U.S. Finalize Joint Action Plan on Critical Minerals Collaboration [Press release]*. https://www.canada.ca/en/natural-resources-canada/news/2020/01/canada-and-us-finalize-joint-action-plan-on-critical-minerals-collaboration.html

Neukampf, J., Ellis, B. S., Magna, T., Laurent, O., & Bachmann, O. (2019). Partitioning and isotopic fractionation of lithium in mineral phases of hot, dry rhyolites: The case of the Mesa Falls Tuff, Yellowstone. *Chemical Geology*, *506*, 175–186. https://doi.org/10.1016/j.chemgeo.2018.12.031

Owen, R. B., Renaut, R. W., & Lowenstein, T. K. (2018). Spatial and temporal geochemical variability in lacustrine sedimentation in the East African Rift System: Evidence from the Kenya Rift and regional analyses. *Sedimentology*, *65*(5), 1697–1730. https://doi.org/10.1111/sed.12443

Pecoraino, G., D'Alessandro, W., & Inguaggiatom, S. (2015). The other side of the coin: geochemistry of alkaline lakes in volcanic areas. In D. Rouwet, J. Vandemeulebrouck, B. Christenson, & F. Tassi (Eds.), *Volcanic Lakes* (pp. 219–237). Springer-Verlag. https://doi.org/10.1007/978-3-642-36833-2

Pogge von Strandmann, P. A. E., Kasemann, S. A., & Wimpenny, J. (2020). Lithium and Lithium Isotopes in Earth's Surface Cycles. *Elements*, *16*(4), 253–258. https://doi.org/10.2138/gselements.16.4.253

Pozo, M., & Calvo, J. P. (2018). An overview of authigenic magnesian clays. *Minerals*, *8*(11), 1–22. https://doi.org/10.3390/min8110520

Renaut, R. W. (1993). Zeolitic diagenesis of late Quaternary fluviolacustrine sediments and associated calcrete formation in the Lake Bogoria Basin, Kenya Rift Valley. *Sedimentology*, *40*(2), 271–301. https://doi.org/10.1111/j.1365-3091.1993.tb01764.x

Renaut, R. W., Owen, R. B., Lowenstein, T. K., De Cort, G., Mcnulty, E., Scott, J. J., & Mbuthia, A. (2021). The role of hydrothermal fluids in sedimentation in saline alkaline lakes: Evidence from Nasikie Engida, Kenya Rift Valley. *Sedimentology*, *68*(1), 108–134. https://doi.org/10.1111/sed.12778

Risacher, F., Alonso, H., & Salazar, C. (2003). The origin of brines and salts in Chilean salars: A hydrochemical review. *Earth-Science Reviews*, *63*(3–4), 249–293. https://doi.org/10.1016/S0012-8252(03)00037-0

Rivas, S., Sanchez, A. P., Alvarez Amado, F., Perez Fodich, A., Godfrey, L., Becerra, P.,

Tardani, D., Perez Flores, P., Aron, F., Fica, C., Munoz Saez, C., & Mathur, R. (2024). Water-rock interaction and magmatic contribution in thermal fluids of the Southern Volcanic Zone, Chile: Insights from Li, B and Sr isotopes. *Journal of Volcanology and Geothermal Research*, *453*(July), 108149. https://doi.org/10.1016/j.jvolgeores.2024.108149

Ross, C. S., & Hendricks, S. B. (1943). Minerals of the montmorillonite group: Their origin and relation to soils and clays. *Geological Survey Professional Paper 205-B*, *23–79*, 23–79.

Rudolph, W., Brooker, M. H., & Pye, C. C. (1995). Hydration of lithium ion in aqueous solution. *Journal of Physical Chemistry*, *99*(11), 3793–3797. https://doi.org/10.1021/j100011a055

Rytuba, J. J., & Glanzman, R. K. (1979). Relation of mercury, uranium, and lithium deposits to the McDermitt caldera complex, Nevada-Oregon. In *Papers on mineral deposits of western North America (Report 33)* (pp. 109–117). Nevada Bureau of Mines and Geology.

Saller, A., Rushton, S., Buambua, L., Inman, K., McNeil, R., & Dickson, J. A. D. T. (2016). Presalt stratigraphy and depositional systems in the Kwanza Basin, offshore Angola. *AAPG Bulletin*, *100*(7), 1135–1164. https://doi.org/10.1306/02111615216

Sanderson, H. (2020). *Tesla's move into mining aimed at energising battery supply chain*. Financial Times. https://www.ft.com/content/b13f316f-ed85-4c5f-b1cf-61b45814b4ee

Siffert, B. (1962). Quelques réactions de la silice en solution : la formation des argiles. *Mém. Serv. Carte Géol. Als-Lorr.*, *21*, 86.

Singer, A., & Stoffers, P. (1980). Clay mineral diagenesis in two East African lake sediments. *Clay Minerals*, *15*(3), 291–307. https://doi.org/10.1180/claymin.1980.015.3.09

Starkey, H. C. (1982). Role of Clays in Fixing Lithium. *US Geological Survey Bulletin*.

Strese, H., & Hofmann, U. (1941). Synthese von Magnesiumsilikat-Gelen mit zweidimensional regelmäßiger struktur. *Zeitschrift Für Anorganische Und Allgemeine Chemie*, *247*(1–2), 65–95. https://doi.org/10.1002/zaac.19412470107

Stumm, W. (1992). *Chemistry of the Solid-Water Interface: Processes at the Mineral-Water and Particle-Water Interface in Natural Systems*. John Wiley & Sons, Inc.

Stumm, W., & Morgan, J. J. (1996). *Aquatic Chemistry: Chemical Equilibria and Rates in Natural Waters* (Third). John Wiley & Sons, Ltd.

Surdam, R. C., & Eugster, H. P. (1976). Mineral reactions in the sedimentary deposits of the Lake Magadi region, Kenya. *Bulletin of the Geological Society of America*, *87*(12), 1739–1752. https://doi.org/10.1130/0016-7606(1976)87<1739:MRITSD>2.0.CO;2

Tardy, Y., Gérard, K., & Trauth, N. (1972). Le lithium dans les minéraux argileux des sédiments et des sols. *Geochimica et Cosmochimica Acta*, *86*, 387–412.

Tomascak, P. B., Magna, T., & Dohmen, R. (2016). Methodology of lithium analytical chemistry and isotopic measurements. In *Advances in Lithium Isotope Geochemistry* (p. 5). Springer. https://doi.org/10.1007/978-3-319-01430-2

Tosca, N. J. (2015). Geochemical Pathways to Mg-Silicate Formation. In M. Pozo & E. Galán (Eds.), *Magnesian Clays: Characterization, Origin and Applications* (pp. 283–329). AIPEA

(Association Internationale pour l'Etude des Argiles), Special Publications.

Tosca, N. J., Macdonald, F. A., Strauss, J. V., Johnston, D. T., & Knoll, A. H. (2011). Sedimentary talc in Neoproterozoic carbonate successions. *Earth and Planetary Science Letters*, *306*(1–2), 11–22. https://doi.org/10.1016/j.epsl.2011.03.041

Tosca, N. J., & Masterson, A. L. (2014). Chemical controls on incipient Mg-silicate crystallization at 25°C: Implications for early and late diagenesis. *Clay Minerals*, *49*(2), 165–194. https://doi.org/10.1180/claymin.2014.049.2.03

Tosca, N. J., & Tutolo, B. M. (2023). How to Make an Alkaline Lake: Fifty Years of Chemical Divides. *Elements*, *19*(1), 15–21. https://doi.org/10.2138/GSELEMENTS.19.1.15

Tosca, N. J., & Wright, V. P. (2014). The Formation and Diagenesis of Mg-Clay Minerals in Lacustrine Carbonate Reservoirs. *AAPG Annual Convention and Exhibition*, *51002*, 24.

Tosca, N. J., & Wright, V. P. (2018). Diagenetic pathways linked to labile Mg-clays in lacustrine carbonate reservoirs: A model for the origin of secondary porosity in the Cretaceous pre-salt Barra Velha Formation, offshore Brazil. *Geological Society Special Publication*, *435*(1), 33–46. https://doi.org/10.1144/SP435.1

Tutolo, B. M., & Tosca, N. J. (2018). Experimental examination of the Mg-silicate-carbonate system at ambient temperature: Implications for alkaline chemical sedimentation and lacustrine carbonate formation. *Geochimica et Cosmochimica Acta*, *225*, 80–101. https://doi.org/10.1016/j.gca.2018.01.019

Tutolo, B. M., & Tosca, N. J. (2023). Dry, Salty, and Habitable: The Science of Alkaline Lakes. *Elements*, *19*(1), 10–14. https://doi.org/10.2138/GSELEMENTS.19.1.10

USGS. (2021). Lithium. In *Mineral Commodity Summaries*.

Van Hoecke, K., Belza, J., Croymans, T., Misra, S., Claeys, P., & Vanhaecke, F. (2015). Single-step chromatographic isolation of lithium from whole-rock carbonate and clay for isotopic analysis with multi-collector ICP-mass spectrometry. *Journal of Analytical Atomic Spectrometry*, *30*(12), 2533–2540. https://doi.org/10.1039/c5ja00165j

Varekamp, J. C. (2015). The chemical composition and evolution of volcanic lakes. In D. Rouwet, B. Christenson, F. Tassi, & J. Vandemeulebrouck (Eds.), *Volcanic Lakes*. Springer-Verlag. https://doi.org/10.1007/978-3-642-36833-2

Velde, B. (1995). *Origin and mineralogy of clays*. Springer-Verlag.

Verdel, C., Niemi, N., & van der Pluijm, B. A. (2011). Variations in the illite to muscovite transition related to metamorphic conditions and detrital muscovite content: Insight from the Paleozoic passive margin of the southwestern United States. *Journal of Geology*, *119*(4), 419–437. https://doi.org/10.1086/660086

Vigier, N., Decarreau, A., Millot, R., Carignan, J., Petit, S., & France-Lanord, C. (2008). Quantifying Li isotope fractionation during smectite formation and implications for the Li cycle. *Geochimica et Cosmochimica Acta*, *72*, 780–792. https://doi.org/10.1016/j.gca.2007.11.011

Von Damm, K. L., & Edmond, J. M. (1984). Reverse weathering in the closed basin lakes of the

Ethiopian Rift. In *American Journal of Science* (Vol. 284, pp. 835–862).

Warr, L. N. (2019). A new collection of clay mineral 'Crystallinity' Index Standards and revised guidelines for the calibration of Kübler and Árkai indices – ERRATUM. *Clay Minerals*, *54*(1), 109–109. https://doi.org/10.1180/clm.2019.12

Wright, V. P. (2020). The mantle, CO2 and the giant Aptian chemogenic lacustrine carbonate factory of the South Atlantic: Some carbonates are made, not born. *Sedimentology*. https://doi.org/10.1111/sed.12835

Wright, V. P., & Barnett, A. J. (2015). An abiotic model for the development of textures in some South Atlantic early Cretaceous lacustrine carbonates. *Geological Society Special Publication*, *418*(1), 209–219. https://doi.org/10.1144/SP418.3

Zhu, G., Ma, J., Wei, G., & Zhang, L. (2020). A Rapid and Simple Method for Lithium Purification and Isotopic Analysis of Geological Reference Materials by MC-ICP-MS. *Frontiers in Chemistry*, *8*(November). https://doi.org/10.3389/fchem.2020.557489

Appendix A

The remainder of diffraction patterns used to generate Table 4:

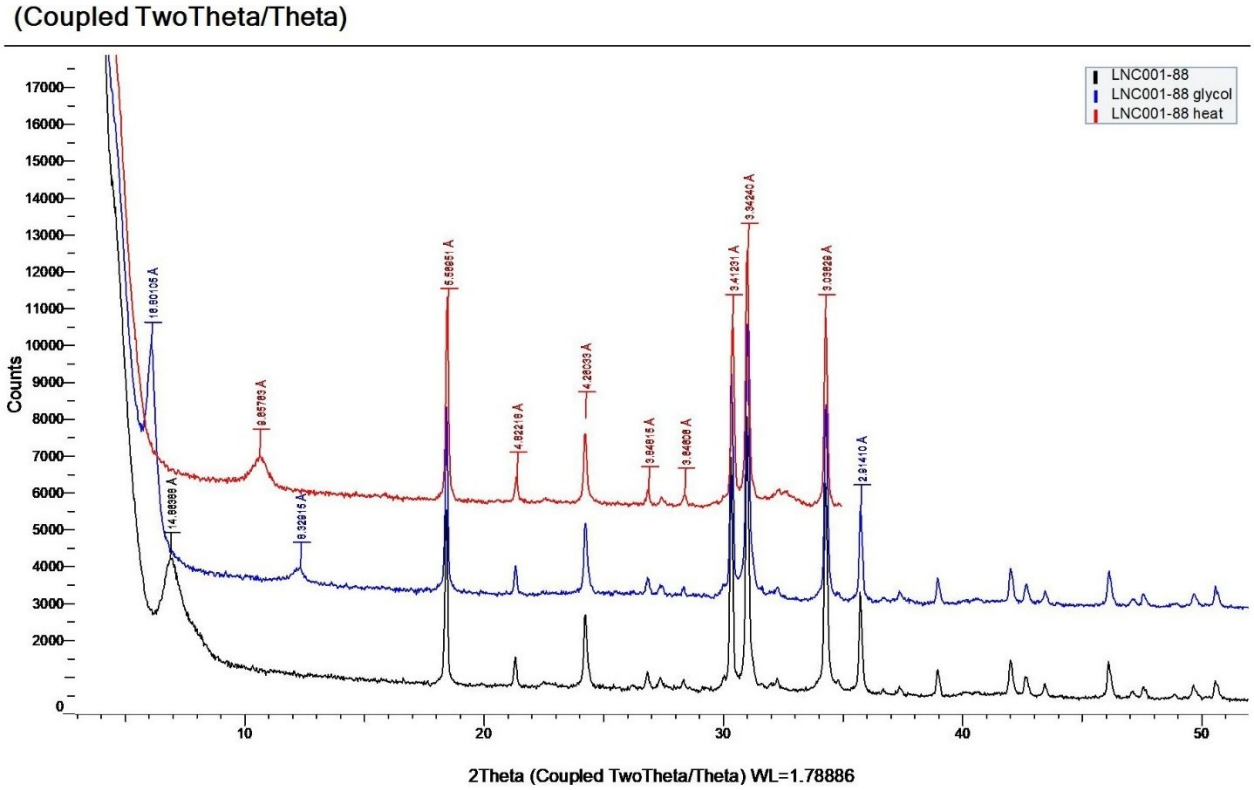

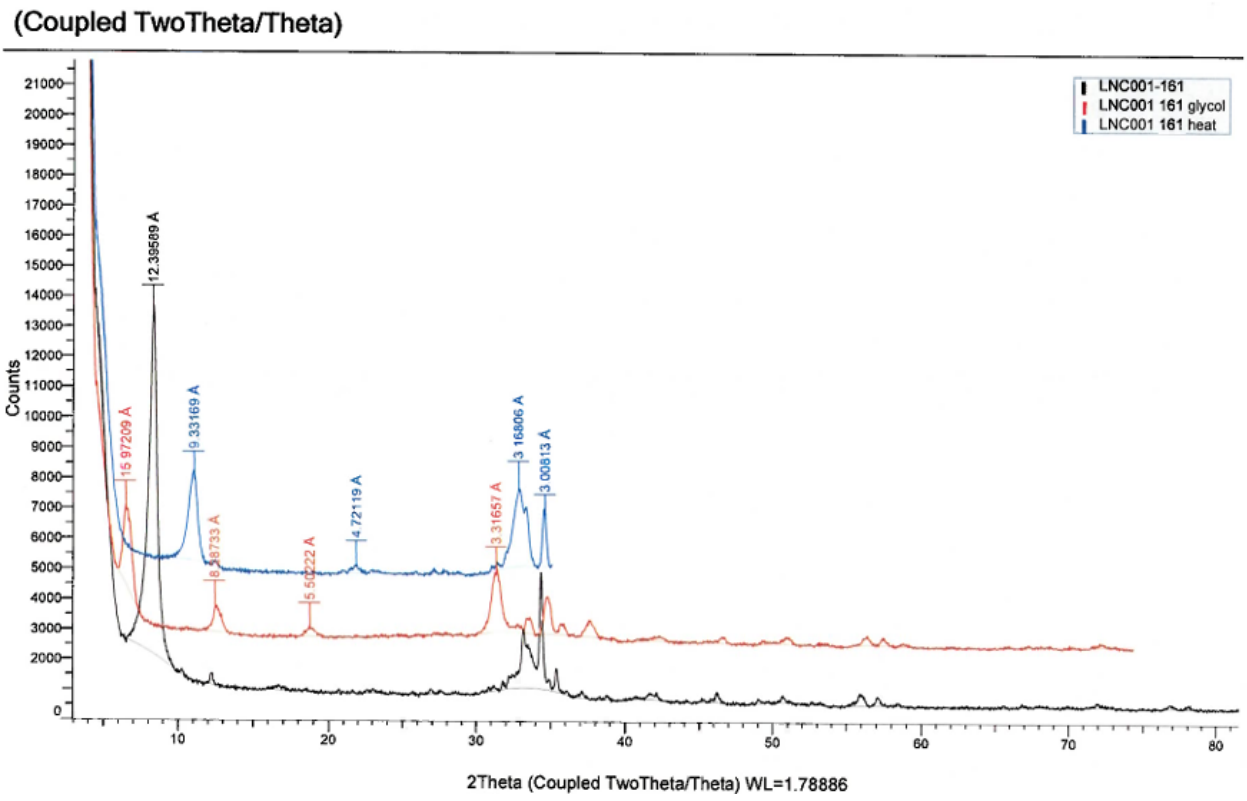

(Coupled TwoTheta/Theta)

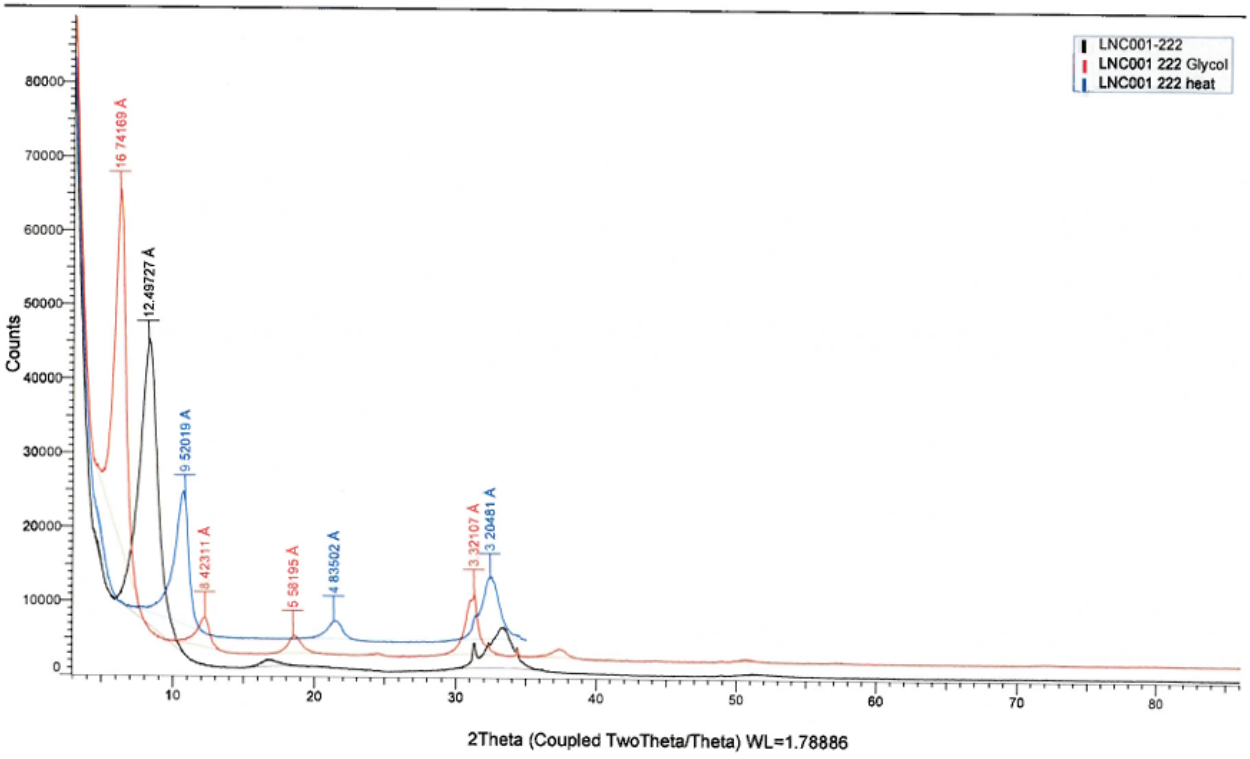

(Coupled TwoTheta/Theta)

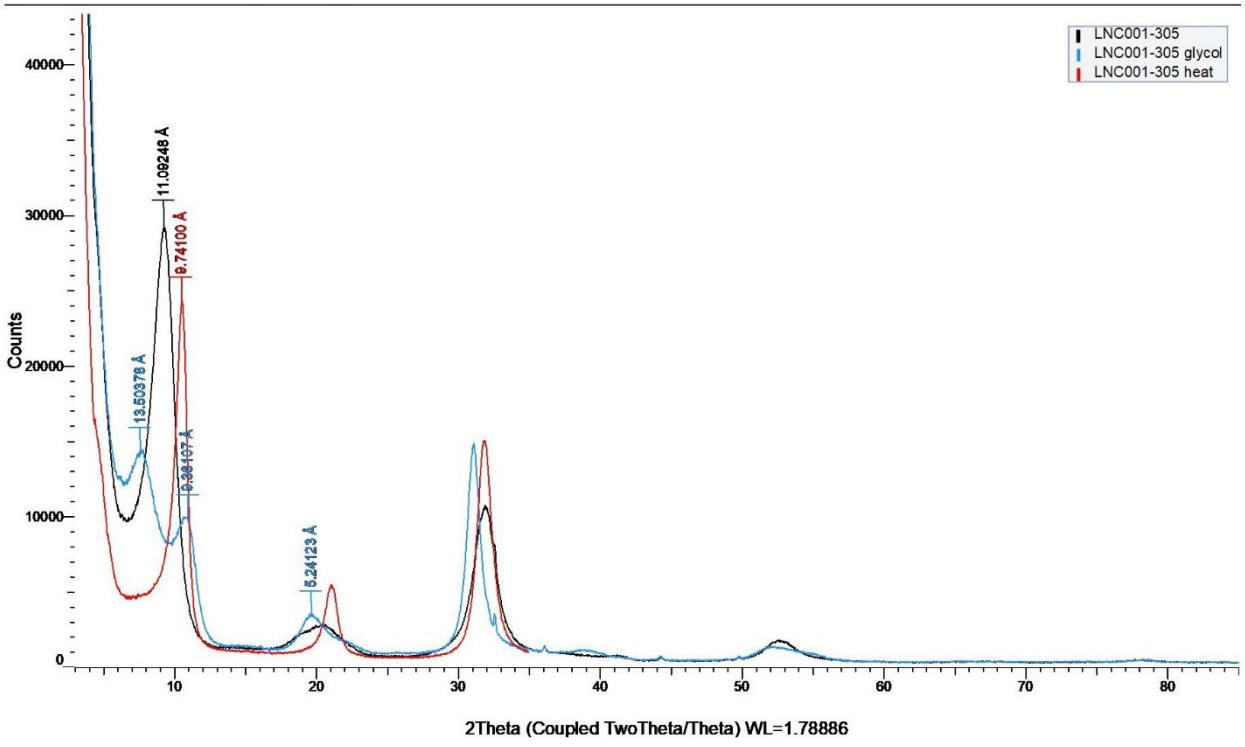

(Coupled TwoTheta/Theta)

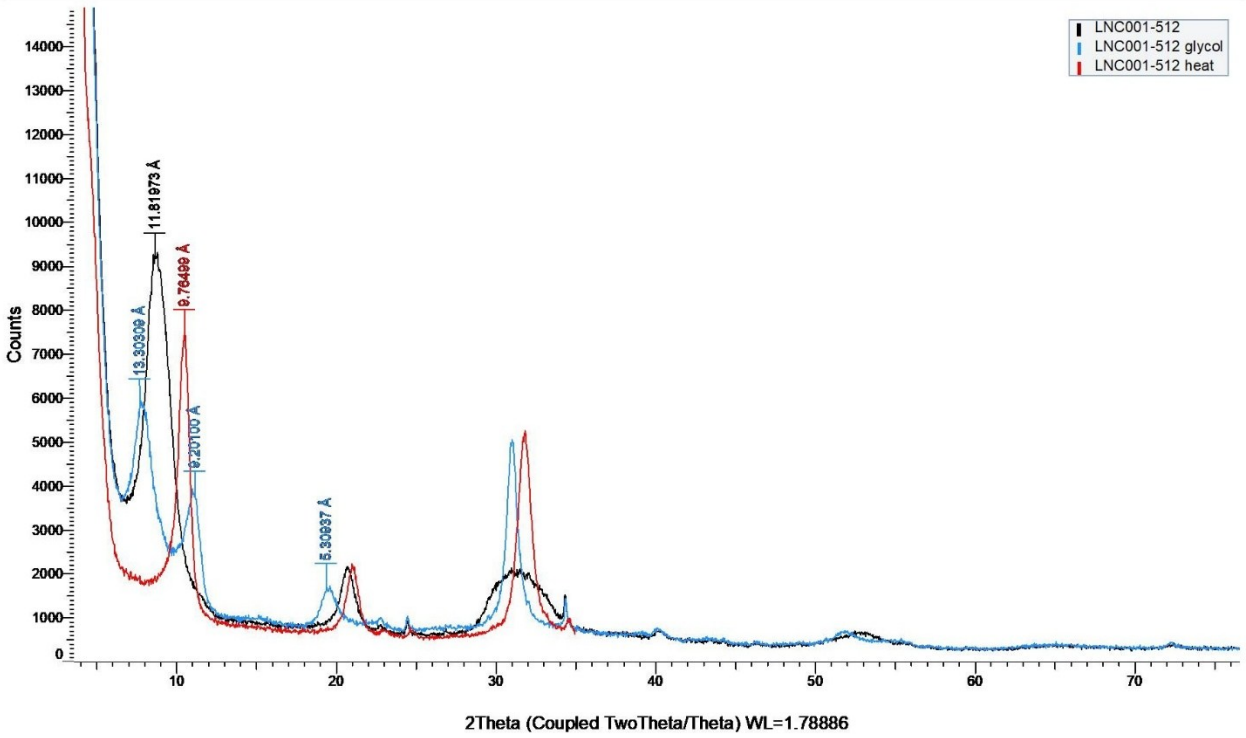

Appendix B

Alternate view of thin section scans presented in photomicrography section:

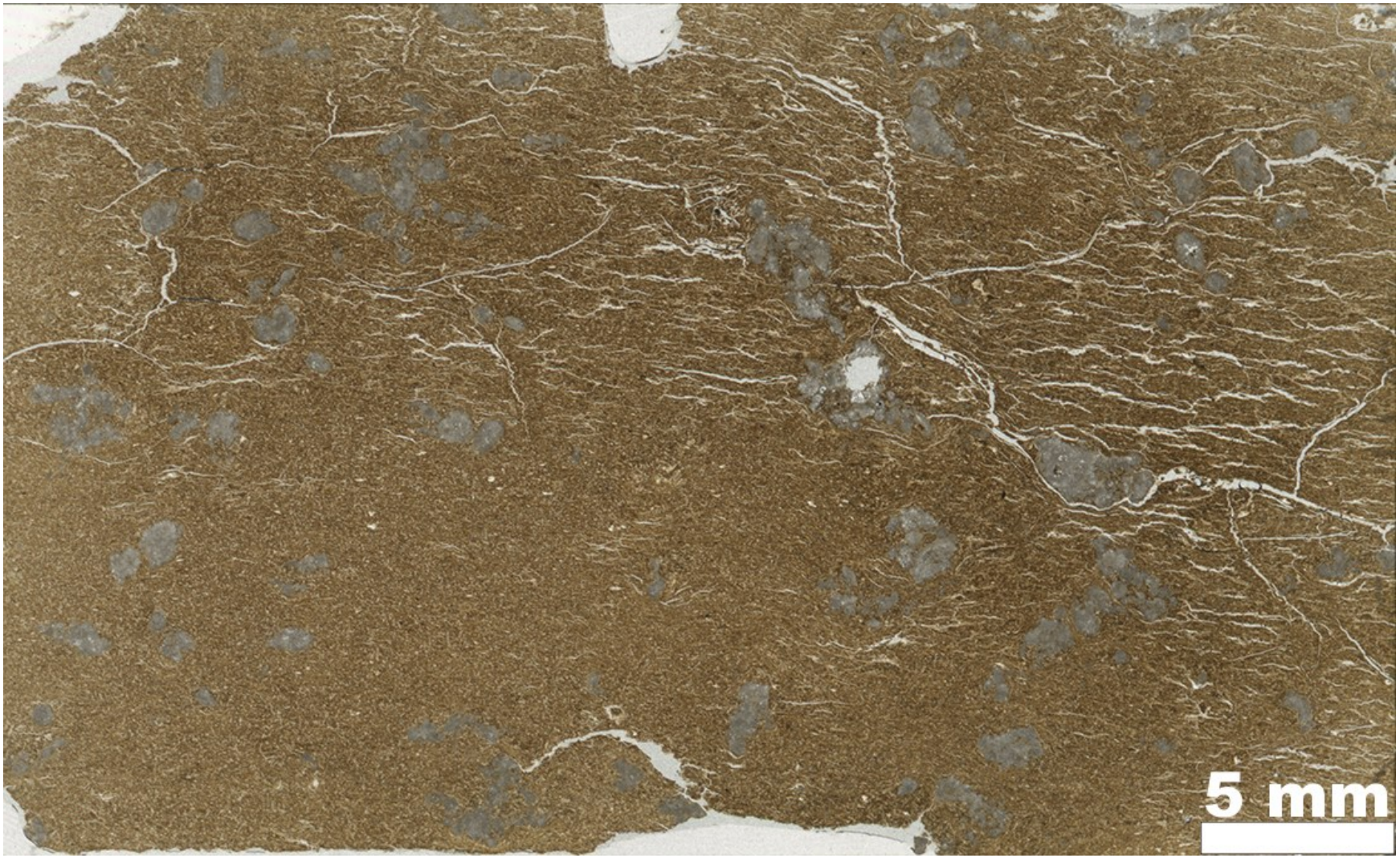

Plane-polars view of thin section scan from Figure 13.

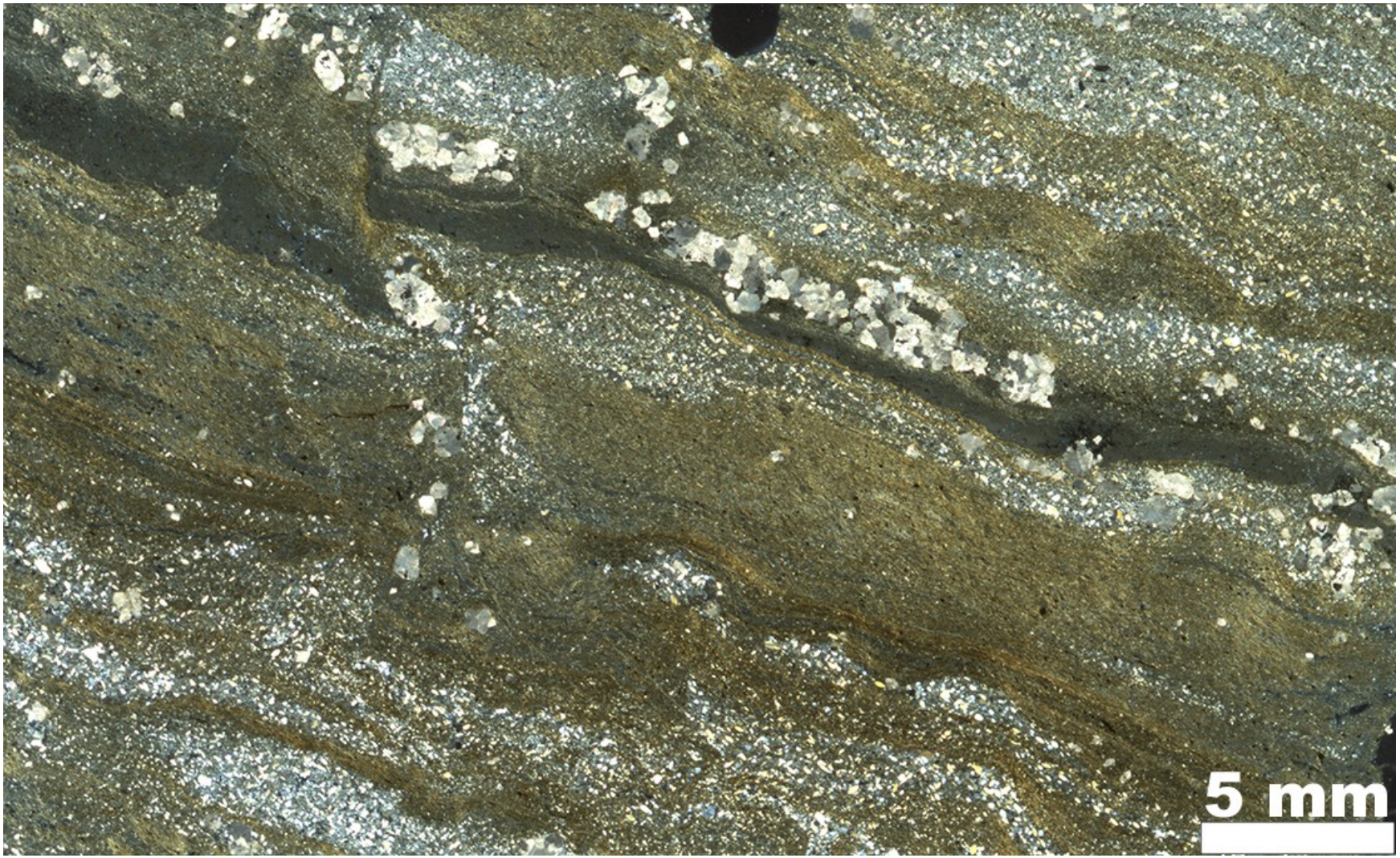

Cross-polars view of thin section scan from Figure 14.

Plane-polars view of thin section scan from Figure 16.

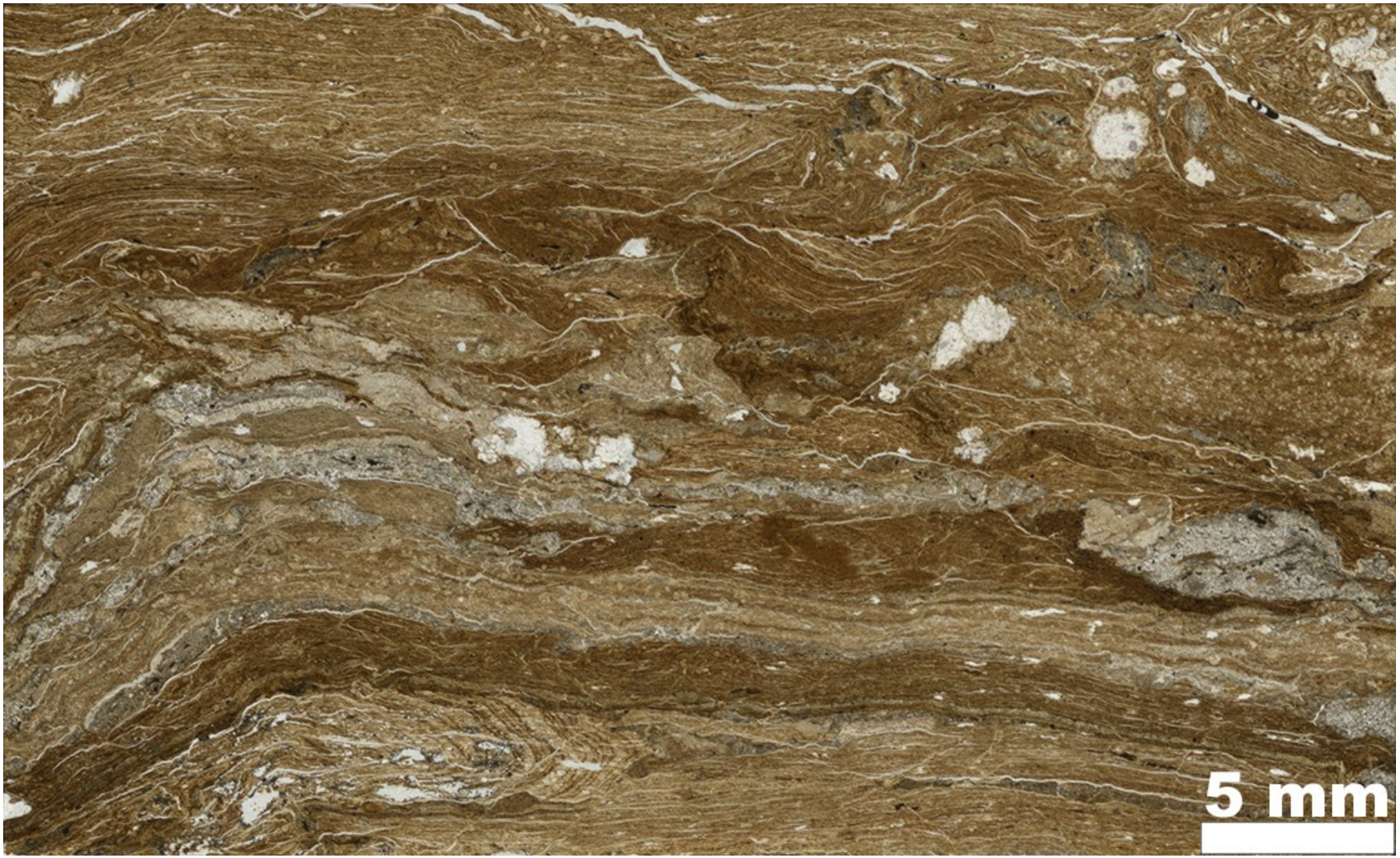

Plane-polars view of thin section scan from Figure 17.

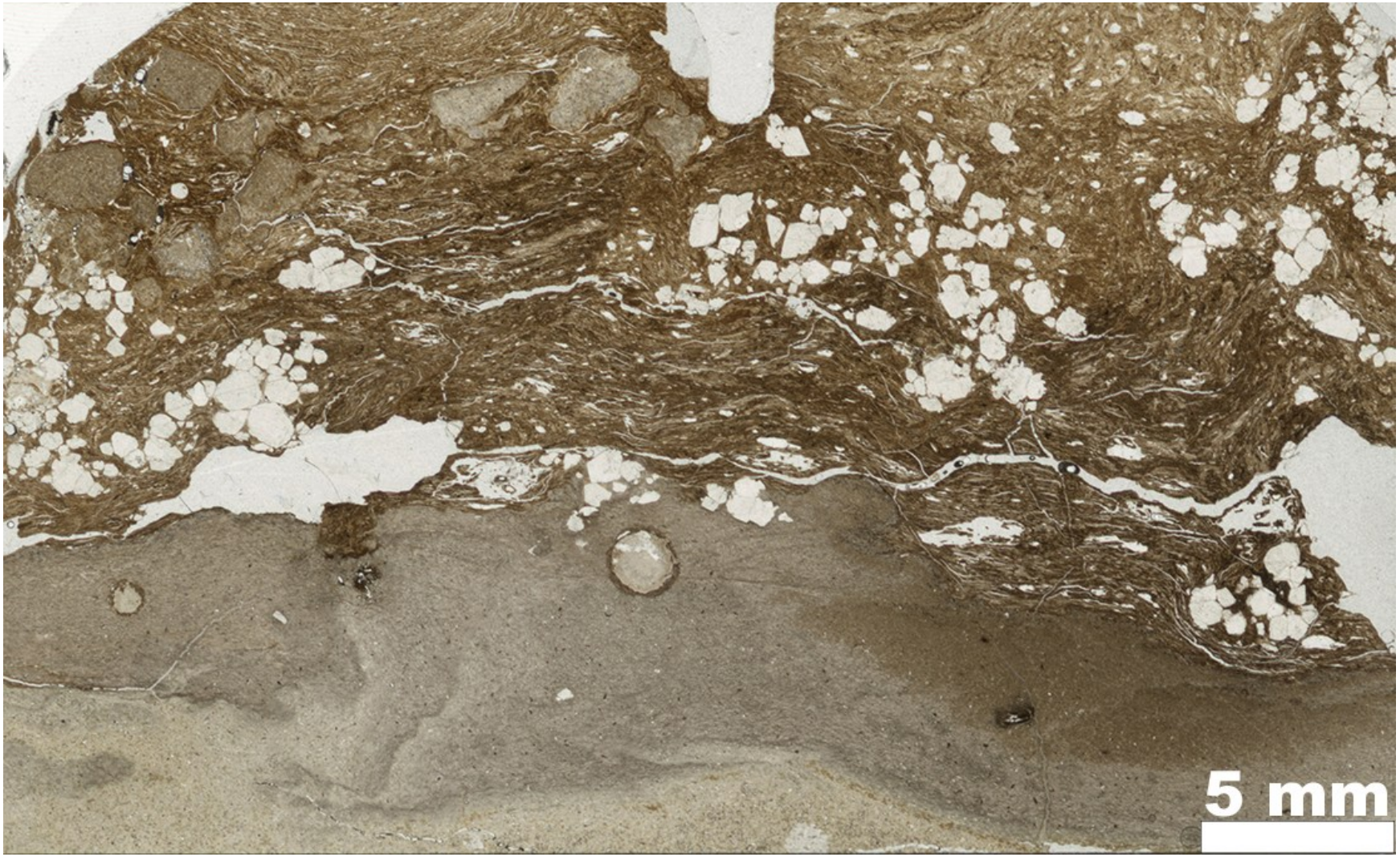

Plane-polars view of thin section scan from Figure 20.

Plane-polars view of thin section scan from Figure 21.